



**UNIVERSIDAD DE INVESTIGACIÓN DE  
TECNOLOGÍA EXPERIMENTAL  
YACHAY**

**Escuela de Ciencias Físicas y Nanotecnología**

**Using Theoretical Spectroscopy to  
Characterize Nanoporous Networks**

Trabajo de integración curricular presentado como  
requisito para la obtención del título de Físico

**Autor:**

Gustavo Ramon Campi Ortiz

**Tutor:**

PhD. Duncan John Mowbray

**Cotutor:**

PhD. Abner de Siervo

Urcuquí, octubre 2024

## **Autoría**

Yo, **Gustavo Ramon Campi Ortiz**, con cédula de identidad 0928346212, declaro que las ideas, juicios, valoraciones, interpretaciones, consultas bibliográficas, definiciones y conceptualizaciones expuestas en el presente trabajo; así como los procedimientos y herramientas utilizadas en la investigación, son de absoluta responsabilidad de el/la autor (a) del trabajo de integración curricular. Así mismo, me acojo a los reglamentos internos de la Universidad de Investigación de Tecnología Experimental Yachay.

Urququí, octubre 2024.

---

Gustavo Ramon Campi Ortiz  
CI. 0928346212

## **Autorización de publicación**

Yo, **Gustavo Ramon Campi Ortiz**, con cédula de identidad 0928346212, cedo a la Universidad de Investigación de Tecnología Experimental Yachay, los derechos de publicación de la presente obra, sin que deba haber reconocimiento económico por este concepto. Declaro además que el texto del presente trabajo de titulación no podrá ser cedido a ninguna empresa editorial para su publicación u otros fines, sin contar previamente con la autorización escrita en la Universidad.

Asimismo, autorizo a la Universidad que realice la digitalización y publicación de este trabajo de integración curricular en el repositorio virtual, de conformidad con lo dispuesto en el Art. 144 de la Ley Orgánica de Educación Superior.

Urququí, octubre 2024.

---

Gustavo Ramon Campi Ortiz  
CI. 0928346212

## **Dedication**

This work is dedicated to the most important person in my life, the only person who has deeply believed in me since childhood. To my dad, who always gave me his deepest support and inspired me to pursue my dreams even though they seemed impossible.

## Acknowledgements

I extend my heartfelt thanks to the higher power I call God for guiding me through this extraordinary journey in my major. For those who may not share this belief, I am grateful for the intricate interplay of chaos and causality that shaped this path.

I sincerely thank my advisor, Duncan J. Mowbray, for his invaluable support and exceptional assistance during this project. His wisdom and knowledge, which he shared generously as part of his research group, were fundamental to my work. This experience also presented an excellent opportunity to collaborate with many talented individuals. I am incredibly thankful for the flexibility he facilitated in working remotely, on campus, and at 'Arbol de la vida'.

I thank my co-advisors, Abner de Siervo and Alisson Ceccato, for generously sharing their expertise during every meeting and welcoming me into their research group & laboratory at UNICAMP.

De la misma manera, deseo expresar mi profunda gratitud a mi familia por el apoyo que cada uno de sus integrantes ha brindado en los momentos clave de mi formación como científico. Especialmente agradecido con mis padres, Gustavo y Mónica, por su incansable esfuerzo, la visión y misión que tuvieron para con su hijo, lo cual contribuyó enormemente a mi apoyo y éxito. Esta gratitud hacia ellos es algo que me llevaré a la tumba, un sentimiento eterno de agradecimiento que al igual que el amor que siento por ellos permanecerá conmigo siempre.

Thanks to everyone who has been on my path during my major, with a special mention to all those members of Yachay Tech who are a constant inspiration to my career path, regarding those I can call 'friends' who supported me on hard times such as O.S, M.G, E.Q, A.R, S.Q, J.S, D.G.

I am deeply grateful to all my professors, dean, and everyone who was and is still part of Yachay Tech University and the School of Physics and Nanotechnology who made me stay at this point with their assistance.

In addition,

- Thanks to the School of Physical Sciences and Nanotechnology from Yachay Tech University, which supported the computational cluster Imbabura.
- Thanks to the Institute of Physics Gleb Wataghin of the State University of Campinas (UNICAMP), which supported the experimental part of this work on the Laboratory of Surface Physics (GFS).
- Thanks to CEDIA, which supported the CEDIA computational cluster.

## Resumen

Las mediciones espectroscópicas y microscópicas han demostrado ser herramientas esenciales para la caracterización de estructuras a nanoescala. Sin embargo, estos métodos siguen siendo tanto costosos como consumidores de tiempo. Por estas razones, los métodos teóricos robustos de espectroscopía y microscopía se han convertido en una alternativa atractiva. En este trabajo, realizamos un análisis de espectroscopía teórica y una comparación con mediciones experimentales recientes de redes nanoporosas en superficies metálicas, específicamente, capas superpuestas de 1,3,4-tris[4-(piridin-4-il)-[1,1'-bifenil]]benceno (TPyPPB) en Ag(111). Utilizaremos métodos basados en la teoría del funcional de la densidad (DFT) para simular los espectros medidos por transformada de Fourier en infrarrojo (FTIR), modos Raman resonantes, espectros de absorción óptica (OA), espectros de fotoelectrón en ultravioleta (UPS), espectros de emisión de fotoelectrón inverso (IPES) y microscopía de efecto túnel (STM) de estos sistemas. Al hacerlo, proporcionaremos información sobre los mecanismos fisicoquímicos detrás de la formación de estas redes nanoporosas y la robustez de las técnicas espectroscópicas teóricas para su caracterización más eficiente.

**Palabras clave:** DFT, TPyPPB, FTIR, Raman, espectros, STM, UPS, IPES, OA

## Abstract

Spectroscopic and microscopic measurements have proven essential tools for characterizing structures at the nanoscale. However, these methods are still both cost-prohibitive and time-consuming. For these reasons, robust theoretical spectroscopy and microscopy methods have become an attractive alternative. In this work, we perform a theoretical spectroscopy analysis and comparison with recent experimental measurements of nanoporous networks on metallic surfaces, specifically, overlayers of 1,3,4-tris[4-(pyridine-4-yl)-[1,1'-biphenyl]]benzene (TPyPPB) on Ag(111). We will use density functional theory (DFT) based methods to simulate the measured Fourier transform infrared (FTIR) spectra, resonant Raman modes, optical absorption (OA) spectra, ultraviolet photoelectron spectra (UPS), inverse photoemission spectra (IPES), and scanning tunneling microscopy (STM) of these systems. In so doing, we will provide insight into the physio-chemical mechanisms behind the formation of these nanoporous networks and the robustness of theoretical spectroscopic techniques for their more efficient characterization.

**Keywords:** DFT, TPyPPB, FTIR, Raman, spectra, STM, UPS, IPES, OA

# Contents

<b>List of Figures</b>	<b>xiv</b>
<b>List of Tables</b>	<b>xvi</b>
<b>List of Papers</b>	<b>xvii</b>
<b>1 Introduction</b>	<b>1</b>
1.1 Problem Statement . . . . .	4
1.2 General and Specific Objectives . . . . .	5
1.2.1 General Objective . . . . .	5
1.2.2 Specific Objectives . . . . .	5
1.3 Overview . . . . .	5
<b>2 Theoretical Background</b>	<b>7</b>
2.1 Density Functional Theory . . . . .	7
2.1.1 The Schrödinger Equation . . . . .	7
2.1.2 The Many-Body Problem . . . . .	8
2.1.3 Born-Oppenheimer approximation . . . . .	9
2.1.4 Periodic systems . . . . .	10
2.1.5 Reciprocal space . . . . .	11
2.1.6 The Hohenberg-Kohn Theorems and implications . . . . .	13
2.1.7 Self-consistent Kohn-Sham approach . . . . .	15
2.1.8 Exchange-Correlation (XC) Functionals . . . . .	20
2.1.9 Derivative Discontinuity . . . . .	23
2.1.10 Band Gap . . . . .	25
2.1.11 GLLB-SC to Describe Band Gaps . . . . .	26
2.2 Representations of the KS wavefunctions . . . . .	26
2.2.1 Real-Space (RS) . . . . .	27
2.2.2 Plane Waves (PW) . . . . .	27



2.2.3	Atomic Orbitals . . . . .	28
2.3	Projector Augmented Wave (PAW) Method . . . . .	29
2.4	Time-Dependent Density Functional Theory (TDDFT) . . . . .	30
2.4.1	Runge-Gross . . . . .	30
2.4.2	Time-Dependent KS equations . . . . .	31
2.4.3	LCAO Time-propagation TDDFT . . . . .	32
2.4.4	Linear density response of the KS system . . . . .	32
2.5	Vibrational Spectroscopy . . . . .	35
2.5.1	Infrared . . . . .	36
2.5.2	Resonant Raman (RR) . . . . .	36
2.6	Bader Charge Analysis . . . . .	37
2.6.1	Grid Method . . . . .	37
2.7	Density of States (DOS) . . . . .	37
2.7.1	Molecular Orbital PDOS . . . . .	38
2.8	UPS . . . . .	38
2.9	Scanning Tunneling Microscopy . . . . .	39
2.10	1,3,4-tris[4-(pyridine-4-yl)- [1,1'-biphenyl]]benzene (TPyPPB) . . . . .	40
2.10.1	TPyPPB on Ag(111) . . . . .	43
<b>3</b>	<b>Methodology</b>	<b>47</b>
3.1	Experimental Details . . . . .	47
3.2	Computational details . . . . .	49
<b>4</b>	<b>Results &amp; Discussion</b>	<b>53</b>
4.1	Formation Energies . . . . .	53
4.2	Vibrational Spectroscopy . . . . .	55
4.2.1	Isolated TPyPPB on gas phase . . . . .	55
4.2.2	Highly ordered self-assembled monolayers on Ag(111) . . . . .	57
4.3	UPS . . . . .	59
4.4	IPES . . . . .	61
4.5	Projected density of states . . . . .	63
4.6	Charge Transfer . . . . .	67
4.7	LCAO-TDDFT- $k$ - $\omega$ . . . . .	67
4.8	STM . . . . .	71
<b>5</b>	<b>Conclusions &amp; Outlook</b>	<b>73</b>
<b>A</b>	<b>Short Appendix 1 Heading for the Table of Contents</b>	<b>77</b>
	<b>Bibliography</b>	<b>81</b>

# List of Figures

2.1	Kohn-Sham ansatz	16
2.2	Kohn-Sham self-consistent scheme	18
2.3	E(Q) vs Q	24
2.4	UPS Schematic	39
2.5	Experimental STM schematic	40
2.6	TPyPPB	41
2.7	STM image of TPyPPB on Cu(111)	42
2.8	STM image of honeycomb high ordered structure	43
2.9	STM image of TPyPPB on Ag(111)	44
2.10	STM image of TPyPPB on Ag(111) with Cl adatoms	45
3.1	Dichloro(1,10-phenanthroline)Platinum(II)	48
3.2	TPyPPB on Ag(111) Packing structures without and with Cl adatoms	50
4.1	Triangular and Inverted Packing lattices	54
4.2	FTIR	56
4.3	Resonant-Raman	57
4.4	FTIR both packings	58
4.5	UPS	60
4.6	IPES Schematic	61
4.7	IPES	62
4.8	DOS isolated TPyPPB in gas phase	64
4.9	PDOS Triangular Packing	65
4.10	PDOS Inverted Packing	66
4.11	HOMO & LUMO TPyPPB	68
4.12	OAS TPyPPB	69
4.13	Exciton density TPyPPB	70
4.14	STM Triangular Packing	71
4.15	STM Inverted Packing	72

A.1	Triangular packing structures . . . . .	78
A.2	Inverted packing structures . . . . .	79

# List of Tables

4.1	Difference in formation energies . . . . .	55
4.2	FTIR active vibrational modes of TPyPPB . . . . .	55
4.3	Raman active vibrational modes of TPyPPB . . . . .	57
4.4	FTIR active vibrational modes of TPyPPB on Ag(111) packings . . . . .	59
4.5	Ratios between intensities . . . . .	59
4.6	Charge transfer of both packings with no adatoms . . . . .	67
4.7	Charge transfer of both packings with 1/2 Cl atoms per TPyPPB molecule . . . . .	67



# List of Papers

- [1] Ceccatto, A.; Campi, G. C.; Carreño-Díaz, V.; da Costa-Ferreira, E. B.; Waleska-Wellenhofer, N. J.; Freiburger, E. M.; Jaekel, S.; Papp, C.; Hans-Peter, S.; Duncan, J. M.; de Siervo, A. "Engineering: Two-Dimensional Supramolecular Self-Assembly: The Role of Cl Atoms", *Submitted 2024*
  
- [2] Campi, G. C.; Ceccatto, A.; de Siervo, A.; Duncan, J. M. "Using FTIR Simulation to Characterize Metal–Organic Frameworks: TPyPB on Cu(111)", *Submitted 2024*



# Chapter 1

## Introduction

Since the dawn of civilization, and likely even before, humankind has sought to invent tools to simplify their daily tasks. This intrinsic drive to innovate has been a constant throughout history, shaping societies' development and technology's evolution. However, as humanity has progressed, the nature of our needs and challenges has undergone a profound transformation. Developing new paradigms, such as quantum mechanics, has opened the door to sophisticated methods of addressing complex problems. This heralds a new era of technological advancement that stretches beyond conventional boundaries and into the realm of previously unimaginable. Since this pivotal moment, our focus has shifted from merely inventing new tools to enhancing these tools at an atomic and molecular scale, seeking not only to create but also to refine and perfect the mechanisms that underpin our daily lives, pushing the limits of what was previously thought possible.

The interdisciplinary nexus of quantum mechanics and nanoscience is at the forefront of pioneering advancements in material science. It is driven by exploring quantum materials to see how to manipulate their properties and macroscopic behavior<sup>1</sup> highlighting the transformative potential of these materials when manipulated via external stimuli, and introducing new quantum states and functionalities. Quantum materials are attractive because of the potential to tailor their electronic, making properties that make them indispensable for future technologies<sup>2</sup>, demonstrating the practical applications of these advancements in the construction industry, and showcasing their broad potential. The fusion of quantum mechanics and material science is revolutionizing industries from electronics and medicine by enabling unprecedented control and enhancement of quantum materials at the nanoscale. A primary ambition in molecular electronics is to emulate nature's approach in constructing intricate circuits or electronically functional entities through the process of molecular self-assembly from solutions<sup>3</sup>. This synergy forecasts a transformative era where these materials' meticulous manipulation and optimization will unlock new possibilities beyond current technological and medical frontiers<sup>4,5</sup>. Despite nanosystems and devices' promising performance characteristics, their transition into practical applications is contingent on economic viability<sup>6</sup>. This underscores the importance of cost-effective approaches in nanotechnology, advocating for using self-assembly in nanoscience to combine efficiency with economic feasibility, thereby enhancing the potential for widespread adoption and practical use.



The journey ahead is filled with challenges and prospects in nanoporous material science. Particularly in catalysis, achieving high selectivity and yield is a principal objective. This necessitates the precise engineering of catalytic particles through nanoparticle synthesis and self-assembly, ensuring they facilitate only specific reactions efficiently and with more significant energy savings. Moreover, aiming for a uniform pore size distribution is crucial for enhanced selectivity in adsorption and catalysis<sup>7</sup>. Building on the intersection of quantum mechanics and nanoscience, this research delves into the intricacies of nanoporous networks, recognizing their pivotal role due to their exceptional properties. Advanced textural characterization has become a cornerstone in linking the structural nuances of nanoporous materials—such as surface area, pore size, and connectivity—to their performance in various processes<sup>8</sup>. This exploration is nestled between recent advances in material manipulation at the quantum level and innovative applications in nanostructure self-assembly, setting the stage for a deeper understanding of material science's future directions.

The emergence of nanoscience has sparked a resurgence in the field, fueled by the innovative notion that artificial nanostructures capable of self-assembly can be tailored for precise functions to enhance regenerative processes.<sup>9</sup> Self-assembly on surface materials represents another frontier in our quest to manipulate materials at the most fundamental levels, especially highlighted by the birth of scanning tunneling microscopy (STM)<sup>10</sup>. STM has revolutionized surface material science, allowing for unprecedented manipulation and observation of atomic and molecular interactions<sup>11</sup>. Furthermore, the reversibility of non-covalent interactions such as van der Waals forces, hydrogen bonding, and metal-ligand bonds, facilitate the supramolecular coordination of molecules on top of metallic surfaces<sup>12</sup>. These interactions can be used to create surface-confined metallosupramolecular nanostructures which can form wide-range assemblies depending on the choice of precursor molecule<sup>13</sup>. In particular, molecules with  $\pi$ -orbitals are of significant interest for research due to their ability to transfer charge to or from the surface<sup>14</sup>.

Several factors significantly influence the epitaxial development of organic thin films atop inorganic surfaces. These include the molecule and substrate's size and symmetry, the alignment of their lattice constants, and the interactions both between the molecules themselves (adsorbate-adsorbate) and between the molecules and the surface (adsorbate-substrate)<sup>15</sup>. This often results in hydrogen-bonded nanostructures of unique shapes which can also be achieved on surfaces. Such structures often exhibit flat and extended  $\pi$ -systems featuring peripheral functional groups. Such structures are especially conducive to forming distinct planar arrangements<sup>16</sup>.

Due to their distinct cavities and hydrogen bonding interactions, organic molecules have become more and more important in self-assembled materials in the midst of these revolutionary developments. These molecules illustrate the sensitive interaction between organic chemistry and materials science and show promise for complex self-assembly when organized on metallic surfaces<sup>16</sup>. This is often attributed to the delocalized nature of  $\pi$  bonding and  $\pi^*$  antibonding orbitals. This synergy produces complex structures that are essential for creating new materials with specialized functions and bridging the gap between theoretical innovation and practical application in nanotechnology as potential organic photovoltaic (OPV) materials.

Over the last decade, there has been remarkable progress in developing ultrathin organic films and multilayered structures, showcasing a broad spectrum of optoelectronic characteristics<sup>17</sup>. These advancements underscore the potential of organic molecules in self-assembled materials, particularly as OPVs. This emerging field exploits the unique properties of organic films to enhance light absorption and charge separation due to their isomeric effect,

which leads to the delocalization of  $\pi$ -electrons, and in turn causes a significant increase in electronic polarizability<sup>18</sup>.

Self-assembly offers distinct pathways for creating nanoscale supramolecular configurations, i.e., sophisticated and widespread molecular structures that are highly ordered<sup>19</sup>. This includes self-assembly on metallic surfaces<sup>20</sup> tools such as STM at low temperature for their principal analysis and low-energy electron diffraction (LEED)<sup>21</sup> to check the patterns of a highly ordered structure can be employed to show the emerging clusters and structures<sup>22–26</sup>.

The exploration of nonmetal atomic species-mediated self-assembled two-dimensional (2D) networks showcases the important role of hydrogen bonding in stabilizing such structures, mainly through the controlled addition of halogen atoms<sup>27,28</sup>. This strategy enhances the stability of self-assembled frameworks and introduces new avenues for manipulating charge transfer and stability, thereby altering the packing of 2D structures on metallic surfaces. In this way, alternative packings may appear, and more stable configurations such as a metal-organic frameworks (MOFs) can be corroborated via density functional theory (DFT) calculations<sup>29</sup>. This demonstrates the essential role DFT<sup>30</sup> calculations may play by demonstrating both the stability of packings and exploring their hydrogen bonding modes.

To expand upon the initial analysis, this study investigates the theoretical aspects of 1,3,4-tris[4-(pyridine-4-yl)-[1,1'-biphenyl]]benzene (TPyPPB) on Ag(111). We also extend our study to include systems modified with Cl adatoms, which may induce new self-organized structures. These adatoms play a significant role in 2D molecular packings, interacting with the adsorbed species via Cl $\cdots$ H bonding, akin to the Br  $\cdots$ H interactions discussed in Refs. 27 and 28. Such extensions allow for a nuanced exploration of the effects of halogen bonding on the structural and electronic properties of the system. DFT plays a pivotal role here, positing that electron density accurately determines a system's ground state<sup>30</sup>. By employing electron density-based functionals, DFT effectively models quantum-level electronic structures and properties, thereby facilitating the theoretical design of materials and offering a more efficient alternative to other more computationally expensive methods<sup>31,32</sup>.

STM has emerged as an essential tool for the characterization of nanoscale materials, offering an unprecedented window into the atomic and molecular intricacies of surfaces. Its critical role in precisely examining large organic molecules and carbon-based nanostructures enhances our understanding of material properties at the nanoscale. By facilitating the direct observation of atomic arrangements and surface electronic structures, STM has become indispensable in correlating theoretical predictions with actual material behaviors, and plays an essential role in the advancement of the field of nanomaterials science<sup>33</sup>.

This research delves into both theoretical predictions and experimental measurements of TPyPPB on the Ag(111) surface, by providing a holistic view of its structure. This is accomplished by calculating their vibrational modes, electronic, and optoelectronic properties by employing time-dependent density functional theory (TDDFT) to calculate their optical absorption spectra<sup>34</sup> and insight into their excitonic activity in the optical limit<sup>35</sup>. This dual approach enhances our understanding of the interaction between the organic molecule and the metallic surface. It paves the way to identifying potential applications in nanotechnology and materials science. Through this comprehensive study, we endeavor to bridge the gap between theoretical simulations and practical characterizations, shedding light on the intricate behaviors of molecular nanoporous assemblies on surfaces.

TPyPPB on metallic surface can lead to the formation of a highly ordered networks as previous work detailed 29 by depositing TPyPPB on Cu(111) with a range of annealing temperatures 400-500 K approximately. This

work studied two possible packings of TPyPPB on Ag(111). First, the deposition of TPyPPB on Ag(111) at RT lead to the formation of a highly ordered porous self-assembled monolayer structure. However, by the deposition of the precursor Dichloro(1,10-phenanthroline)Platinum(II) on top of the metallic surface with the dehalogenation performed by annealing and sputtering followed by TPyPPB deposition created a new highly ordered monolayer structure reported as inverted packing due to the interplay of Cl atoms within the hydrogen bonding. Additionally, the performance of depositing the precursor and the dehalogenation on a previous p-SAM reported during this work as triangular packing lead to a effective separation of Cl into the triangular nanoporous.

As previous work depicted in 36 theoretical spectroscopy tools such as FTIR are able to characterize this monolayer materials and differentiate changes into the system such as Py-Cu-Py bonding mode by analyzing the ratio of the intensities between peaks. During this work it was also performed FTIR simulations for both packings with and without Cl atoms giving an insight into the characterization and having a clear difference in the intensity peak ratios. The theoretical spectroscopy analysis were complemented by analyzing TPyPPB isolated with vibrational spectroscopy methods as Raman and optical absorption spectroscopy. Furthermore, both packings are compared experimentally and theoretically with STM.

## 1.1 Problem Statement

The rapid evolution of material science, driven by quantum mechanics and nanoscience, presents an unprecedented opportunity to explore and manipulate quantum materials experimentally, and direct such research using theoretical insight. This research aims to address the critical challenge of designing and characterizing nanoporous networks on metallic surfaces, explicitly focusing on the interaction of 1,3,4-tris[4-(pyridin-4-yl)-[1,1'-biphenyl]]benzene (TPyPPB) on Ag(111). TPyPPB self-assembles in several different configurations depending on the metallic surface. Specifically, it can form large pores with possible applications as an accommodating material for various molecules and atoms, enabling its function as a nanoreactor for catalytic processes<sup>29</sup>. It is also possible to use 2D self-assembly packing configurations on Ag(111) to explore the stability of adding Cl atoms, complemented with an in-depth theoretical spectroscopy analysis. This dual approach enhances our understanding of the interaction between the organic molecule and the metallic surface and its interaction with a deposited halogen atom, such as Cl. Furthermore, this study includes a detailed analysis of charge transfer processes, offering insights into the electronic properties of the charge-transferred between adsorbates or between the adsorbate and the slab. In this way we provide insight into the future of nanoporous materials, emphasizing the role of self-assembly in promoting economic and efficient material design. Through this structured exploration, we encapsulate the synergy between theoretical insights and practical advancements, underscoring the transformative potential of quantum materials.

To do so, we have performed DFT calculation using linear combinations of atomic orbitals (LCAOs), plane waves (PW), and real space (RS) to represent the Kohn-Sham (KS) wavefunctions<sup>37</sup> with the Perdew-Burke-Ernzerhof (PBE) implementation of the generalized gradient approximation (GGA) for the exchange-correlation (xc) functional<sup>38</sup> and Grimme's D3 semi-empirical correction to describe long-ranged van der Waals (vdW) interactions<sup>39</sup>. Gritsenko-Leeuwen-Lenthe-Baerends (GLLB-SC) xc functional was also used to obtain the derivative discontinuity correction to the Kohn-Sham energy gap, as employed by the LCAO-TDDFT-k- $\omega$  code<sup>35</sup>. This is implemented with

the projected-augmented wave (PAW) method<sup>40</sup> based code GPAW<sup>41</sup>, within the atomic simulation environment (ASE)<sup>42</sup>. ASE is an adaptable tool to perform several different calculations expanding GPAW's capabilities to perform Grimme's correction<sup>39</sup> and characterize with STM, and vibrational spectroscopy<sup>43</sup> DFT based simulations. Additionally, Bader's charge analysis technique<sup>44</sup> emerges as a crucial tool, offering detailed insights into electron localization and charge distribution.

## 1.2 General and Specific Objectives

### 1.2.1 General Objective

This research aims to untangle the complicated physiochemical properties and possible uses of highly ordered porous self-assembled monolayer (p-SAM) networks on metallic surfaces. By emphasizing the intricate self-assembly process, the research aims to further our comprehension of these 2D structures. Specifically, we investigate their formation stability with DFT and the characterization, delving into their potential applications in various domains, including surface analysis, Chlorine separation, charge transfer, and photovoltaic properties. For this purpose, theoretical calculations are performed and compared with experimental measurements.

### 1.2.2 Specific Objectives

- Analyze with STM measurements the on-surface synthesis of TPyPPB on Ag(111) with and without the presence of Cl atoms.
- Perform DFT simulations of both highly ordered packings on Ag(111) to study their stability by the difference in the formation energies per TPyPPB molecule.
- Use the Bader analysis to depict how the charge transfer occurs to the monolayer being adsorbed on the metallic surface.
- Characterization with FTIR simulations of TPyPPB on Ag(111) for both packings with and without Chlorine atoms.
- Characterize TPyPPB using Raman simulations.
- Provide an insight into the possibly OPV application of TPyPPB by simulating the optical absorption spectrum complemented with a look into exciton-density activity to see the shifts in energy with respect to HOMO and LUMO.

## 1.3 Overview

This thesis delves into the complexities of characterizing nanoporous networks on metallic surfaces, underscoring the synergy between advanced theoretical frameworks and empirical insights. Leveraging the robustness of DFT and

cutting-edge spectroscopic analyses, we offer a comprehensive examination of TPyPPB on the Ag(111) surfaces. This study is structured to progressively build from a foundational understanding of theoretical principles toward nuanced applications in material science. Through meticulous simulation and comparison with experimental measurements, we illuminate the physicochemical mechanisms underpinning the formation and characterization of these intricate networks, pushing the frontiers of nanotechnology and offering a scaffold for future exploration. Through a structured five-chapter narrative, we delve into theoretical backgrounds, methodological approaches, detailed results, and conclusive insights supplemented by computational data. The first chapter states why we study this system on the metallic surface and how we address the problem by discussing the state-of-the-art, reviewing the literature, and considering past works for the methodology and experimental results.

The second chapter presents an in-depth theoretical background justifying how we have performed our theoretical spectroscopy calculations and the many-body problem. We briefly review the fundamentals of DFT, explain TDDFT, and introduce the spectroscopic methods employed throughout this work. Finally, we provide a short introduction to the system we will study in this thesis, namely, TPyPPB on Ag(111).

The third chapter is broken into two main parts: the project's experimental setup and computational details. Specifically, we review the equipment details and both where and how the experiments were carried out. This is followed by a detailed review of how our DFT calculations and complementary simulations based on TDDFT and theoretical spectroscopy were performed.

The fourth chapter is also divided into two main sections. The first includes the experimental and computational results, which we both compare and discuss. In addition, some of our theoretical results have no direct experimental data to be compared to, but may be performed experimentally in the future. Finally, the fifth chapter summarizes all the most important findings of the work presented during this thesis project, along with an outlook for future work.

## Chapter 2

# Theoretical Background

The development of quantum mechanics transformed our ability to simulate theoretical processes, primarily by employing  $\Psi$ , the wavefunction of electrons, to describe their behavior precisely. This novel method makes it possible to accurately represent quantum processes and infer macroscopic features from tiny states. We look to an approximation that simplifies this complicated reality: electron density as a function, searching for a workable way to realize this potential. By giving a feasible substitute for solving for  $\Psi$  directly, this approximation hopes to pave the way for a more accurate and efficient understanding of material behaviors at the quantum level.

## 2.1 Density Functional Theory

### 2.1.1 The Schrödinger Equation

The Schrödinger equation describes how the quantum state of a physical system changes over time using a probability function known as a wavefunction  $\Psi$ . The foundational equation of quantum mechanics provides a way to calculate the wave function of a system, which encapsulates the probabilities of finding particles in various states, in this case, electrons.

Formally, the time-dependent Schrödinger equation is given by:

$$i\hbar \frac{\partial}{\partial t} \Psi(\mathbf{r}, t) = \hat{H}\Psi(\mathbf{r}, t), \quad (2.1)$$

where  $i$  is the imaginary unit,  $\hbar$  is the reduced Planck's constant,  $\Psi(\mathbf{r}, t)$  is the wave function of the system,  $\mathbf{r}$  represents the coordinates,  $t$  denotes time, and  $\hat{H}$  is the Hamiltonian operator which represents the total energy of the system.

For many applications, especially in stationary states where the system's properties do not change over time, the time-independent Schrödinger equation is often used:

$$\hat{H}\psi(\mathbf{r}) = E\psi(\mathbf{r}), \quad (2.2)$$

Here,  $E$  represents the energy eigenvalues associated with the corresponding eigenfunctions  $\psi(\mathbf{r})$  of the system.

Eq (2.1) and Eq (2.2) possess an endless array of solutions, denoted as  $\psi_i$ , each corresponding to an eigenvalue  $E_i$ . Thus, a linear combination of these discrete separable solutions makes up the overall solution:

$$\Psi(\mathbf{r}, t) = \sum_{i=0}^{\infty} c_i \psi_i(\mathbf{r}) e^{-iE_i t/\hbar}, \quad (2.3)$$

The wavefunction,  $\Psi$ , for a quantum system is defined by the equation 2.3 in terms of position,  $\mathbf{r}$ , and time,  $t$ . Each term in the infinite series is built by combining a time-dependent phase factor with the stationary state wavefunction,  $\psi_i(\mathbf{r})$ . The amplitude of each stationary state contributing to the overall wavefunction is represented by the coefficient  $c_i$ , which indicates the likelihood that the system will be discovered in that state. Each component wavefunction's evolution over time is encoded by the phase factor,  $e^{-iE_i t/\hbar}$ , which is controlled by the energy  $E_i$ . The energy level of the  $i$ -th state is indicated by  $E_i$ , while the reduced Planck's constant integral to the quantum description of the system is represented by  $\hbar$ . This detailed representation reflects the geographical and temporal evolution of the quantum system's state and depicts its dynamic behavior.

### 2.1.2 The Many-Body Problem

The wavefunction  $\Psi(\mathbf{r}, t)$  of a system such as a hydrogen atom and its states is described by Schrödinger's equation described above. However, in case we have an extensive system composed of a set of electrons and atoms, e.g., a crystalline network, to find a solution to Schrödinger's equation, the wavefunction's definition will hinge on the specific locations and spins of the nuclei and electrons present as:

$$\Psi = \Psi(\mathbf{r}_1, s_1; \mathbf{r}_2, s_2; \dots; \mathbf{r}_N, s_N; \mathbf{R}_1, S_1; \mathbf{R}_2, S_2; \dots; \mathbf{R}_M, S_M), \quad (2.4)$$

Eq 2.4 provided represents the wavefunction,  $\Psi$ , for a many-body quantum system, which encompasses both electrons and nuclei within a single framework. In this case, the position vectors and spin variables of the  $i$ -th electron are represented by  $\mathbf{r}_i$  and  $s_i$ , respectively, and those of the  $j$ -th nucleus by  $\mathbf{R}_j$  and  $S_j$ . By considering the interactions between all particles, this wavefunction captures the system's complete quantum state, a function of the locations and spins of all  $N$  electrons and  $M$  nuclei. Such a thorough description is essential for precise behavior prediction of the system and comprehension of the quantum mechanical interactions in complex materials and molecules. To build a redefined Hamiltonian for the many-body problem, we can decompose it by considering the following potentials in the system: the coulomb interaction of the electron-electron repulsion, the attraction of the electron-towards the nuclei, the repulsion between nuclei-nuclei, also considering the kinetic energy of electrons and nuclei. So our redefined Hamiltonian will be made of 5 terms as:

$$\hat{H} = \hat{T}_e + \hat{T}_n + \hat{V}_{ee} + \hat{V}_{en} + \hat{V}_{nn}, \quad (2.5)$$

Then, the eq 2.5 in a detailed way can be expressed as:

$$\hat{H} = -\frac{1}{2} \sum_i^{N_e} \nabla_i^2 - \frac{1}{2} \sum_J^{M_n} \frac{1}{M_J} \nabla_J^2 + \frac{1}{2} \sum_{i \neq j} \frac{1}{|\mathbf{r}_i - \mathbf{r}_j|} - \sum_{i,J} \frac{Z_J}{|\mathbf{r}_i - \mathbf{R}_J|} + \sum_{I \neq J} \frac{Z_I Z_J}{|\mathbf{R}_I - \mathbf{R}_J|}, \quad (2.6)$$

Here,  $\hat{H}$  denotes the Hamiltonian operator, capturing the system's total energy, including the kinetic energies of electrons and nuclei (first two terms) and their electrostatic interactions (last three terms).  $N_e$  and  $M_a$  represent the number of electrons and nuclei, respectively,  $\mathbf{r}_i$  and  $\mathbf{R}_J$  are the position vectors of the  $i$ -th electron and  $J$ -th nucleus,  $Z_J$  is the charge of the  $J$ -th nucleus, and  $M_J$  is the mass of the  $J$ -th nucleus. The Laplacian operator,  $\nabla^2$ , reflects the Laplacians concerning the electronic and nuclear coordinates (lower case letter electrons, upper case letter nucleus). All by using atomic mass units stating electron mass, proton charge, and Planck's constant to the unity ( $m_e = e = \hbar, a_0 = 1$ ). These conditions underpin atomic units, significantly simplifying the mathematical expressions and computational models in quantum physics by reducing the number of variables and constants in equations.

### 2.1.3 Born-Oppenheimer approximation

Given the challenge of finding solutions within the framework of the many-body problem and considering the mass ratio between protons and electrons  $\frac{m_p}{m_e} \approx 1836$ , the Born-Oppenheimer approximation (BOA)<sup>45</sup> emerges as a pivotal strategy. This approach, also recognized as the adiabatic approximation<sup>46</sup>, is instrumental in disentangling the movements of nuclei and electrons when analyzing molecular systems. Rooted in the significant mass difference between electrons and nuclei, the BOA assumes that electrons, owing to their lesser mass and resultant higher velocity, can instantaneously realign with any shifts in nuclear positions. This assumption allows for the molecular wavefunction to be partitioned into distinct electronic and nuclear components, thereby transforming the intricate issue of molecular dynamics into far more tractable subsets. Through this simplification, the BOA addresses the computational and conceptual hurdles posed by the many-body problem. It lays the groundwork for in-depth exploration and understanding of molecular behavior and properties. So, considering  $\mathbf{r} = \mathbf{r}_i$  and  $\mathbf{R} = \mathbf{R}_j$  the total wavefunction  $\Psi$  can be described as a product of two wavefunctions:

$$\Psi(\mathbf{x}) = \psi_{\text{elec}}(\mathbf{r}_1, s_1; \mathbf{r}_2, s_2; \dots; \mathbf{r}_{N_e}, s_{N_e}) \otimes \chi(\mathbf{R}_1, S_1; \mathbf{R}_2, S_2; \dots; \mathbf{R}_{M_a}, S_{M_a}), \quad (2.7)$$

Here, the function  $\psi_{\text{elec}}$  is the electron-only wavefunction, and  $\chi$  is the nuclear-only wavefunction. Therefore, to solve the BO approximation we can simplify the many-body Hamiltonian problem to a problem just in terms of the electrons with an electronic Hamiltonian  $\hat{H}_e$ :

$$\hat{H}_e = -\frac{1}{2} \sum_{i=1} \nabla_{r_i}^2 + \frac{1}{2} \sum_{i,j} \frac{1}{|r_i - r_j|} + V_{\text{ext}}^{R_1, \dots, R_{M_a}}(\mathbf{r}_1, \dots, \mathbf{r}_{N_e}), \quad (2.8)$$

On this approximation of the electronic Hamiltonian, it was added the external potential  $V_{\text{ext}}$ . Therefore, as the nuclei interact through electromagnetic forces within electrons that interaction is considered by the external potential term. Therefore, it is stated that the electronic wavefunction depends parametrically on the nuclear position coordinates  $\mathbf{R}_1, S_1; \dots; \mathbf{R}_{M_a}, S_{M_a}$ . Consequently, we derive the "frozen-nuclei" Schrödinger equation.

$$\hat{H}_e \psi_{\text{elec}}(\mathbf{r}_1, s_1; \mathbf{r}_2, s_2; \dots; \mathbf{r}_{N_e}) = \varepsilon(\mathbf{R}_1, S_1; \dots; \mathbf{R}_{M_a}, S_{M_a}) \psi_{\text{elec}}(\mathbf{r}_1, s_1; \mathbf{r}_2, s_2; \dots; \mathbf{r}_{N_e}, s_{N_e}) \quad (2.9)$$

Eq 2.9 states into a single framework to describe the solution of the electron wavefunction with the eigenvalues  $\varepsilon_i$ . These potential energy surfaces represent the electronic energy of the system. By disregarding the kinetic energy of



the nuclei, we obtain:

$$\begin{aligned}
\hat{H}_e\Psi(\mathbf{x}) &= \hat{H}_e\chi(\mathbf{R}_1, S_1; \mathbf{R}_2, S_2; \dots; \mathbf{R}_{M_a}, S_{M_a})\psi_{\text{elec}}(\mathbf{r}_1, s_1; \mathbf{r}_2, s_2; \dots; \mathbf{r}_{N_e}, s_{N_e}) \\
&= \chi(\mathbf{R}_1, S_1; \mathbf{R}_2, S_2; \dots; \mathbf{R}_{M_a}, S_{M_a})\hat{H}_e\psi_{\text{elec}}(\mathbf{r}_1, s_1; \mathbf{r}_2, s_2; \dots; \mathbf{r}_{N_e}, s_{N_e}) \\
&= \varepsilon(\mathbf{R}_1, S_1; \dots; \mathbf{R}_{M_a}, S_{M_a})\Psi(\mathbf{x})
\end{aligned} \tag{2.10}$$

In this manner, the electronic and nuclear parts of the Hamiltonian can be completely decoupled. Additionally, the much more massive nuclei can be treated as classical point particles with a high degree of accuracy. Henceforth, we will use  $\hat{H}$ ,  $\Psi$ , and  $E$  to refer to the electronic Hamiltonian  $\hat{H}_e$ , wavefunction  $\psi_{\text{elec}}$ , and eigenenergies  $\varepsilon$ . Although the many-body electronic wavefunction provides all the necessary information, its exact calculation can only be performed for a small system with few electrons and atoms.

### 2.1.4 Periodic systems

Periodicity, evident in structures such as crystalline networks, simplifies the complex task of determining wave functions across a system. With this periodic framework, solving each component individually is manageable, given the sheer number of potential solutions and the inefficiency of such an approach.

The idea of periodicity is crucial for navigating these difficulties, and it leads to the application of the Floquet theorem<sup>47</sup>, also known as Bloch's theorem in condensed matter physics. It's interesting to note that Bloch later applied this theory to crystalline materials, building on work done by Floquet and showing how closely periodic systems and their quantum states are related. This fundamental idea argues that it is possible to elegantly simplify solutions to the quantum states inside of periodic potentials. This makes it easy to analyze material properties at the quantum level. Therefore, in preparation for a more thorough examination of this theorem, it is recognized that Floquet's groundbreaking work served as the foundation for what condensed matter physicists refer to as Bloch's theorem, emphasizing the ubiquitous importance of periodicity in comprehending material behaviors. After discussing periodicity in material science and the fundamental role of Floquet's discoveries, we move on to a particular use of these ideas in condensed matter physics. This leads us to Bloch's Theorem, a fundamental concept in quantum mechanics applied to crystalline solids<sup>48</sup>.

**Theorem 1. Floquet/Bloch's Theorem:** For an electron subjected to a periodic potential, the eigenstates are given by:

$$\psi_{n,\mathbf{k}}(\mathbf{r}) = e^{i\mathbf{k}\cdot\mathbf{r}} u_{n,\mathbf{k}}(\mathbf{r}), \tag{2.11}$$

In this context of eq 2.11,  $\mathbf{k}$  is defined as a wavevector located in the first Brillouin zone (BZ)<sup>49</sup>, while  $u_{n,\mathbf{k}}(\mathbf{r})$  is characterized as a function exhibiting the same periodicity in space as that of the supercell. This is mathematically expressed as:

$$u_{n,\mathbf{k}}(\mathbf{r} + \mathbf{R}_n) = u_{n,\mathbf{k}}(\mathbf{r}), \tag{2.12}$$

where  $\mathbf{R}_n$  symbolizes a lattice vector in the form:

$$\mathbf{R}_n = n_1\mathbf{a}_1 + n_2\mathbf{a}_2 + n_3\mathbf{a}_3, \tag{2.13}$$

with each of  $n_1, n_2$ , and  $n_3 \in \mathbb{Z}^+$ . This delineation suggests that it is feasible to approach the solution of the Schrödinger equation for each distinct value of  $\mathbf{k}$  independently. It establishes a correspondence principle: if a system exhibits periodicity, then a periodic external potential, consistent and unaltered by translational transformations, should also be present.

$$\hat{v}_{ext}(\mathbf{r} + \mathbf{R}_n) = \hat{v}_{ext}(\mathbf{r}), \quad (2.14)$$

Eq. 2.14 shows how an external potential  $\hat{v}_{ext}(\mathbf{r})$ . This periodicity and uniform consistency across the lattice for any translation underscore the crystalline structure's inherent symmetry and regularity. By defining a unit cell, which essentially acts as the smallest repeating unit within the crystal lattice, this periodic framework allows for a systematic and three-dimensional stacking process that meticulously reconstructs the entire crystal lattice. This approach to understanding crystalline structures leverages the concept of lattice vectors  $\hat{a} = a_1 + a_2 + a_3$ , which are fundamental to describing the crystal's geometry and spatial arrangement. The integers  $\alpha_i$  and the lattice vectors  $\hat{a}$  play a crucial role in this context, providing a mathematical and physical basis for the crystal's periodicity. These vectors define the dimensions and orientation of the unit cell, encapsulating the crystal's structural essence. Consequently, the unit cell can be visualized as a parallelepiped, a three-dimensional geometric figure whose edges are formed by these primitive vectors.

The volume of the unit cell, a key parameter, is then determined by the scalar triple product of the lattice vectors:

$$\Omega = |\mathbf{a}_1 \cdot (\mathbf{a}_2 \times \mathbf{a}_3)|, \quad (2.15)$$

The kinetic and Coulombic components of the Hamiltonian exhibit stability during lattice translations  $\mathbf{R}_n$ , indicating that the Hamiltonian for a periodic structure is invariant under such spatial shifts. This invariance implies that the Hamiltonian and the translation operations share identical eigenstates because of the translational symmetry. So our 2.2 which satisfies the **Floquet/Bloch's Theorem** stated in 2.11 is given by:

$$\left[ -\frac{1}{2} \nabla^2 + \hat{v}_{ext}(\mathbf{r}) \right] \psi_{n,\mathbf{k}}(\mathbf{r}) = E_{n,\mathbf{k}} \psi_{n,\mathbf{k}}(\mathbf{r}), \quad (2.16)$$

### 2.1.5 Reciprocal space

Understanding crystalline materials' structural and electronic properties requires a comprehensive approach extending beyond real space's confines. Reciprocal space is a crucial tool for studying crystals. It provides a unique perspective for physicists and materials scientists to analyze diffraction patterns and electronic behaviors of crystals with enhanced clarity and precision. Transitioning our analysis to reciprocal space helps us better understand these properties. Mathematic and computational techniques, such as Fourier transforms, are indispensable for probing the periodic structures of crystals. This shift not only facilitates a deeper understanding of the crystalline properties at the atomic level but also enables the effective use of computational models to predict and analyze material behaviors. As we delve into the reciprocal lattice, we prepare to unravel the intricacies of crystal structures through the lens of the Fourier series, setting the stage for the subsequent detailed exploration. Introducing the reciprocal lattice is pivotal to exploring the properties of a crystal through the Fourier series<sup>46</sup>. This necessitates the formulation of the

reciprocal lattice's primitive vectors,  $b_1$ ,  $b_2$ , and  $b_3$ , per the specified guideline:

$$\mathbf{b}_1 = 2\pi \frac{\mathbf{a}_2 \times \mathbf{a}_3}{\Omega}, \quad (2.17)$$

analogously to eq 2.17 for  $b_2$  and  $b_3$  considering that all three indices are not equal. Following the definition of the reciprocal lattice, encompassing all vectors  $\mathbf{G}_\beta$ , a direct implication of Bloch's theorem emerges. This theorem stipulates that all observables within the system can be expressed through Fourier expansion using the reciprocal lattice vectors  $\mathbf{G}_\beta$ :

$$\mathbf{G}_\beta = \beta_1 \mathbf{b}_1 + \beta_2 \mathbf{b}_2 + \beta_3 \mathbf{b}_3, \quad (2.18)$$

taking  $\beta_i \in \mathbb{Z}^+$ . All this satisfies the relation of eq 2.17 between eq 2.13 by:

$$\mathbf{a}_i \cdot \mathbf{b}_j = 2\pi \delta_{i,j}, \quad (2.19)$$

In the context of performing practical calculations, eq 2.19 indicates that for every vector  $\mathbf{G}_\beta$ . from the direct lattice and corresponding vector  $\mathbf{R}_\alpha$  from the reciprocal lattice, the expression  $\exp(i\mathbf{G}_\beta \cdot \mathbf{R}_\alpha) = 1$  holds true. This relationship underscores the intrinsic periodicity and symmetry between the direct and reciprocal lattice frameworks, facilitating the simplification<sup>46</sup>.

Given this characteristic, it's logical to confine the examination of the band structure to merely a single unit cell within the reciprocal lattice. For instance, one might focus on wavevectors  $\mathbf{k}$  situated within the primitive cell of the reciprocal lattice, which is the parallelepiped outlined by  $\mathbf{b}_i$ . However, in practical scenarios, considering  $\mathbf{k}$ -vectors located within a specific region of reciprocal space, known as the first Brillouin zone, is more advantageous. This zone is described as the region encompassing  $\mathbf{k}$  vectors closer to the origin ( $\mathbf{G}_\beta = 0$ ) than any other  $\mathbf{G}$ -vector. The construction of the first Brillouin zone involves identifying the planes that bisect all  $\mathbf{G}$ -vectors and then defining the smallest volume centered at  $\mathbf{G}=0$  bounded by these planes<sup>46</sup>.

The space occupied by the first Brillouin zone is identical to that of a primitive cell in the reciprocal lattice, hence its volume can be determined as follows:

$$\Omega_{BZ} = |\mathbf{b}_1 \cdot \mathbf{b}_2 \times \mathbf{b}_3| = \frac{(2\pi)^3}{\Omega}, \quad (2.20)$$

From eq 2.16, the wavevector  $\mathbf{k}$  signifies the system's periodic nature, while the integer  $\alpha$  represents separate eigenstates of the system at various eigenvalues. Furthermore, within the first Brillouin Zone, every wavevector  $\mathbf{k}$  is associated with a full spectrum of electronic bands denoted by  $\alpha$ . To illustrate, the electronic band structure of any solid material can be determined by calculating the eigenvalues  $E_{\alpha,\mathbf{k}}$  and graphically representing them along a specific path in reciprocal  $\mathbf{k}$ -space. The analysis can be limited to the restriction of  $\mathbf{k}_\ell$ :

$$\mathbf{k}_\ell = \frac{\ell_1}{N_1} \mathbf{b}_1 + \frac{\ell_2}{N_2} \mathbf{b}_2 + \frac{\ell_3}{N_3} \mathbf{b}_3, \text{ with } -\frac{N_i}{2} \leq \ell_i < \frac{N_i}{2}, \quad (2.21)$$

Eq 2.21 takes  $\ell_i, N_i \in \mathbb{Z}^+$ . The constrained  $\mathbf{k}$  values are defined by the first Brillouin zone, with any  $\mathbf{k}$  value beyond this zone being reducible to within the first Brillouin zone. To utilize Bloch waves for representing Kohn-Sham (KS) wavefunctions, selecting a finite set of sample points within the first Brillouin zone is necessary. The orbitals change

smoothly with  $\mathbf{k}$ , and calculations must converge for each sample point. A Monkhorst-Pack<sup>50</sup> grid of special<sup>51</sup>  $k$ -points as it is utilized for its impartial approach in choosing these points across an evenly distributed mesh

$$\mathbf{k}(\alpha_1, \alpha_2, \alpha_3) = \sum_{i=1}^3 \frac{2\alpha_i - N_i - 1}{2N_i} \mathbf{b}_i, \quad (2.22)$$

For  $\alpha_i = 1, \dots, N_i$ , where  $N_i$  specifies the quantity of points along the  $\mathbf{b}_i$  direction. Assessing numerous properties necessitates computing integrals over the Brillouin zone within reciprocal space. We can closely approximate these integrals using this discrete selection of  $k$ -points. For example, consider the mean of  $F$  equal to the integral calculation for a function  $F(\mathbf{k})$  which represents the average over the BZ<sup>51</sup> :

$$\bar{F} = \Omega_{BZ}^{-1} \int_{BZ} F(\mathbf{k}) d^3 \mathbf{k} \approx \sum_{\mathbf{k}} w_{\mathbf{k}} F(\mathbf{k}), \quad (2.23)$$

In this context,  $\Omega_{BZ}$  represents the Brillouin Zone (BZ) volume, and  $w_{\mathbf{k}}$  is the weight assigned to each  $\mathbf{k}$ -point in the summation. The integral is approximated by a weighted sum over the selected  $k$ -points within the first BZ. By exploiting the unit cell symmetries, we can streamline the calculation by eliminating redundant  $\mathbf{k}$ -points and adjusting their weights  $w_{\mathbf{k}}$ . This process gives rise to the so-called irreducible Brillouin Zone (IBZ), where, particularly in systems with high symmetry, the number of necessary  $k$ -points for calculations can be considerably minimized.

## 2.1.6 The Hohenberg-Kohn Theorems and implications

To assess the value of a theory in physics, we consider two key questions: does it accurately reflect reality, and does it capture all of its essential features?<sup>52</sup> As an example, consider equation 2.9, which theoretically solves many-body problems. However, while it demonstrates the potential for a theory to be complete in a specific domain, its complexity hinders its practical application, highlighting the importance of completeness and efficiency in evaluating a theory's practical value. Therefore, to make this calculation practical and less computationally expensive we just reduce by the following equation where the system has paired electrons (meaning each electron has a partner with opposite spin), and at a theoretical  $T \rightarrow 0$ :

$$\rho(\mathbf{r}) = 2 \sum_{i=1}^{N_e/2} \psi_i^*(\mathbf{r}) \psi_i(\mathbf{r}), \quad (2.24)$$

Eq 2.24 defines the electron number density,  $\rho(\mathbf{r})$ , which represents the average number of electrons per unit volume at any point  $\mathbf{r}$  in a spin-paired system. It achieves this by summing the probability densities of finding each electron across all occupied orbitals (up to  $N_e/2$ , where  $N_e$  is the total number of electrons). The probability density for each electron is calculated by squaring its wavefunction,  $\psi_i(\mathbf{r})$ , which describes the likelihood of finding that electron at a specific location. The summation considers the contributions from all occupied orbitals. The factor of 2 accounts for the two electrons with opposite spins that can occupy each orbital in this system. This comes from the Pauli exclusion principle<sup>53</sup>. The first Hohenberg-Kohn (HK) theorem states a surprising and fundamental connection in physics. It asserts that for a solid (or any system with fixed interactions between particles):

**Theorem 2. First Hohenberg-Kohn (HK) Theorem:** there's a unique and direct relationship between the ground-state wavefunction (which describes all electrons and their behavior) and the ground-state electron density (which describes the average number of electrons at each point in space), and is described as:

$$\rho(\mathbf{r}) = -n(\mathbf{r}), \quad (2.25)$$

Once we know the ground-state electron density, it remarkably carries all the information needed to determine the system's physical properties in its ground state, including the complete wavefunction of all electrons and their energies. This means that the ground-state energy of the system can be calculated as a function of the electron density (written as  $E[n(\mathbf{r})]$ ). To obtain this energy, we only need to know the interactions between the particles or the external potential (written as  $V_{ext}$ ) influencing the system. The proof of the theorem 2 can be found on 54. Considering that ground state functional has a unique ground state density as:

$$|\psi_{gs}\rangle = |\psi[n_{gs}]\rangle \quad (2.26)$$

Such a functional dependence enables the computation of any ground state observable  $\hat{O}$  as a density functional,  $O[n] \equiv \langle \psi[n] | \hat{O} | \psi[n] \rangle$ . The ground state energy can be expressed as

$$F[n(\mathbf{r})] = \min \langle \psi[n] | \hat{T}_e + \hat{V}_{ee} | \psi[n] \rangle, \quad (2.27)$$

In eq. 2.27  $F[n]$  represents the universal part of the ground state energy functional, and  $V_{ext}$  is an input if we rewrite eq. 2.27 as:

$$\int d\mathbf{r} V_{ext}(\mathbf{r}) n_{gs}(\mathbf{r}) + F[n_{gs}] = \mathbf{E}_{gs}, \quad (2.28)$$

As a consequence of these eq. 2.28 and 2.27, all the ground state properties, which we can describe as functionals, are described by the electron density for each kind of interaction by using the  $\rho(\mathbf{r})$ <sup>55</sup>, leading to a solution for  $\mathbf{E}_{gs}$  as follows in the theorem:

**Theorem 3. Second Hohenberg-Kohn (HK) Theorem:** For all densities  $n'_{gs}(\mathbf{r}) \neq n_{gs}(\mathbf{r})$ , where  $n_{gs}$  is the density at ground state corresponding to  $V_{ext}$ .

$$E[n_{gs}] < E'[n_{gs}] \iff E_{gs} = \min E[n^\circ]. \quad (2.29)$$

where  $n^\circ \in N$ , and  $N$  represents the collection of all possible electron densities that correspond to the ground state of a system, considering various  $V_{ext}$ . Then, the solution for electron energy contribution to the system by solving eq 2.9<sup>55</sup> can be rewritten in terms of four functionals dependent on the electron density<sup>56</sup> as:

$$E[n] = T[n] + E_H[n] + E_{ext}[n] + E_{xc}[n], \quad (2.30)$$

This equation breaks down the total energy of a system into different components, each represented by a functional that depends on the electron density  $n[\mathbf{r}]$ .

- $T[n]$ : The kinetic energy of the electrons.
- $E_H[n]$ : The Hartree energy<sup>57</sup> accounts for the classical electrostatic interaction between the electrons. This term is sometimes referred to as the self-interaction contribution.
- $E_{ext}[n]$ : The external potential energy arises from the electrons' interaction with external forces, such as the nuclei in a molecule.
- $E_{xc}[n]$ : The exchange-correlation energy. This term captures the complex effects of electron interactions not explicitly included in the other terms, such as quantum mechanical effects and the correlation between electrons.

Decomposing the total energy into functionals of the electron density  $n(\mathbf{r})$  significantly reduces the computational complexity. This approach avoids finding the individual wave function for every electron, focusing solely on the overall electron density distribution. This simplification translates to a dramatic decrease in the computational effort required for calculations.

### 2.1.7 Self-consistent Kohn-Sham approach

Beyond Hartree's approximation theory within a Self-consistent field<sup>57</sup> by implementing a trial change in the field of the electron density, The Kohn-Sham (KS)<sup>37</sup> approach revolutionized how we tackle the complex problem of describing systems with many electrons (n-electron problem). This method focuses on the electron density as the key variable instead of the individual wavefunctions of each electron. This is a significant shift compared to traditional approaches that require solving a  $3n$ -dimensional equation (e.g., 30 dimensions for 10 electrons)<sup>58</sup>. Indeed, exchange-correlation (XC) energy reflects the complex interactions between electrons, which is why it's often referred to as their "lively activities." Since this term is complex and difficult to calculate precisely, we rely on approximations. The accuracy of these approximations is crucial for the quality of results obtained from Density Functional Theory (DFT) calculations. In simpler terms, the closer the approximate XC energy is to the actual value, the better the overall quality of the DFT calculation<sup>58</sup>.

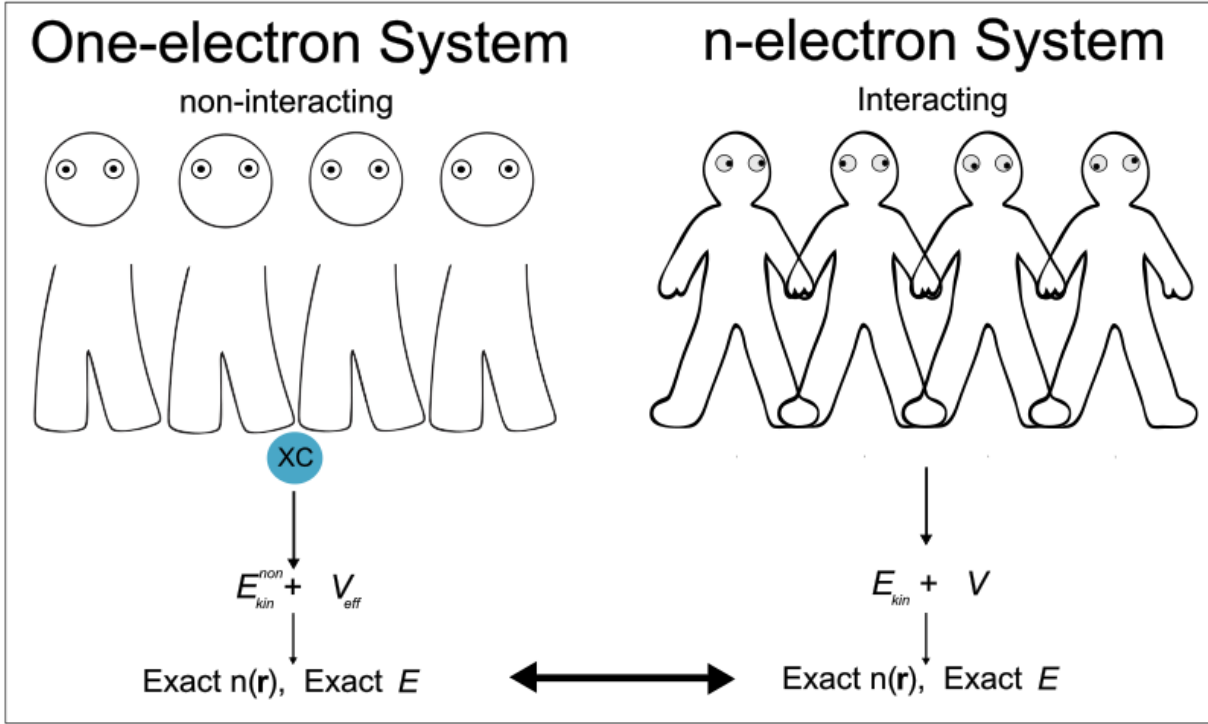


Figure 2.1: Kohn-Sham ansatz adapted from Ref. 58.

From fig. 2.1. The Kohn-Sham (KS) system acts as a stand-in for the real system. It consists of non-interacting electrons, but remarkably, it replicates the same electron density as the real system. It involves interactions between electrons but takes the effective potential, which approximates eq 2.28 better and costs less computational effort. Still, the best approximations ultimately depend on the XC selected for a specific system. The Kohn-Sham (KS) scheme, outlined in Fig. 2.2, provides a step-by-step approach to finding the essential properties of a system using the electron density by taking into account the KS Hamiltonian:

$$\hat{H}_{KS} = E_{kin}^{non} + V_{ext} + V_H + V_{XC} = -\frac{1}{2} + V_{eff}, \quad (2.31)$$

Of course, all terms of eq 2.31 are dependent on  $n[\mathbf{r}]$ , and  $V_{eff}$  as the effective potential includes the three potential terms. This iterative process of the numerical methods solution involves five key steps:

1. Starting with an initial guess for the electron density defined as  $\tilde{n}(\mathbf{r})$ .
2. Building a special potential  $V_{eff}$  that depends on the guessed electron density  $\tilde{n}(\mathbf{r})$

$$V_{eff}[\tilde{n}(\mathbf{r})] = V_{ext}(\mathbf{r}) + \int \frac{\tilde{n}(\mathbf{r}')}{|\mathbf{r} - \mathbf{r}'|} d^3\mathbf{r}' + V_{XC}[\tilde{n}(\mathbf{r})] \quad (2.32)$$

Eq. 2.32 describes the special potential  $V_{eff}$  that influences the electrons in the system by: the influence of the atomic nuclei on the electrons ( $V_{ext}$ ), the average repulsion between the electrons due to their shared space (Hartree potential), and the complex term ( $V_{XC}$ ) that accounts everything else such as the corrections for how the electrons move (kinetic energy) and the detailed interactions between them. This last term captures the key differences between the real system where electrons interact and the simplified system (KS system) where they don't.

3. Solve an equation similar to the Schrödinger equation, but with a special potential  $V_{eff}$ , to find the KS orbitals for each electron given a  $\phi_i$ ,

$$\left(-\frac{1}{2}\nabla^2 + V_{eff}[\tilde{n}(\mathbf{r})]\right)|\phi_i(\mathbf{r})\rangle = \epsilon_i|\phi_i(\mathbf{r})\rangle, \quad (2.33)$$

4. We can now estimate a more accurate new trial electron density  $\tilde{n}'(\mathbf{r})$  based on the recently obtained information about the electrons' behavior (KS wavefunctions  $\phi_i$ ),

$$\tilde{n}'(\mathbf{r}) = 2 \sum_i^{N/2} |\phi_i|^2, \quad (2.34)$$

The average number of electrons at any point in the system can be calculated by summing the contributions from the  $N/2$  most important wavefunctions, which describe the electrons with the lowest energy levels and are occupied by two electrons each.

5. The calculated electron density  $\tilde{n}(\mathbf{r})$  from the initial step is compared to the one used in the calculation  $\tilde{n}'(\mathbf{r})$ . This comparison is repeated (step 2,3, and 4) until the two densities become almost identical, reaching a state of "convergence" of the numerical methods. This iterative process is like a loop, as shown in Fig. 2.2.



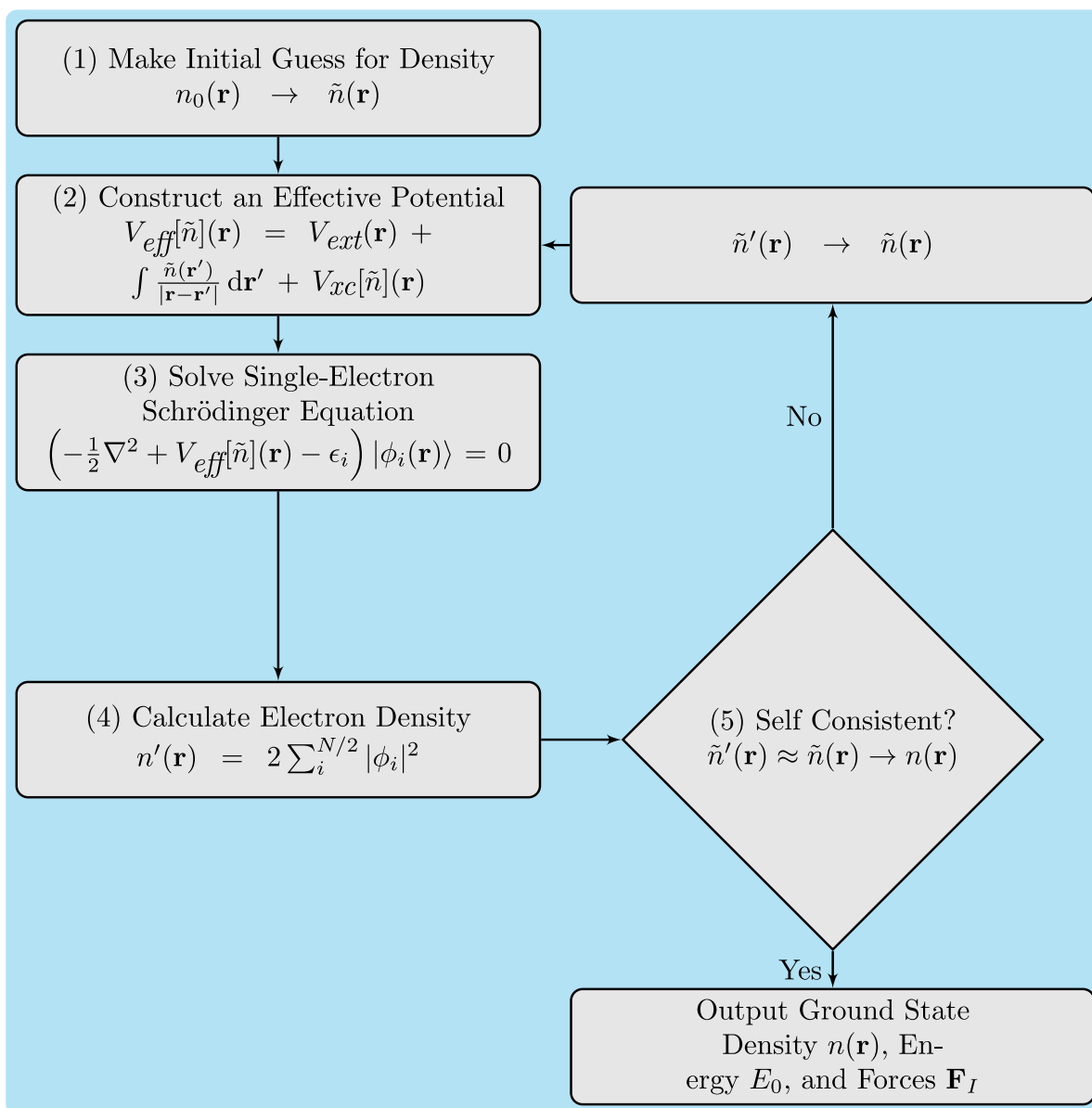


Figure 2.2: Illustrative KS self-consistent numerical algorithm flowchart, adapted from Ref. 59.

When the densities converge, the obtained electron density and the corresponding electron energies  $\epsilon_i$  represent the system's ground state with a certain level of accuracy. It's important to remember that the energies and

wavefunctions obtained from the Kohn-Sham (KS) approach ( $\epsilon_i$  and  $\phi_i$ ) don't directly correspond to the physical properties of individual electrons. However, the energy of the highest occupied KS orbital or HOMO ( $\epsilon_N$ ) relative to the vacuum level holds physical significance - it approximates the system's ionization energy. Additionally, the KS orbitals ( $\phi_i$ ) contribute to calculating the true physical electron density ( $n(\mathbf{r})$ ).

While exact expressions for the exchange-correlation potential  $V_{XC}$  are only attainable for simple systems with few atoms and not known for many body problems, the underlying principles and equations of KS theory are exact.

### 2.1.8 Exchange-Correlation (XC) Functionals

In quantum mechanics, the exchange-correlation (XC) functional is a key component of density functional theory (DFT), crucial for accurately describing the electronic structure of many-body systems. The XC functional is responsible for capturing the complex interplay between exchange, which stems from the wave function's antisymmetry, and correlation, which considers the mutual repulsion of electrons. Understanding and appropriately modeling these phenomena is vital for predicting various properties of atoms, molecules, and solids.

Within the framework of DFT, the XC functional is the essential factor in translating electron density into total energy. This functional is typically broken down into two components: exchange, which reflects electron exchange effects due to the Pauli exclusion principle, and correlation, which accounts for electron-electron interactions beyond simple exchange effects. The accurate treatment of exchange and correlation effects is critical for making reliable predictions of electronic properties, such as ionization potentials, electron affinities, bond dissociation energies, and electronic band structures.

Over the years, several approaches have been developed to formulate XC functionals, each with advantages and limitations. Among the most widely used are functionals based on the local density approximation (LDA), the generalized gradient approximation (GGA), and hybrid functionals<sup>58</sup>. These functionals vary in sophistication and complexity, offering a range of computational accuracy and efficiency tailored to the specific needs of various applications.

Understanding the principles underlying different XC functionals is crucial for selecting the most appropriate method for a given system and the desired level of accuracy. In this subsection, we delve into the intricacies of exchange-correlation functionals, exploring their theoretical foundations, computational performance, and practical implications for electronic structure calculations.

#### Local density approximation

LDA is one of the first xc functional to solve the homogeneous electron gas (HEG) system by improving the previous one proposed by Slater<sup>60</sup> to simplify and make less computational effort compared to Hartree-Fock (HF) calculations, all done by Perdew and Zunger<sup>61</sup>, as in a HEG system the electron density is a density which depends only on its position. LDA xc functional can be computed as:

$$E_{XC}^{LDA}[n(\mathbf{r})] = \int d^3\mathbf{r} n(\mathbf{r}) \epsilon_{XC}[n(\mathbf{r})] \quad (2.35)$$

Eq. 2.35 is a simple approach because it depends only on the electron density at each point (local). This characteristic makes it straightforward to incorporate into the Kohn-Sham (KS) scheme 2.2 from Ref. 60,

$$V_{XC}^{LDA}(\mathbf{r}) = \frac{\delta E_{XC}^{LDA}[n(\mathbf{r})]}{\delta n(\mathbf{r})}, \quad (2.36)$$

In physical terms, the  $V_{XC}^{LDA}$  exhibits a minimal range owing to its local nature. Despite being constructed based on a uniform electron density assumption, it has successfully reproduced experimental observations. Moreover, the LDA adheres to the fundamental principle that one electron is excluded from the immediate vicinity of another electron,

a property known as the exclusion principle. Additionally, the LDA benefits from the advantageous phenomenon of error cancellation. While it typically overestimates correlation energy and underestimates exchange energy, these errors tend to offset each other, resulting in a balanced description of electronic interactions. Although the Local Density Approximation (LDA) disregards corrections to the exchange-correlation (xc) energy stemming from spatial variations, it has enjoyed significant success despite this limitation. Its extensive usage in Density Functional Theory (DFT) over many years has yielded many results documented in the literature. The effectiveness of LDA can be attributed to its adherence to the fundamental sum rule, wherein one electron is excluded from the immediate vicinity of another electron. Moreover, while LDA typically underestimates exchange energy and overestimates correlation energy, these errors often offset each other. However, a recognized drawback of LDA is its tendency to bind molecules<sup>62</sup> excessively.

### Generalized gradient approximation

A semi-local approximation considering gradient dependencies is frequently employed to depict non-uniformities in electron density comprehensively. The Generalized Gradient Approximation (GGA) operates based on gradual density fluctuations surrounding electron coordinates. Typically, the GGA exchange functional is expressed in the following manner<sup>38</sup>,

$$E_X^{GGA} = \int d^3\mathbf{r} n(\mathbf{r}) \epsilon_X^{unif}[n(\mathbf{r})] F_X[s(\mathbf{r})] d^3\mathbf{r}, \quad (2.37)$$

where  $\epsilon_X^{unif}$  is the exchange energy density of a uniform HEG, which is equal to  $-3e^2 k_f / 4\pi$  taking  $k_f = (3\pi^2 n)^{1/3}$ , and  $s$  is the dimensionless generalized density gradient,

$$s(\mathbf{r}) = \frac{|\nabla n|}{2k_f n}, \quad (2.38)$$

Eq. 2.37 is a non-polarized derivation of the GGA approximation; however, it is required to use a spin-polarized calculation that may be found<sup>63</sup>. The augmentation in any GGA model that reinstates the HEG limit is:

$$F_X[s(\mathbf{r})] = 1 + \nu s^2 + \dots (s \rightarrow 0) \quad (2.39)$$

Likewise, the expansion in gradients for the correlation functional that recovers HEG limit:

$$E_C^{GGA}[n(\mathbf{r})] = \int n(\mathbf{r}) \Lambda[n(\mathbf{r})] d^3\mathbf{r}, \quad (2.40)$$

with  $\Lambda[n(\mathbf{r})] = \epsilon_C^{unif}[n(\mathbf{r})] + \frac{\pi k_f}{2} \beta s^2[n(\mathbf{r})] + \dots$  where  $\beta$  is a coefficient. GGA is typically tuned by fitting experimental data, limiting their applicability to specific systems. However, modern parameter-free functionals can be employed across various systems. An example of such functionals is the one devised by Perdew, Burke, and Ernzerhof (PBE)<sup>38</sup>.

### Perdew-Burke-Ernzerhof (PBE)

The constants utilized in the PBE functional are intrinsic parameters,

$$\nu = 0.21951 \text{ and } \beta = 0.0066725, \quad (2.41)$$

Applying the PBE functional in this thesis incorporates essential features such as the linear response of the uniform gas, consistent behavior under uniform scaling, and a smoother potential. Further insights into the theoretical underpinnings of PBE and its implications for practical computations can be explored<sup>64,65</sup>.

### Perdew-Burke-Ernzerhof (PBE) for solids

The Perdew-Burke-Ernzerhof functional for solids (PBEsol) is an upgrade to the PBE-GGA functional. It targets explicitly dense solids and their surfaces by incorporating additional information about their equilibrium properties, primarily focusing on improving the accuracy of lattice constant calculations compared to PBE. This is achieved by adjusting the critical parameters within the PBE functional as follows:

$$\nu = \nu_{GE} = 0.1235, \text{ and } \beta = 0.046, \quad (2.42)$$

where  $\nu_{GE}$  provides a more accurate gradient expansion for slowly varying electronic densities. This functional reduces the dependence on error cancellation by providing accurate xc energies of surfaces<sup>66</sup>.

### Semi-empirical method PBE-D3

The Perdew-Burke-Ernzerhof (PBE) functional is one of the most used functionals in the Density Functional Theory (DFT) method for calculating materials' electronic structure and properties. However, traditional DFT functionals like PBE often struggle to accurately describe dispersion forces we call van der Waals (vdW) interactions, which play a crucial role in many molecular and condensed matter systems<sup>38</sup>.

To address this limitation, Grimme proposed the PBE-D3 functional, which extends PBE by incorporating dispersion corrections<sup>67</sup>. These corrections account for the long-range correlation effects arising from electron density fluctuations, improving the ability of PBE-D3 to describe non-bonded interactions. This makes it particularly valuable for systems where dispersion interactions are significant, such as:

- Molecular complexes
- Adsorption on surfaces
- Intermolecular interactions in solids

The PBE-D3 approach has gained significant popularity in computational chemistry and materials science due to its balanced trade-off between computational efficiency and accuracy<sup>39,68</sup>. Additionally, various versions of PBE-D3 exist, allowing users to tailor the method to their specific needs by adjusting the employed parameters and corrections<sup>67</sup>. The dispersion correction terms added to the PBE functional in PBE-D3 can be represented by equations such as:

$$E_{\text{disp}} = - \sum_{i=1}^N \sum_{j>i}^N f(r_{ij}) \frac{C_{ij}^6}{r_{ij}^6} g(r_{ij}), \quad (2.43)$$

where  $E_{\text{disp}}$  is the dispersion energy,  $N$  is the total number of atom pairs,  $r_{ij}$  is the distance between atoms  $i$  and  $j$ ,  $C_6^{ij}$  is the dispersion coefficient,  $f(r_{ij})$  is a damping function, and  $g(r_{ij})$  is a geometric mean damping function.

Another important equation in PBE-D3 is the total energy expression, which combines the PBE exchange-correlation energy with the dispersion correction:

$$E_{\text{total}} = E_{\text{PBE}} + E_{\text{disp}}, \quad (2.44)$$

where  $E_{\text{PBE}}$  is the total energy calculated using the PBE functional.

### 2.1.9 Derivative Discontinuity

The derivative discontinuity delves into extending energy functionals to accommodate fractional particle numbers, offering insights beyond the conventional treatment restricted to integer values. In exploring the derivation outlined by Engel, E<sup>56</sup>, we uncover a statistical superposition approach, where energy functionals are constructed by amalgamating the lowest energies of two distinct states. This novel perspective allows for a deeper understanding of the underlying principles governing systems with fractional particle numbers, paving the way for enhanced interpretations and applications in density functional theory. Energy functionals are defined only for an integer number of electrons,  $N$ . As Engel, E. stated<sup>56</sup>, the energy functional for fractional particle numbers is derived as the statistical superposition of the lowest energies of the two states:

$$E_f[n(\mathbf{r})] \equiv F_f[n(\mathbf{r})] + \int d^3\mathbf{r} V_{\text{ext}}(\mathbf{r})n(\mathbf{r}), \quad (2.45)$$

where

$$F_f[n(\mathbf{r})] \equiv \min_{\psi_N, \psi_{N+1}} \left( (1 - \eta) \langle \psi_N | \hat{T}_e + V_{e-e} | \psi_N \rangle + \eta \langle \psi_{N+1} | \hat{T}_e + V_{e-e} | \psi_{N+1} \rangle \right), \quad (2.46)$$

with  $0 < \eta < 1$ , and the search for the minimum is restricted by the density

$$n(\mathbf{r}) = (1 - \eta) \langle \psi_N | \hat{n}(\mathbf{r}) | \psi_N \rangle + \eta \langle \psi_{N+1} | \hat{n}(\mathbf{r}) | \psi_{N+1} \rangle, \quad (2.47)$$

For fractional particle numbers, the variational equation that determines the ground state density is well-defined because  $F_f[n(\mathbf{r})]$  exists for any density that integrates up to  $N + \eta$ ,

$$\frac{\delta E_f[n(\mathbf{r})]}{\delta n(\mathbf{r})} = \mu_L, \quad (2.48)$$

where  $\mu_L$  is the Levy-Lieb functional, identical to the chemical potential for integer particle number

$$\mu(N) = \frac{\partial E}{\partial N}(N), \quad (2.49)$$

where the total energy  $E(N + \eta)$  corresponds to the minimum of the energy functional of a fractional particle number,

$$E(N + \eta) = \min_n E_f[n(\mathbf{r})], \quad (2.50)$$

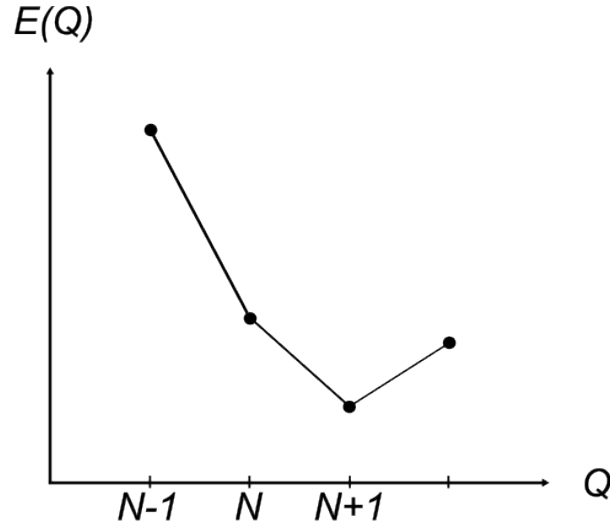


Figure 2.3: Total energy  $E(Q)$  in as a function of the fractional particle number  $Q$  adapted from Ref. 69

The minimum described in Eq. 2.50 occurs when the density  $n(\mathbf{r})$  is a combination of the ground state densities of the  $N$ -particle system  $n_N(\mathbf{r})$  and the  $(N + 1)$ -particle system  $n_{N+1}(\mathbf{r})$ , given by

$$n(r) = (1 - \eta)n_N(\mathbf{r}) + \eta n_{N+1}(\mathbf{r}). \quad (2.51)$$

Similarly, the total energy of a system with  $N + \eta$  particles is a combination of the total energies of systems with  $N$  and  $N + 1$  particles, respectively, yielding

$$E(N + \eta) = (1 - \eta)E(N) + \eta E(N + 1). \quad (2.52)$$

Fig. 2.3 illustrates that the total energy for a fractional number of particles follows a linear function between two integer particle numbers. The chemical potential corresponds to the piecewise linear  $E(Q)$  slope. Consequently, the ionization potential (IP) and the electron affinity (EA) can be expressed simply as

$$\mu(N - \eta) = E_N - E_{N-1} = -IP, \quad (2.53)$$

$$\mu(N + \eta) = E_{N+1} - E_N = -EA. \quad (2.54)$$

Due to the structure of the total energy, the chemical potential  $\mu(N)$ , which represents the energy derivative concerning the number of particles, exhibits discontinuities at all integer particle numbers. Eq. 2.49 implies that the functional derivative of the total energy functional  $E_f[n(\mathbf{r})]$  also contains discontinuities for integer particle numbers, known as derivative discontinuities.

### 2.1.10 Band Gap

The band gap  $E_{gap}$  represents the energy difference between a material's highest occupied (valence) band or valence band maximum (VBM), and lowest unoccupied (conduction) or conduction band minimum (CBM). This property significantly influences various electronic and optical behaviors. Within this framework  $E_{gap}$

$$E_{gap} = E_{CBM} - E_{VBM}, \quad (2.55)$$

Here,  $E_{gap}$  represents the band gap energy, expressed as the difference within the energies of CBM and VBM, respectively<sup>70</sup>, also:  $E_{CBM} = E_{N+1} - E_N$ , and  $E_{VBM} = E_N - E_{N-1}$ ; therefore, for a KS system, the ionization energies can be seen as the orbital energies, so it is possible to define a band gap for a non-interacting system

$$\Delta_{KS} = \varepsilon_{N+1} - \varepsilon_N. \quad (2.56)$$

The  $\varepsilon$  from Eq. 2.56 are an analogous concept to  $E_{VBM}$  and  $E_{CBM}$ , but for this idealized non-interacting system. However, by using equations 2.53 and 2.54, it is possible to rewrite the fundamental band gap as

$$E_{gap} = IP - EA = \lim_{\eta \rightarrow 0^+} (\mu(N + \eta) - \mu(N - \eta)) \quad (2.57)$$

So, Eq. 2.48 into 2.57

$$E_{gap} = \lim_{\eta \rightarrow 0^+} \left( \left. \frac{\delta E[n(\mathbf{r})]}{\delta n(\mathbf{r})} \right|_{N+\eta} - \left. \frac{\delta E[n(\mathbf{r})]}{\delta n(\mathbf{r})} \right|_{N-\eta} \right) \quad (2.58)$$

This possibility of evaluation lies in assessing it at the density of the  $N + \eta$  particles in their ground state. By breaking down the energy functional, similar to Eq. 2.30, and considering we complementing the band gap definition within a discontinuity correction which can be seen as the abrupt change in energy is due to an absence of possible energy states within a certain range. The definition of the energy gap will not depend on  $E_{ext}$ , and  $E_H$  due to their continuity, so band gap energy becomes

$$\begin{aligned} E_{gap} &= \lim_{\eta \rightarrow 0^+} \left[ \left( \left. \frac{\delta T[n]}{\delta n(\mathbf{r})} \right|_{N+\eta} - \left. \frac{\delta T[n]}{\delta n(\mathbf{r})} \right|_{N-\eta} \right) + \left( \left. \frac{\delta E_{xc}[n]}{\delta n(\mathbf{r})} \right|_{N+\eta} - \left. \frac{\delta E_{xc}[n]}{\delta n(\mathbf{r})} \right|_{N-\eta} \right) \right] \\ &= \Delta_{KS} + \Delta_{XC}, \end{aligned} \quad (2.59)$$

The xc potential  $T$  in the Kohn-Sham (KS) system is unique because its derivative has a sudden jump. Additionally, the band gap - the energy difference between the lowest empty and highest filled KS orbitals - can be understood as two parts:

- The difference between the KS energy levels of those orbitals themselves
- The contribution from this jump in the derivative of the xc potential

Then, it can be also written as

$$E_{gap} = \varepsilon_{N+1} - \varepsilon_N + \Delta_{XC}. \quad (2.60)$$



### 2.1.11 GLLB-SC to Describe Band Gaps

From Eq. 2.61, the energy of the band gap is made by two contributions, one of the KS energy levels and the second contribution. by the xc potential from the  $\hat{H}_{KS}$ <sup>71</sup>; therefore it is possible to obtain a better defined  $V_{XC}$ .

#### GLLB-SC xc potential

Based on PBE<sup>61</sup> the correction made by Gritsenko, van Leeuwen, van Lenthe, and Baerends (GLLB) to the xc potential<sup>72,73</sup>. GLLB-SC corresponds to the GLLB xc potential with a solid correction similar to PBEsol from section 2.1.8, so this xc potential can be defined as

$$V_{GLLB-SC}(\mathbf{r}) = 2E_{XC}^{PBEsol}(\mathbf{r}) + \sum_i^{occ} K_X \sqrt{\epsilon_r - \epsilon_i} \frac{|\psi_i(\mathbf{r})|^2}{n(\mathbf{r})} + V_{resp}^{PBEsol}(\mathbf{r}) \quad (2.61)$$

The GLLB-SC potential formulation from Eq. 2.61 is orbital-dependent<sup>74</sup> and this potential add the PBEsol to the GLLB potential formulation creating this correlation<sup>66</sup>.

#### Derivative Discontinuity

The derivative discontinuity, which offers practical assessments of the band gap<sup>75</sup> making possible to predict the band gap of semiconductor materials with higher accuracy due to GLLB-SC<sup>74</sup> its reliability lies on its quasi-particle band gap, which also makes perfect this DFT calculation to perform spectroscopy

$$\Delta_x^{GLLB-SC} = \langle \psi_{CBM} | \sum_{n=1}^{N/2} \frac{8\sqrt{2}}{3\pi^2} (\sqrt{E_{CBM} - E_n} - \sqrt{E_{VBM} - E_n}) \frac{|\psi_n(\mathbf{r})|^2}{n(\mathbf{r})} | \psi_{CBM} \rangle, \quad (2.62)$$

The potential undergoes a sudden change as soon as the CBM wavefunction, denoted as  $\psi_{CBM}$ , begins to be occupied by a tiny increment denoted as  $\eta$ . Here,  $\psi_n$  represents the  $n^{th}$  KS wavefunction, while  $E_{CBM}$ ,  $E_{VBM}$ , and  $E_n$  denote the eigenenergies of the CBM, VBM, and the  $n$ th states, respectively.

## 2.2 Representations of the KS wavefunctions

In density functional theory (DFT) calculations, Kohn-Sham (KS) wavefunctions are usually represented in one of three ways: real-space (RS), plane waves (PW), or linear combinations of atomic orbitals (LCAO). Real-space representations involve sampling wavefunctions at specific grid points, while PW or LCAO representations involve expanding wavefunctions using a basis set of plane waves or atomic orbitals, respectively.

Since wavefunctions belong to a Hilbert space, a vector space endowed with an inner product, they can be expressed as linear combinations of basis vectors. Hence, any state  $\psi$  can be represented as a sum over basis vectors  $\{\phi_\mu\}$  with corresponding expansion coefficients  $c_{n,\mu}$

$$\psi_n = \sum_{\mu} c_{n,\mu} \phi_{\mu} \quad (2.63)$$

In practical implementations, a truncated basis set is often employed to expand wavefunctions, facilitating the solution of the KS equation via a finite matrix approach to solve the eigenvalue problem. This section provides a concise overview of each representation method.

### 2.2.1 Real-Space (RS)

Wavefunctions, electron densities, and potentials can be effectively represented using discrete grids of points in real space<sup>76</sup>.

This approach allows for the straightforward implementation of the finite difference (FD) method to approximate the kinetic energy operator within the Hamiltonian, which involves derivatives. For improved accuracy, increasing the number of grid points, which reduces the grid spacing, becomes crucial. Additionally, real-space representations offer flexibility in imposing various boundary conditions, allowing for periodic, non-periodic, or even hybrid configurations<sup>77</sup>. Moreover, calculations in real space can be efficiently parallelized across different processors through domain decomposition techniques. However, scaling up real-space or FD methods for large molecules with numerous atoms remains challenging due to inherent computational limitations. As it performs a real space calculation, it can be defined as a tensor by Riemann notation<sup>78</sup>. In addition, DF or RS approach involves discretizing the Kohn-Sham equations without assuming any periodicity in the solution.<sup>79</sup>

$$\psi(\mathbf{x}(\xi)) = \sum_{\mathbf{k}} c_{\mathbf{k}} \chi_{\mathbf{k}}(\mathbf{x}(\xi)), \quad (2.64)$$

Where analogously to Eq. 2.63,  $\mathbf{x}(\xi)$  describe the generalized coordinates mapping, and  $\chi_{\mathbf{k}}(\mathbf{x})$  a function which represents the solution to the Schrödinger equation with a combination of the expansion coefficients  $c_{\mathbf{k}}$ . These last two are the variational parameters.

### 2.2.2 Plane Waves (PW)

For periodic systems Bloch's theorem 2.11, and as an application it is possible to express these wavefunctions in to a plane waves PW representation. However, all plane waves are not in the same distances from the nuclei; therefore the Schrödinger equation is not a single PW solutions, instead, a linear combination of PWs. So, using the KS representation from Eq. 2.63 to a given unit cell volume  $\Omega$  the PW general expression is:

$$\psi_{\mathbf{k}}(\mathbf{r}) = \frac{e^{i\mathbf{k}\cdot\mathbf{r}}}{\sqrt{\Omega}} \sum_{\mathbf{G}=0}^{\infty} C_{\mathbf{k}}(\mathbf{G}) e^{i\mathbf{G}\cdot\mathbf{r}}, \quad (2.65)$$

Hence, as the PW basis functions are defined as:

$$\phi_{\mathbf{G}}(\mathbf{r}) = \frac{1}{\sqrt{\Omega}} e^{i\mathbf{G}\cdot\mathbf{r}}, \quad (2.66)$$

Although, it is possible to re-write Eq. 2.66 to a more general solution dependent on a particular point Brillouin zone:

$$\phi_{\mathbf{G}}^{\mathbf{k}}(\mathbf{r}) = \frac{1}{\sqrt{\Omega}} e^{i(\mathbf{k}+\mathbf{G})\cdot\mathbf{r}}, \quad (2.67)$$

So, by using Eq. 2.67, Eq. 2.65 becomes:

$$\psi_j^{\mathbf{k}}(\mathbf{r}) = \sum_{\mathbf{G}=0}^{\infty} C_{j\mathbf{k}}(\mathbf{G})\phi_{\mathbf{G}}^{\mathbf{k}}(\mathbf{r}), \quad (2.68)$$

Where  $j$  corresponds to different eigenstates.

### Energy cutoff

Theoretically, it exists an infinite set of the reciprocal lattice vector to reproduce the wave function solution with an infinite accuracy with an endless set of Fourier coefficient  $C_{\mathbf{k}}(\mathbf{G})$ . However, in a practical situation, those coefficients decrease as  $|\mathbf{k} + \mathbf{G}|$  increases, so it is truncated to a limited number of terms within an Energy cutoff ( $E_{cutoff}$ ) as follows:

$$\frac{1}{2}|\mathbf{k} + \mathbf{G}|^2 < E_{cutoff}. \quad (2.69)$$

### 2.2.3 Atomic Orbitals

Since atomic distributions significantly influence molecular electronic distribution, a logical approach is to refine basis functions to mimic atomic orbitals, which can then be applied to molecular systems or condensed phases. This approach, known as a linear combination of atomic orbitals (LCAO), begins with solving the atomic problem to determine the one-electron eigenstates within an effective central field resembling Coulomb-like interactions. In spherical coordinates, the one-electron Schrödinger-like equation is the starting point for this process.

$$\left[ -\frac{\hbar^2}{2m} \left( \frac{1}{r^2} \frac{\delta}{\delta r} \left( r^2 \frac{\delta}{\delta r} \right) - \frac{\hat{L}^2}{r^2} \right) + V_{eff} \right] \phi_{\alpha}(\mathbf{r}) = E_{\alpha} \phi_{\alpha}(\mathbf{r}), \quad (2.70)$$

here  $\hat{L}^2$  is the angular momentum operator<sup>80</sup>. Because the Hamiltonian commutes with both the angular momentum squared operator  $\hat{L}^2$  and the z-component of angular momentum operator  $\hat{L}_Z$  for a central field, the atomic orbitals (AOs) can be separated into a radial component and an angular component<sup>81</sup>.

$$\phi_{nlm}(\mathbf{r}) = \zeta_{nl}(r) \Upsilon_{lm}(\theta, \phi), \quad (2.71)$$

Eq. 2.71 show  $\Upsilon_{lm}(\theta, \phi)$  as a representation of the spherical harmonics, and  $n, l, m$  are the three quantum numbers.

### Basis sets

The most straightforward and effortless basis set is formed by selecting atomic orbitals (AOs) as basis functions, which are solutions derived from the atomic problem. While it's possible to accomplish this at the preferred level of theory for each atom species, maintaining consistency is often more convenient. For a minimal or single- $\zeta$  (SZ), this kind of basis set is really convenient for isolated atoms; however, it does not consider the polarization by the bonds<sup>77</sup>. Similarly, multiple- $\zeta$  sets are created using the split valence technique to generate multiple functions for each occupied valence orbital<sup>82</sup>. For example, double- $\zeta$ . When it does take into account the polarization functions, it becomes single- $\zeta$  plus polarize (SZP) and double- $\zeta$  plus polarize (DZP), improving the description of the orbitals. On this thesis LCAO were implemented as shown in sec. 2.3 with PAW method<sup>83</sup>.

## 2.3 Projector Augmented Wave (PAW) Method

To solve the Kohn-Sham (KS) equations efficiently, various approximations are employed, primarily concerning the behavior of wavefunctions in different regions of actual space, such as near and away from the nucleus. Two standard methods are the pseudopotential and all-electron approaches. The pseudopotential method utilizes the notion that core electrons, being close to the atomic nucleus, are minimally influenced by the chemical environment, ensuring their binding energy remains consistent across different atomic environments. This method replaces the strong Coulomb potential and highly localized core electron states with a smooth pseudopotential, simplifying the computational representation of valence electrons. However, drawbacks include the need for more information about wavefunctions near the nucleus and the complexity of generating accurate pseudopotentials. Conversely, the all-electron methods retain complete wavefunction information, typically employing the frozen core approximation, where core electron orbitals are precalculated and held fixed. One such method, the Augmented-Plane-Wave (APW) approach<sup>84</sup>, divides space into regions: a spherical region around each atom where wavefunctions are expanded using a local basis, and an interstitial region where another basis set, such as plane waves, is utilized. These two bases are interconnected at the boundaries between the regions, providing a comprehensive representation of the wavefunctions. A broader methodology known as the Projector Augmented Wave method (PAW)<sup>85</sup> offers a more encompassing framework, where the APW<sup>84</sup> approach emerges as a specialized instance, and the pseudopotential method serves as a clearly defined approximation<sup>40</sup>. All this is implemented using GPAW<sup>41</sup> code in all the analyses detailed in this thesis. So the all-electron (AE) Kohn-Sham wavefunction:

$$|\psi_{KS}\rangle = \hat{\mathcal{T}}|\psi_{pseudo}\rangle, \quad (2.72)$$

where  $\psi_{pseudo}$  is the pseudo-wavefunction. and  $\hat{\mathcal{T}}$  operator is the linear transformation. For an operator  $\hat{O}$ , that:

$$\langle \hat{O} \rangle = \langle \psi_{KS} | \hat{O} | \psi_{KS} \rangle = \langle \psi_{pseudo} | \hat{\mathcal{T}}^\dagger \hat{O} \hat{\mathcal{T}} | \psi_{pseudo} \rangle, \quad (2.73)$$

Then, regarding this new linear transformation space named Pseudo Hilbert space. The linear transformation is given by:

$$\hat{\mathcal{T}} = 1 + \sum_a \sum_i (|\phi_i^a\rangle - |\phi_{i,pseudo}^a\rangle) \langle p_{i,pseudo}^a |, \quad (2.74)$$

Eq. 2.74 takes  $\phi_i^a$  as the atom-centered partial waves, expanding the KS wavefunction, also called AE wavefunction, within the augmentation region,  $\phi_{i,pseudo}^a$  corresponds to the partial waves which expand the pseudo-wavefunction. The pseudo-partial waves align with the corresponding genuine partial waves beyond the augmentation region, seamlessly extending within it. The projector function for each pseudo partial wave is confined within the augmentation region and satisfies the condition  $\langle_{i,pseudo}^a | \phi_{j,pseudo}^a \rangle = \delta_{ij}$  inside the sphere. To render the PAW method feasible in practice, certain approximations are required. These encompass the frozen core approximation, which eliminates the need for projector functions for the core states, and the utilization of a finite number of partial waves and projectors. Finally, the KS wavefunction of Eq. 2.72 with Eq. 2.74 becomes:

$$|\psi_{KS}\rangle = |\psi_{pseudo}\rangle + \sum_a \sum_i (|\phi_i^a\rangle - |\phi_{i,pseudo}^a\rangle) \langle p_{i,pseudo}^a | \psi_{pseudo}\rangle, \quad (2.75)$$

These pseudopotentials are smooth and have high accuracy in describing near-core states.

## 2.4 Time-Dependent Density Functional Theory (TDDFT)

Time-dependent density functional theory (TDDFT) addresses interacting electrons in time-varying external potentials, resulting in time-dependent Kohn-Sham (TDKS) equations for fictitious non-interacting electrons. This approach enables the treatment of atoms and molecules subjected to intense laser fields. Additionally, many quantum chemistry codes now compute the response to weak external fields, providing precise estimations of electronic transition frequencies, oscillator strengths, and polarizabilities<sup>86</sup>. Similar to the phenomena of transport and conduction in the quantum realm<sup>87</sup>. This section will elucidate the fundamental concepts underlying TDDFT, namely the Runge-Gross theorem and linear response within TDDFT<sup>88</sup>.

### 2.4.1 Runge-Gross

The Runge-Gross theorem is like the Hohenberg-Kohn theorem, but for systems that change over time. It connects the evolving "density" of a system (how particles are distributed in space) to its changing state. This means you can understand how a system evolves over time by just knowing its density and initial state, without needing to know the exact details of its wavefunction which is governed by the time-dependent Schrödinger equation

$$\hat{H}(t)\psi(t) = i\frac{\delta\psi(t)}{\delta t}, \quad (2.76)$$

where must be set an initial state such as initial condition:

$$\psi(t_0) = \psi_0 \quad (2.77)$$

So, the Hamiltonian will be defined with an external potential changing in time as:

$$\hat{H}(t) = \hat{T} + \hat{V}_{ext}(t) + \hat{W}. \quad (2.78)$$

Considering a system with  $N$  electrons that don't move at speeds close to the speed of light (nonrelativistic). These electrons repel each other Coulomb repulsion and are also influenced by an external force that changes over time (time-dependent external potential)

$$\hat{T} = -\frac{1}{2} \sum_{i=1}^N \Delta_i^2, \quad (2.79)$$

Where  $i$  denotes the coordinates of each particle that is denoted as  $\mathbf{r}_i$ , the particle-particle repulsion is:

$$\hat{W} = \frac{1}{2} \sum_{i \neq j}^N \frac{1}{|\mathbf{r}_i - \mathbf{r}_j|}, \quad (2.80)$$

The summation goes over every combination of two electrons in the system. We divide by 2 to avoid counting the interaction between each electron twice (since electron A interacting with electron B is the same as electron B interacting with electron A). Finally, we represent the force acting on each electron by the term  $V_{ext}(t)$ . The external environment influences this force and may change over time (denoted by  $t$ ).

$$\hat{V}_{ext} = \sum_{i=1}^N V_{ext}(\mathbf{r}_i, t), \quad (2.81)$$

Over time, the way the electrons are distributed in the system changes. This distribution, called the one-particle density, is described by the following equation:

$$n(\mathbf{r}, t) = N \int d^3 r_2 \dots \int d^3 r_N |\psi(\mathbf{r}, \mathbf{r}_2, \mathbf{r}_3, \dots, \mathbf{r}_N, t)|^2, \quad (2.82)$$

The Eq. 2.82 tells the probability of finding any electron within a tiny volume ( $d^3 r$ ) around a specific point  $\mathbf{r}$  at a particular time ( $t$ ). This value, called the electron density, is calculated for every point in space and time. Notably, the total probability of finding all electrons equals the number of electrons ( $N$ ) in the system.

$$\int d^3 r n(\mathbf{r}, t) = N. \quad (2.83)$$

**Theorem 4. Runge-Gross theorem:** states that a system with a defined  $\psi_0$  with two densities  $n(\mathbf{r}, t)$ , and  $n'(\mathbf{r}, t)$  that evolved from that initial state. Both systems are then subjected to external, time-varying forces (potentials) represented by  $V_{ext}(\mathbf{r}, t)$  and  $V'_{ext}(\mathbf{r}, t)$  respectively. We can express these potentials as expansions around a specific time point,  $t_0$ .<sup>88</sup> Must differ eventually if the difference between the potentials  $V_{ext}(\mathbf{r}, t) - V'_{ext}(\mathbf{r}, t)$  goes beyond just a simple factor that changes with time  $c(t)$  or in other words  $V_{ext}(\mathbf{r}, t) - V'_{ext}(\mathbf{r}, t) \neq c(t)$ <sup>89</sup>.

In contrast to working with constant forces in Density Functional Theory (DFT), calculating the total energy in time-dependent DFT is more complicated. This is because the total energy constantly changes rather than remaining constant. Solving the complete equations for time-dependent DFT can be computationally intensive.

## 2.4.2 Time-Dependent KS equations

Analogously as Time-dependent Schrödinger from Eq. 2.76. Let's define the KS time-dependent as

$$i \frac{\delta}{\delta t} \psi_{KS}(\mathbf{r}, t) = \hat{H}_{KS}(t) \psi_{KS}(\mathbf{r}, t), \quad (2.84)$$

To tackle this problem, let's define the density matrix because the approach is more efficient<sup>90,35</sup>. Therefore, the KS density matrix:

$$\rho(t) = \sum_i |\psi_{KS}(t)\rangle f_i \langle \psi_{KS}(t)|, \quad (2.85)$$

Where  $f_i$  represents a factor of occupation of a certain  $n$ th KS state<sup>91</sup>. Considering a time-dependent perturbation theory principles<sup>81</sup>, the time-dependent potential can be written as

$$V_{ext}(\mathbf{r}, t) = V_{gs}(\mathbf{r}) + \lambda \Theta(t - t_0) V_1(\mathbf{r}, t), \quad (2.86)$$

All this approach to solve the first-order perturbation, also the  $\Theta$  denotes the step function also known as Heavyside function, regarding  $\lambda$  between a range of  $[0, 1]$  for weak external perturbations (considering the perturbation turn on when  $(t = t_0)$ ). By following the  $\delta$ -pulse theory perturbation<sup>92</sup>. Is it possible to write a solution to the perturbed KS Hamiltonian in time as<sup>93</sup>

$$\hat{H}_{KS}(t) = \hat{H}_{KS}^{gs} + z K_z \delta(t). \quad (2.87)$$

### 2.4.3 LCAO Time-propagation TDDFT

The LCAO representation is shown in Eq. 2.71, so let's redefine it for a time-dependent pseudo-wavefunction<sup>85</sup> as

$$\Psi_{i,pseudo}(\mathbf{r}, t) = \sum_{\mu} \phi_{\mu,pseudo}(\mathbf{r}) C_{\mu i}(t), \quad (2.88)$$

where  $i$  denotes the  $i$ -th wavefunction state, and  $C_{\mu i}$  are the coefficients of the expansion. To attack the computational problem, the PAW method is shown in Eq. 2.74 from Ref. 86. Then, the LCAO wavefunction written with the PAW formalism<sup>94</sup>

$$\left[ \hat{\mathcal{T}}^{\dagger} \left( -i \frac{d}{dt} + \hat{H}_{KS}(t) \right) \hat{\mathcal{T}} \right] \Psi_{i,pseudo}(\mathbf{r}, t) = 0. \quad (2.89)$$

Then let's use Eq. 2.88 into Eq. 2.89, and multiplying on the left by  $\int d\mathbf{r} \phi_{\mu,pseudo}(\mathbf{r})$ <sup>95</sup>

$$\langle \phi_{\mu,pseudo} | \hat{\mathcal{T}}^{\dagger} \hat{\mathcal{T}} | \phi_{\nu,pseudo} \rangle i \frac{d\mathbf{C}(t)}{dt} = \langle \phi_{\mu,pseudo} | \hat{\mathcal{T}}^{\dagger} \hat{H}_{KS}(t) \hat{\mathcal{T}} | \phi_{\nu,pseudo} \rangle \quad (2.90)$$

$\mathbf{C}(t)$  is the matrix of the all  $C_{\mu i}(t)$  on Eq. 2.90. However, to solve it numerically, we must use matrix expression taking  $\mu, \nu$  as sub-indexes as:

$$i\mathbf{S} \frac{d\mathbf{C}(t)}{dt} = \mathbf{H}(t)\mathbf{C}(t), \quad (2.91)$$

Where all these three matrices are the dense matrices that are implemented by using ScaLAPACK<sup>96</sup>. Presently, a semi-implicit Crank–Nicolson method (SICN)<sup>97</sup> is employed to advance wave functions. To progress the wave functions at a specific time  $t$ , the system is propelled forward using  $\mathbf{H}(t)$  and addressing the linear equation

$$(\mathbf{S} + i\mathbf{H}(t)dt/2)\mathbf{C}'(t + dt) = (\mathbf{S} - i\mathbf{H}(t)dt/2)\mathbf{C}(t). \quad (2.92)$$

### 2.4.4 Linear density response of the KS system

Due to an external influence, the system's density undergoes small variations over time. This change in density can be expressed in a series of terms:

$$n(\mathbf{r}, t) = n_0(\mathbf{r}) + \lambda n_1(\mathbf{r}, t) + \lambda^2 n_2(\mathbf{r}, t) + \dots \quad (2.93)$$

The passage describes the density response  $n$  of a system to a small perturbation ( $V_1$  and  $\lambda$ )(see Eq. 2.86). It separates the response into linear  $n_1$  and higher-order  $n_2$  terms, emphasizing that the linear term dominates due to the weak perturbation. Norm conservation ensures the total density response integrates to zero. As we look for the first-order solution, let's express the linear response of the density

$$n_1(\mathbf{r}, t) = \int_{-\infty}^{\infty} dt' \int d^3\mathbf{r}' \chi(\mathbf{r}, t, \mathbf{r}', t') V_1(\mathbf{r}', t'), \quad (2.94)$$

on Eq. 2.94  $\chi$  corresponds to the density-density response function given by<sup>89</sup>

$$\chi(\mathbf{r}, t, \mathbf{r}', t') = -i\theta(t - t') \langle \Psi_{gs} | [\hat{n}(\mathbf{r}, t - t'), \hat{n}(\mathbf{r}')] | \Psi_{gs} \rangle \quad (2.95)$$

According to Eq. 2.95, to compute the system's response at a particular point in time and space, we need to take into account its initial state, represented by the ground state wavefunction  $\Psi_{gs}$ . Additionally, thanks to the Hohenberg-Kohn theorem, the equation expresses the response function entirely in terms of the ground state density  $n_0$ , using a mathematical concept called a functional  $\chi[n_0]$ .

### Frequency-dependent response representation

The structure of the density response varies with frequency<sup>89</sup>

$$n_1(\mathbf{r}, \omega) = \int d^3 r' \chi_{nm}(\mathbf{r}, \mathbf{r}', \omega) V_1(\mathbf{r}', \omega), \quad (2.96)$$

where it's Fourier Transform, and  $\Omega_n = E_n - E_{gs}$ , also known as Lehman representation of the density-density response function<sup>89</sup>

$$\chi_{nm}(\mathbf{r}, \mathbf{r}', \omega) = \lim_{\eta \rightarrow 0^+} \sum_{n=1}^{\infty} \left[ \frac{\langle \Psi_{gs} | \hat{n}(\mathbf{r}) | \Psi_n \rangle \langle \Psi_n | \hat{n}(\mathbf{r}') | \Psi_{gs} \rangle}{\omega - \Omega_n + i\eta} - \frac{\langle \Psi_{gs} | \hat{n}(\mathbf{r}') | \Psi_n \rangle \langle \Psi_n | \hat{n}(\mathbf{r}) | \Psi_{gs} \rangle}{\omega + \Omega_n + i\eta} \right]. \quad (2.97)$$

Therefore as a consequence of the theorems of Hohenberg-Kohn (2, 3) and Runge-Gross (4), hence it is possible to define the density as a functional of position and time based on the KS effective potential, and the external potential as:

$$n(\mathbf{r}, t) = n[V_{eff}[V_{ext}]], \quad (2.98)$$

Subsequently, the linear response of density, denoted as  $n_1$ , can be determined using the linearized effective Kohn-Sham (KS) potential as outlined in Equation 2.96. In this context, the response function for density-density interactions within the non-interacting KS system can be represented as stated

$$\chi^0(\mathbf{r}, \mathbf{t}, \mathbf{r}', \mathbf{t}') = \left. \frac{\delta n[V_{eff}](\mathbf{r}, t)}{\delta V_{eff}(\mathbf{r}', t')} \right|_{V_{eff}[n_0](\mathbf{r})} \quad (2.99)$$

Here, the linearized effective Kohn-Sham (KS) potential, specifically the potential of order  $\lambda$ , is referred to

$$V_{eff-\lambda}[n(\mathbf{r}, t)] = V_{ext}(\mathbf{r}, t) + \int d^3 \mathbf{r}' \frac{n_1(\mathbf{r}', t)}{|\mathbf{r} - \mathbf{r}'|} + V_{xc-\lambda}(\mathbf{r}, t), \quad (2.100)$$

In the context of Time-Dependent Density Functional Theory (TDDFT), it is necessary to iteratively compute the linear density response of the non-interacting Kohn-Sham system to an applied perturbation. This is because the linearized effective potential defined in Eq. 2.100 relies on the density response (r,t). The Kohn-Sham system's response function which takes  $\omega_{mn} = E_m - E_n$  as the perturbed state energy or excitation energies, expressed in frequency, is provided

$$\chi^0(\mathbf{r}', \mathbf{r}, \omega) = \lim_{\eta \rightarrow 0^+} \sum_{m,n=1}^{\infty} \frac{f_n - f_m}{\omega - \omega_{mn} + i\eta} \varphi_m(\mathbf{r}) \varphi_n^*(\mathbf{r}) \varphi_m^*(\mathbf{r}') \varphi_n(\mathbf{r}'), \quad (2.101)$$



A Fourier transform concerning position can acquire the linear density response in reciprocal space. This proves beneficial for systems characterized by periodic boundary conditions. As the subsequent equation depicts, the transition is made by employing position vectors  $\mathbf{r}$  and  $\mathbf{r}'$  to utilize reciprocal lattice vectors  $\mathbf{G}$  and  $\mathbf{G}'$ <sup>98</sup>:

$$\chi_{\mathbf{G}\mathbf{G}'}^0(\mathbf{q}, \omega) = \frac{1}{\Omega} \sum_{\mathbf{k}} \sum_{n,m} \frac{f_{n,\mathbf{k}} - f_{m,\mathbf{k}+\mathbf{q}}}{\omega + E_{n,\mathbf{k}} - E_{m,\mathbf{k}+\mathbf{q}} + i\eta} \langle \varphi_{n,\mathbf{k}} | e^{-i(\mathbf{q}+\mathbf{G})\cdot\mathbf{r}} | \varphi_{m,\mathbf{k}+\mathbf{q}} \rangle \langle \varphi_{n,\mathbf{k}+\mathbf{q}} | e^{i(\mathbf{q}+\mathbf{G}')\cdot\mathbf{r}'} | \varphi_{m,\mathbf{k}} \rangle, \quad (2.102)$$

where  $q$  represents the momentum transferred by the perturbation,  $f_{n,\mathbf{k}}$ ,  $E_{n,\mathbf{k}}$ , and  $\varphi_{n,\mathbf{k}}$  stand for the occupations, eigenvalues, and eigenfunctions of the  $n$ th band at the  $\mathbf{k}$ th  $k$ -point in the Brillouin zone (BZ),  $\Omega$  denotes the volume of the unit cell, and  $\eta$  denotes the half-width at half-maximum of the Lorentzian broadening.

### Random Phase Approximation

In linear-response Time-Dependent Density Functional Theory (TDDFT), accurately determining the exchange-correlation (xc) kernel is crucial. This kernel can be approximated using various methods, either derived from approximations to the time-dependent xc potential or constructed directly. The chosen time-dependent xc potential must match the approximate static xc potential utilized to establish the system's initial ground state. The time-dependent xc potential must converge to the static xc potential without external perturbations. These requirements extend to the xc kernel, ensuring consistency with the static xc potential used in the ground-state calculation. Deviations from this consistency can lead to violations of fundamental principles of linear response theory<sup>99</sup>, potentially resulting in inaccuracies in excitation energies and oscillator strengths. The most straightforward and drastic approach to handling the exchange-correlation (xc) kernel, termed the random phase approximation (RPA), involves setting it to zero:

$$f_{xc}^{RPA} = 0. \quad (2.103)$$

### Interacting density response function

The solution to the Dyson equation allows for the retrieval of the density response function under interaction

$$\chi(\mathbf{r}, \mathbf{r}', \omega) = \chi^0(\mathbf{r}, \mathbf{r}', \omega) + \iint_{\Omega} d^3\mathbf{r}_1 d^3\mathbf{r}_2 \chi^0(\mathbf{r}, \mathbf{r}_1, \omega) \left[ \frac{1}{|\mathbf{r}_1 - \mathbf{r}_2 + f_{xc}(\mathbf{r}_1, \mathbf{r}_2, \omega)} \right] \chi(\mathbf{r}_2, \mathbf{r}', \omega), \quad (2.104)$$

All the expressions involved depend on the ground-state density, and it is feasible to estimate the interacting response function using the non-interacting response function:

$$\chi_{\mathbf{G},\mathbf{G}'}(\mathbf{q}, \omega) \approx \frac{\chi_{\mathbf{G},\mathbf{G}'}^0(\mathbf{q}, \omega)}{1 - V_{\mathbf{G},\mathbf{G}'} \chi_{\mathbf{G},\mathbf{G}'}^0(\mathbf{q}, \omega)}, \quad (2.105)$$

Here,  $V_{\mathbf{G},\mathbf{G}'}$  represents the interaction kernel governing the Coulomb interaction in three dimensions as

$$V_{\mathbf{G},\mathbf{G}'}(\mathbf{q}) = \frac{4\pi}{\|\mathbf{q} + \mathbf{G}\|^2}. \quad (2.106)$$

## 2.5 Vibrational Spectroscopy

Vibrational spectroscopy is a powerful analytical technique used to study the way molecules vibrate. This method helps us understand the energy levels of molecules and gives us important information about molecular structures, chemical bonding, and interactions between molecules. This section focuses on two main techniques in vibrational spectroscopy: Raman spectroscopy and infrared (IR) spectroscopy. In this context, the vibrational modes are explored through DFT calculations. This allows us to obtain a system's vibrational characteristics, or eigenmodes, by solving an eigenvalue problem<sup>100</sup>. This problem involves a matrix equation and specific conditions.

$$\sum_{k=1}^{3N} (H_{jk} - \lambda_i M_{jk}) X_{ki} = 0, \quad (2.107)$$

Here:

- $j = 1, \dots, 3N$  (iterates over all  $3N$  degrees of freedom)
- $\lambda_i = (2\pi\nu_i)^2$  (represents the squared frequency ( $\nu_i$ ) of the  $i$ -th mode)
- $X_{ki}$  (elements of the  $i$ -th eigenvector)
- $H$  (dynamical of the Hessian matrix)
- $M$  (mass matrix, diagonal with elements  $m_n$  for the  $n$ -th atoms mass)

Now, following the normalization condition:

$$\sum_{k=1}^{3N} \sum_{l=1}^{3N} X_{ki} M_{kl} X_{lj} = \delta_{ij}, \quad (2.108)$$

Where the  $\delta_{ij}$  represents the Kronecker delta, equal to 1 if  $i = j$  and 0 otherwise. Eq 2.108 takes  $M_{kl} = \delta_{kl} m_n$ ,  $k = 3n - 2, 3n - 1, 3n$ . In addition, the Hessian matrix captures how much the system's total energy changes in response to tiny movements of its atoms.

$$H_{aa'} = \nabla_{\mathbf{r}_{a'}} \otimes \nabla_{\mathbf{r}_a} E = \frac{\delta^2 E}{\delta \mathbf{r}_{a'} \delta \mathbf{r}_a} \quad (2.109)$$

The displacement  $U_{ki}$  in the direction of the  $i$ -th eigenvector can be expressed as

$$U_{ki} = Q_i X_{ki} \quad (2.110)$$

The term  $Q_i$  is denoted as a normal-mode coordinate. Frequently, it becomes necessary to compute the derivatives of a physical property  $A$  concerning  $Q_i$ . If the derivatives of  $A$  are already established concerning the external Cartesian atomic coordinates  $\mathbf{R}_k$ , the desired expression can be readily derived from the existing framework:

$$\frac{dA}{dQ_i} = \sum_{k=1}^{3N} \frac{\partial A}{\partial \mathbf{R}_k} X_{ki} \quad (2.111)$$

### 2.5.1 Infrared

Infrared spectroscopy involves molecules' absorption of infrared radiation, causing vibrational transitions between different energy levels. By measuring the absorption of infrared light at specific wavelengths, IR spectroscopy provides insights into molecular vibrations, including stretching, bending, and twisting motions of chemical bonds. The infrared employs a harmonic approximation, where the vibrational eigenmodes are determined by solving the eigenvalue equation<sup>43</sup>. The first-order infrared intensity of the  $i$ -th mode<sup>101</sup>, is given by:

$$I_i^{IR} = \frac{N\pi}{3c} \left| \frac{d\mu}{dQ_i} \right|^2, \quad (2.112)$$

Eq. 2.112. express  $N$  as the particle density,  $c$  as the velocity of light,  $Q_i$  as the normal-mode coordinate,  $\mu$  the electric dipole moment of the system<sup>43</sup>. The sole molecular property incorporated in the formula,  $\frac{d\mu}{dQ_i}$ , is commonly referred to as the absolute infrared intensity. The components of the Hessian matrix in Eq. 2.109 are computed using finite displacements. Specifically, for each atomic coordinate  $\delta r_a$ , the coordinate is initially increased by a small value,  $\frac{1}{2}\Delta r'_a$ , and the gradients are computed. Then, the coordinate is decreased by  $\Delta r'_a$ , and the gradients are recalculated. The second derivative is subsequently derived from the difference between the two gradients and the step size. Re-written Fourier transform infrared intensity can be written in terms of the eigenvectors, the displacements, and the dipole moment  $\mathbf{d}$  as:

$$I_{k,i}^{FTIR} = \frac{N\pi}{3c} \left| \sum_{a=1}^{N_a} (\mathbf{X}_{k,a} \cdot \nabla_{\mathbf{r}_a} \mathbf{d}) \right|^2, \quad (2.113)$$

As subsequent FTIR intensities only need the Hessian matrix shown in eq. 2.109 and the dipole moment  $\mathbf{d}$ .

### 2.5.2 Resonant Raman (RR)

Raman spectroscopy is based on the inelastic scattering of photons by molecules (electro-phonon interaction<sup>102</sup>), where incident light interacts with molecular vibrations, resulting in energy shifts that are characteristic of the vibrational modes of the molecule<sup>43</sup>. This technique offers detailed information about molecular symmetry, chemical composition, and structural changes, making it invaluable in various fields such as chemistry, materials science, and biology.

The Raman intensities  $I_\lambda^{Raman}$  are derived from the polarizability tensor  $\tilde{\alpha}$  of the molecules and the eigenvectors of the Hessian matrix  $\mathbf{X}_{\lambda,a}$ , utilizing:

$$I_\lambda^{Raman} = C \frac{2\pi^2 N h \nu_S^4}{c^4 \nu_\lambda} \frac{|\hat{\mathbf{e}}_S \sum_{a=1}^{N_a} (\mathbf{X}_{\lambda,a} \cdot \nabla_{\mathbf{r}_a}) \tilde{\alpha} \hat{\mathbf{e}}_q|^2}{1 - \exp\left(-\frac{h\nu_\lambda}{k_B T}\right)} \quad (2.114)$$

Eq. 2.114 depict  $\nu_S$  and  $\hat{\mathbf{e}}_S$  as the frequency and polarization direction of the scattered light, respectively, and  $\hat{\mathbf{e}}_q$  as the polarization direction of the incident light. Unlike the computation of FTIR intensities, determining Raman intensities necessitates separately calculating the derivatives of the polarizability matrix  $\tilde{\alpha}$  for the atomic coordinates  $\mathbf{r}_a$ . This requirement makes the computation of Raman spectra significantly more computationally demanding than that of FTIR spectra, and only feasible for Real-Space (RS) representation of the KS wavefunctions.

## 2.6 Bader Charge Analysis

Throughout history, chemists have observed that some properties of atoms and functional groups seem to hold across different molecules. This has been crucial for creating group additivity models, which predict properties based on these group contributions. However, the exact electronic explanation for why these properties are transferable is still a question<sup>103</sup>. Richard Bader's Quantum Theory of Atoms in Molecules (QTAIM)<sup>104</sup> offers a fresh perspective on how atoms exist within molecules. It redefines atoms based on the electron density, using "zero flux surfaces" - regions where electron density dips - to naturally separate them. This approach proves valuable for analyzing charge distribution within molecules, allowing scientists to calculate features like atomic charge and multipole moments and even quantify bond strength through numerical values.

### 2.6.1 Grid Method

Our research presents a highly efficient and reliable computational method for dividing a charge density grid into individual Bader volumes. This method works by following the steepest slopes of electron density (charge density gradient) point-by-point across the grid until it reaches a peak. Once assigned to a peak, a grid point is no longer considered for other Bader volumes. This clever grid-based approach allows the method to handle the massive datasets generated by plane-wave density functional theory calculations, making it a powerful tool for Bader volume analysis<sup>44,105,106</sup>.

## 2.7 Density of States (DOS)

The Density of States (DOS) provides an insight into the electronic structure. It quantifies the distribution of energy levels (states) available to electrons within a material across its energy spectrum. DOS has great significance in understanding electronic properties such as conductivity, magnetism, and optical behavior. In theoretical spectroscopy DOS can be applied for describing Ultraviolet Photoelectron Spectroscopy (UPS) and Inverse Photoelectron Emission Spectroscopy (IPES), we can describe DOS by mapping the states as follows:

$$\rho(\varepsilon) = \sum_n \langle \psi_n | \psi_n \rangle \delta(\varepsilon - \varepsilon_n), \quad (2.115)$$

In the context of eigenstates, where  $\varepsilon$  is the eigenvalue of the eigenstate  $|\psi_n\rangle$ , this can be rewritten by inserting a complete orthonormal basis.

$$\begin{aligned} \rho(\varepsilon) &= \sum_i \rho_i(\varepsilon), \\ \rho_i(\varepsilon) &= \sum_n \langle \psi_n | i \rangle \langle i | \psi_n \rangle \delta(\varepsilon - \varepsilon_n) \end{aligned} \quad (2.116)$$

where  $\rho_i(\varepsilon)$  represents the projected density of states (PDOS). Thus, summing up the PDOS over  $i$  yields the spectral weight of orbital  $i$ .

### 2.7.1 Molecular Orbital PDOS

As demonstrated in the Density of States section, creating the Projected Density of States (PDOS) involves projecting the Kohn-Sham eigenstates as  $\psi_n$  onto a set of orthogonal states  $\psi_m$ .

$$\rho_m(\varepsilon) = \sum_n |\langle \psi_m | \psi_n \rangle|^2 \delta(\varepsilon - \varepsilon_n) \quad (2.117)$$

The overlaps of all electrons can be computed within the Projector Augmented-Wave (PAW) formalism using the pseudo wave functions, and their projector overlaps<sup>85</sup> by:

$$\langle \psi_m | \psi_n \rangle = \langle \psi_{m,pseudo} | \psi_{n,pseudo} \rangle + \sum_a \sum_{i_1, i_2} \langle \psi_{m,pseudo} | p_{i_1,pseudo}^a \rangle \langle \phi_{i_1}^a | \phi_{i_2}^a \rangle - \langle \phi_{i_1,pseudo} | \phi_{i_2,pseudo} \rangle \langle p_{i_1,pseudo}^a | \psi_{n,pseudo} \rangle, \quad (2.118)$$

However, suppose we choose to project onto the partial waves of all electrons (i.e., the wave functions of the isolated atoms)  $\phi_i^a$ . In that case, we observe directly from the formulation in the Molecular Orbital PDOS section that the pertinent overlaps within the PAW formalism are evident as:

$$\langle \phi_i^a | \psi_n \rangle = \langle \phi_{i,pseudo}^a + \sum_{a'} \sum_{i_1, i_2} \langle \phi_{i,pseudo}^a | p_{i_1,pseudo}^{a'} \rangle \langle \phi_{i_1}^{a'} | \phi_{i_2}^{a'} \rangle - \langle \phi_{i_1,pseudo}^{a'} | \phi_{i_2,pseudo}^{a'} \rangle \langle p_{i_2,pseudo}^{a'} | \psi_{n,pseudo} \rangle \quad (2.119)$$

Thus, we can define PDOS for atomic orbitals within the sphere approximations of the augmentation,

$$\rho_i^a(\varepsilon) = \sum_n |\langle p_{i,pseudo}^a | \psi_{n,pseudo} \rangle|^2 \delta(\varepsilon - \varepsilon_n) \approx \sum_n |\langle \phi_i^a | \psi_n \rangle|^2 \delta(\varepsilon - \varepsilon_n). \quad (2.120)$$

So, in this way, it is possible to obtain the PDOS of a specific atom to a specific orbital such as s,p,f, and f.

## 2.8 UPS

Spectroscopy based on the photoelectric effect to measure their emission of electrons by a photo (photoelectric effect) can produce powerful results about the electronic behavior of gases & solids<sup>107</sup>. Ultraviolet Photoelectron Spectroscopy (UPS) was developed in the 1960s and provides quite interesting results to describe valence electrons, particularly in carbon-based materials<sup>108</sup>. The fundamental principles of the technique, along with the methods for accurately measuring the valence spectra of uncovered metals and metals with adsorbed layers<sup>109</sup>. Self-assembled monolayers (SAMs)<sup>110</sup> being adsorbed on top of a metal mixed with the extreme sensitivity of the UPS<sup>109</sup> for those overlayers is expected to be particularly rewarding<sup>111</sup> to describe the behavior of the valence electrons, i.e., occupied states or electrons below the Fermi level. Fig. 2.8 represents just an illustrative schematic of the UPS experimental process theory explained. However, our UPS analysis was carried out for DOS without considering those secondary electrons as can be seen in Fig.4.5 literal a).

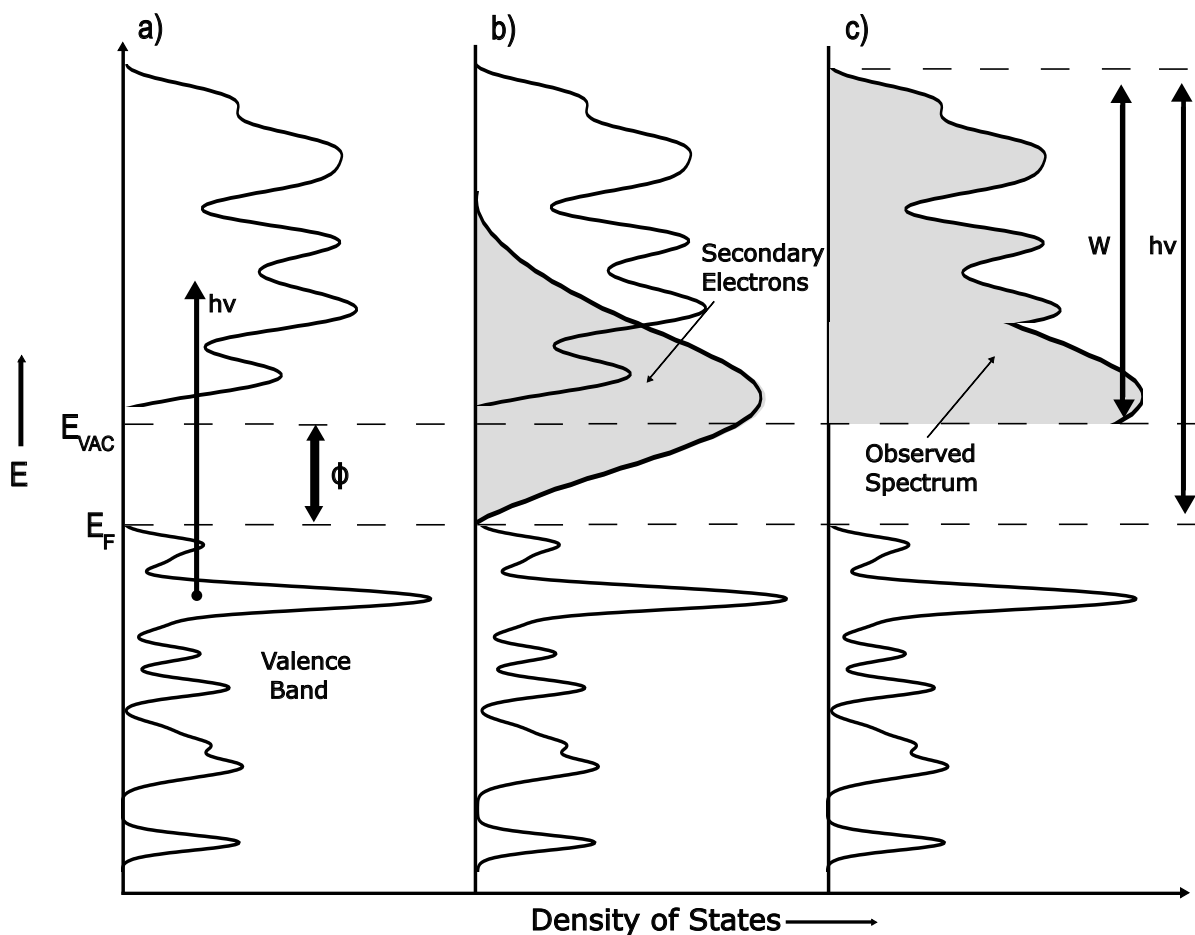


Figure 2.4: Schematic of the UPS process. a) Density of States (in this schematic is metal), b) As these excited electrons travel from below the surface to the surface-vacuum boundary, some lose energy and become **secondary electrons**, c) The observed spectrum consists of photoelectrons that reach the surface without energy loss and secondary electrons above  $E_{vacuum}$ .  $E_F$  represents the Fermi level of the spectrometer. The total of the spectrum's width ( $w$ ) and the work function ( $\phi$ ) equals the photon energy<sup>109</sup>. Adapted from Ref. 109.

## 2.9 Scanning Tunneling Microscopy

The Scanning Tunneling Microscopy (STM) technique was discovered and developed by Binnig and Rohrer at IBM laboratories at Zurich in 1981<sup>10,112</sup>. Today, there are two main types of STM. Both types utilize a sharp metallic conductive tip and apply a voltage known as a bias voltage, with a resulting tunneling current in the picoampere

range, allowing surface mapping with incredibly high resolution, sometimes reaching 1 angstrom. One type of STM uses a piezoelectric material to move the tip over the surface while maintaining a constant bias voltage. The other type keeps the tip fixed and varies the bias voltage during scanning<sup>113,114</sup>. STM is a key tool in surface science. It allows us to see and manipulate individual atoms and molecules on surfaces with incredible precision. In this thesis, we used STM measurements with the first type of STM mentioned (constant voltage bias).

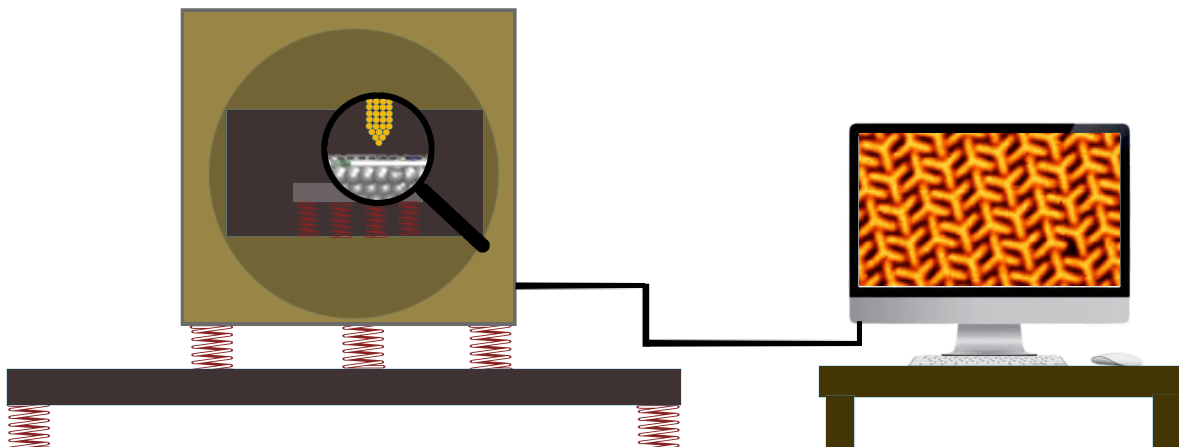


Figure 2.5: Schematic representation of STM in a nutshell adapted from 113. The scanning waveforms applied to the x and y piezos cause the tip to raster scan across the sample surface. A bias voltage is applied between the sample and the tip to induce a tunneling current. A feedback system controls the z piezo to keep the tunneling current constant. The voltage on the z piezo indicates the local topography height. To ensure stable operation, vibration isolation is really crucial<sup>113</sup> in order to get the best imaging possible.

For theoretical STM simulations on this thesis, the Tersoff-Hamann<sup>115</sup> model was applied with its equation implemented by the projected wave method<sup>40</sup> on GPAW<sup>41,116</sup>. The Tersoff-Hamann equation represents the tunneling effect of the current based on the local density of states (LDOS) by the wavefunction as follows:

$$\int_{E_F}^{E_F+eV} \sum_{k_n} w_k |\Psi_{k_n}(\mathbf{r})|^2 \delta(\varepsilon - \varepsilon_{k_n}) d\varepsilon, \quad (2.121)$$

where  $V$  represents the bias voltage of the tip,  $w_k$  denotes the  $k$ -point weight, and  $\Psi_{k_n}(\mathbf{r})$  is the wave function.

## 2.10 1,3,4-tris[4-(pyridine-4-yl)- [1,1'-biphenyl]]benzene (TPyPPB)

In this thesis, our exploration delves into the intricate realm of molecular self-assembly, mainly focusing on the spontaneous organization of a distinctive organic molecule known as 1,3,4-tris[4-(pyridine-4-yl)-[1,1'-biphenyl]]benzene

(TPyPPB) on an Ag(111) surface. This intriguing molecule boasts a unique three-legged structure featuring phenyl spacers adorned with pyridyl end groups<sup>29</sup>. The study conducted by Ceccatto et al.<sup>29</sup> provides valuable insights into the self-assembly behavior of TPyPPB, unveiling a diverse array of potential structures that emerge upon deposition on metallic substrates, such as the face-centered cubic (Fcc)(111) crystal of copper. A pivotal aspect of this investiga-

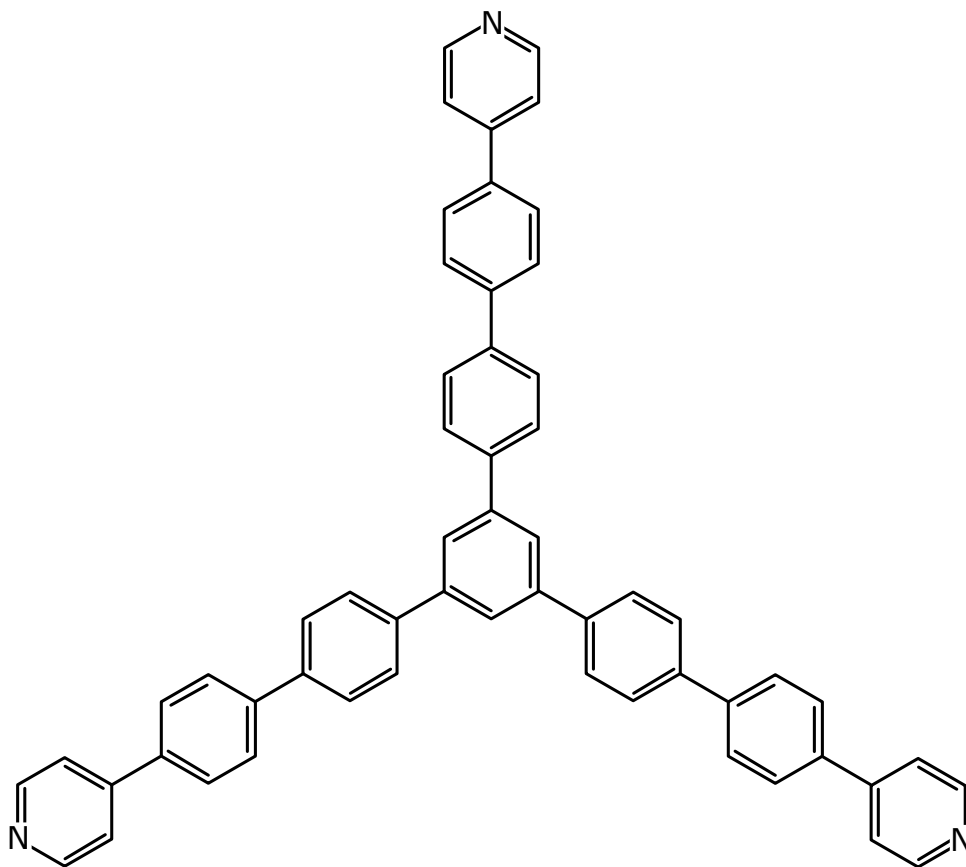


Figure 2.6: 1,3,4-tris[4-(pyridine-4-yl)-[1,1'-biphenyl]]benzene

tion lies in the characterization of TPyPPB's self-assembly on Cu(111) across a spectrum of temperatures, revealing a rich tapestry of structural motifs ranging from vitreous arrangements to meticulously ordered honeycomb nanostructures<sup>29</sup>. Through the lens of density functional theory (DFT) augmented with dispersion corrections (DFT-D3), Ceccatto et al.<sup>29</sup> elucidate the underlying mechanisms driving these diverse assemblies, shedding light on the role of Cu adatoms in facilitating pyridyl-copper-pyridyl (Py-Cu-Py) bonding modes. This comprehensive exploration underscores the profound influence of substrate interactions and environmental conditions on the self-assembly dynamics of TPyPPB, paving the way for a deeper understanding of molecular organization at the nanoscale. During



this thesis, we studied the behavior of TPyPPB and based on Ceccato et al.<sup>29</sup>, we can see how the symmetry of the emerging self-assembled structures. Given the unique nature of tecton-substrate complexes and their distinct mobility and interaction dynamics outlined earlier, it becomes evident that a distinct chemical arena emerges for non-covalent synthesis on surfaces. Consequently, traditional rules and experiences garnered from solution or solid-state environments cannot be readily applied. Surfaces present unparalleled platforms where novel 2D supramolecular chemistry must be investigated. Furthermore, the energetics, distances, and geometric alignment of hydrogen bonds at metal surfaces may differ from those observed in three-dimensional environments<sup>16</sup>. Additionally, electrostatic interactions can be notably affected by screening effects<sup>16</sup>. Especially valuable are tectons with planar-extended  $\pi$ -systems and functional groups at the periphery as TPyPPB. When placed on suitable substrates such as Ceccato et al.<sup>29</sup> on Cu(111) or this thesis on Ag(111), these tectons adhere in flat orientations, promoting lateral molecular recognition<sup>16</sup>.

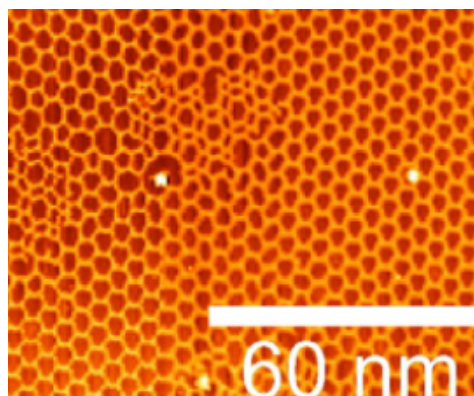


Figure 2.7: Highly ordered nanoporous of TPyPPB on Cu(111) getting honeycomb packing by thermal treatment adapted from Ceccato et al. previous work in Ref. 29.

During heat treatments ranging from 350 to 420 K, the honeycomb nanostructure emerges as the predominant phase owing to its stability. However, the degree of surface coverage by this phase is contingent upon the initial deposition amount. Insufficient molecular presence may impede the formation of this phase, whereas an excess of molecules could curtail molecular diffusion, thereby influencing the extent of coverage. Therefore, growing a highly ordered structure is feasible as we increase the annealing time and varying temperature. For example, Ceccato et al. grew large domain (> 125nm) structures.

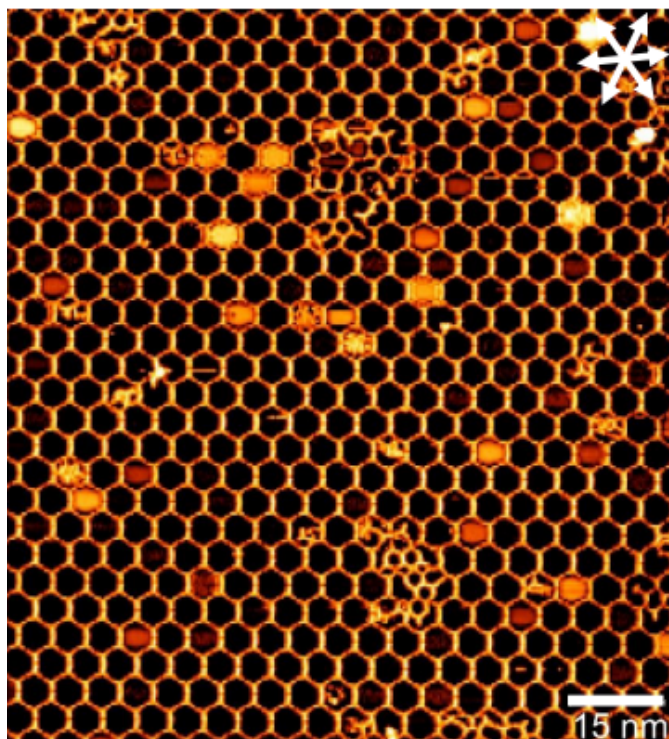


Figure 2.8: A long-range ordered network with a hexagonal structure (honeycomb) is treated with a deposition of TPyPPB<sup>29</sup> at 400K adapted from Ref 29.

Fig. 2.8 depicts a nanoporous network, demonstrating TPyPPB's ability to form highly ordered structures in space. This property suggests TPyPPB's suitability for practical applications.

### 2.10.1 TPyPPB on Ag(111)

The primary structures investigated in this thesis comprise two nanoporous formations (two packings triangular and inverted), specifically the self-assembled configurations of TPyPPB on Ag(111) as Ceccatto et al<sup>117</sup> work. This analysis is grounded in the subsequent scanning tunneling microscopy (STM) image which established our initial structure guess.

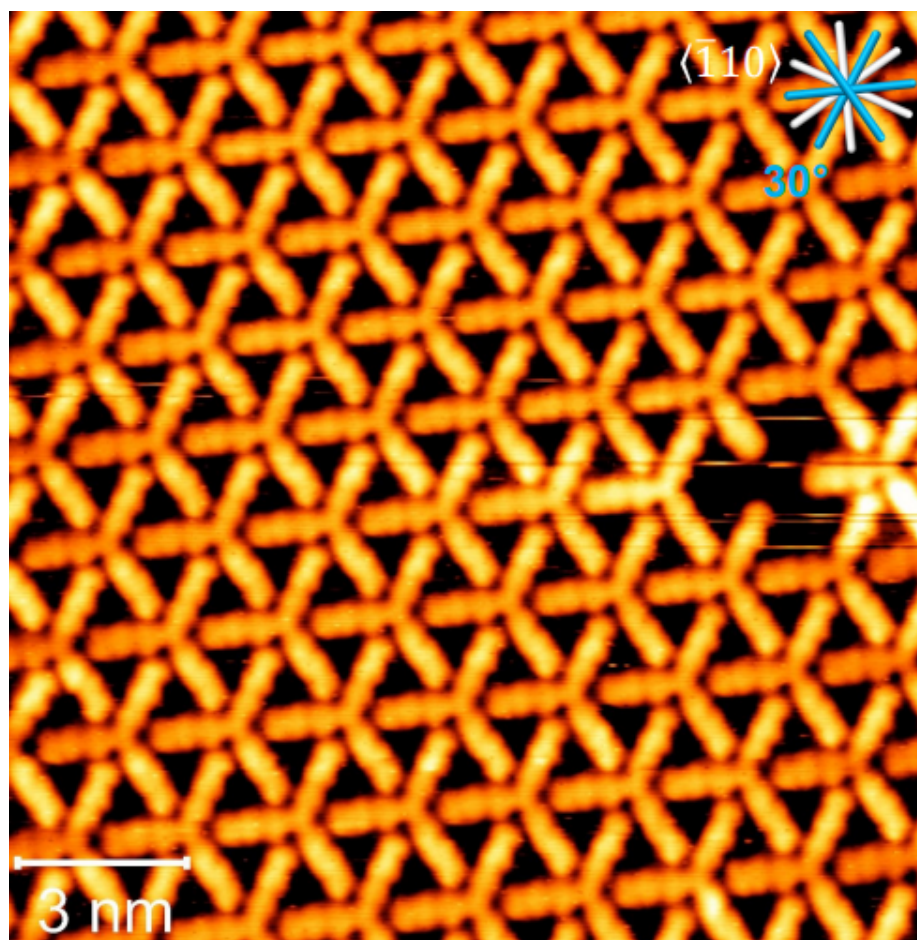


Figure 2.9: The high-ordered self-assembled nanoporous network of TPYPPB on Ag(111) shows the molecule's direction concerning the main crystallographic directions adapted from Ceccato et al<sup>117</sup>.

Fig. 2.9 illustrates a rotation of the structure's legs by 30 degrees relative to the primary crystallographic direction. This spatial configuration within the nanoporous network, forming a triangular shape, is called triangular packing.

### Chlorine adatoms

Later on, we explore the interplay of chlorine Cl adatoms onto our system, followed by annealing processes, and try to explain how Cl atoms by electronegativity could play an interesting role in affecting the packing based on the STM image shown below.

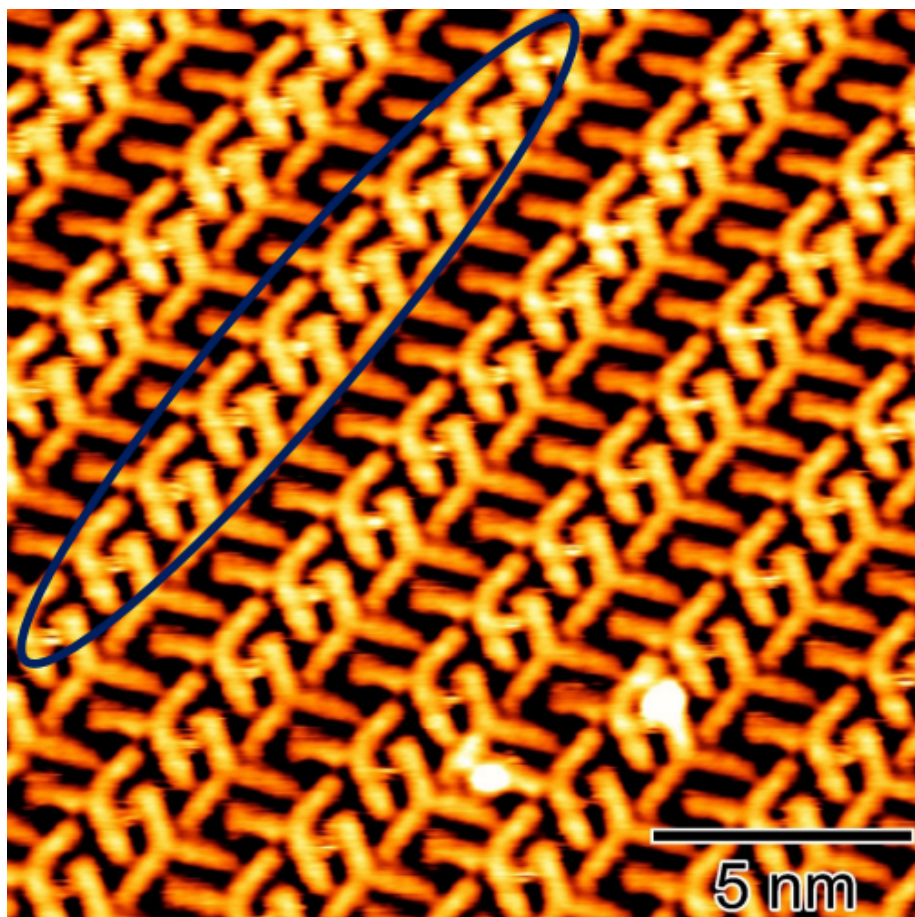


Figure 2.10: A new high-ordered structure emerges with Cl adatom isolation, and the main direction is aligned with the main crystallographic directions as depicted in Ceccatto et al. work<sup>117</sup>.

Fig. 2.10 arises from the interaction between isolated Cl atoms and the surface. The legs of the structure align themselves relative to the primary crystallographic direction, indicating a specific spatial configuration within the highly ordered nanostructure network. This configuration manifests as a pair of inverted TPYPB molecules, leading to inverted packing.



# Chapter 3

## Methodology

This section details the methodology used to create and characterize the 2D highly-ordered structures from essentially TPyPPB on Ag(111) and the interplay with the Cl adatoms experimentally, and computationally.

### 3.1 Experimental Details

The experimental details section provides a comprehensive overview of the methodology utilized for conducting the investigation. All experimental procedures and measurements were meticulously carried out in the surfaces lab at UNICAMP, Campinas (Brazil) under the expert supervision of Professor Abner de Sierbo and PhD (c) Alisson Ceccatto. Operating within ultra-high vacuum (UHV) conditions at a pressure of  $10^{-10}$  [mbar], the experimental setup comprises two chambers, each equipped with specialized instrumentation to facilitate precise measurements and observations. The first chamber is outfitted with indispensable tools, including X-ray photoelectron spectroscopy (XPS), low-energy electron diffraction (LEED) optics, a Knudsen cell for molecular sublimation, and an e-beam evaporator for metal deposition. These instruments play a crucial role in sample preparation and characterization, allowing for the deposition of molecular layers and metal films for subsequent analysis. A Scanning Tunneling Microscope (STM) setup featuring a SPECS Aarhus 150 STM and SPECS SPC 260 controller is employed in the second chamber. This setup is essential for high-resolution imaging and manipulating surface structures at the atomic level. Additionally, both chambers are equipped with Ar+ sputtering capabilities for tip cleaning, ensuring the cleanliness and reliability of the STM measurements. The STM operates under constant current conditions, enabling precise control and measurement of surface topography and electronic properties. Overall, the experimental setup provides a comprehensive platform for conducting detailed investigations into surface morphology, molecular assembly, electronic structure, bonding types, and material symmetry. To conduct this experiment, TPyPPB is deposited onto the gas phase atop the Ag(111) surface, followed by annealing to induce structural transformations, then waits a time on RT and observes the resulting configurations; by this process, it is possible to obtain the so-called triangular packing shown on sec 2.10.1.

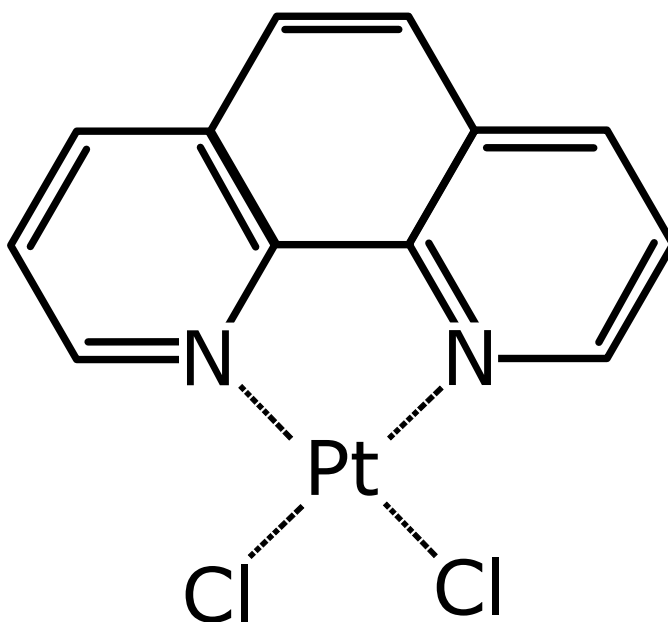


Figure 3.1: Dichloro(1,10-phenanthroline)Platinum(II)

Fig. 3.1 illustrates the chemical structure of the compound  $C_{12}H_8Cl_2N_2Pt$ , which we commonly call as  $Cl_2PhPt$ . This compound is used as a precursor by its dissociation of the Chlorine atoms at the 2D on-surface synthesis of our highly ordered nanostructures. The experimental procedure consisted of several steps:

1. Deposition of  $Cl_2PhPt$  for 40 minutes at higher coverages at room temperature (RT),
2. Annealing at 450 K for dehalogenation of  $Cl_2PhPt$ ,
3. Sputtering with  $Ar^+$  at 600 eV for 30 minutes,
4. Annealing at 770 K, and
5. Finally, the deposition of TPyPPB with annealing at RT.

Additionally, it was performed an experimental procedure with a different order of steps with first depositing the TPyPPB on the Ag (111) surface, then sputtering and annealing the  $Cl_2PhPt$  for its dehalogenation to end up annealing at RT.

## 3.2 Computational details

This work initially focused on the isolated TPyPPB in the gas phase. Subsequent calculations extended to explore both plausible packings on Ag(111), with and without Cl adatoms, to delve into the stability of the packing arrangement and its interaction with Cl adatoms via hydrogen bonding and a possible charge transfer.

For the DFT calculations were performed on GPAW<sup>116</sup> to do so, we employed the PBE exchange-correlation (xc) functional<sup>38</sup> as a semi-empirical method. To account for van der Waals (vdW) forces, Grimme's D3 correction<sup>67</sup> was applied, and all relaxations used for all systems during this thesis were performed with FIRE method<sup>118</sup>. Our KS wavefunctions were represented using the projected augmented wave method<sup>40</sup>, with a linear combination of atomic orbitals (LCAO)<sup>94</sup>. Specifically, we utilized a double  $\zeta$  polarized (DZP) basis set for the overlayer and adatoms (O, N, H, & Cl), while employing a single  $\zeta$  polarized (SZP) basis set for the atoms constituting the Ag(111) substrate. All the overlayer structures, such as TPyPPB and Cl, were relaxed until they reached a value less than  $0.03 \text{ eV}/\text{\AA}$  of maximum force in a  $5 \text{ \AA}$  vacuum in all three directions in space.

Regarding the packing arrangements, we can state their vectors based on the distance between silver atoms that we call  $a = 2.892$ . Therefore, the inverted packing reveals supercell dimensions defined as the following three vectors in each direction for the non-orthogonal cell:  $\mathbf{a}_1 = 14a\hat{i}$ ,  $\mathbf{a}_2 = 7a\hat{i} + 7\sqrt{3}a\hat{j}$ ,  $\mathbf{a}_3 = 25.6\hat{k}$ . On the triangular porous packing supercell features the following three vector directions for the non-orthogonal cell:  $\mathbf{b}_1 = 12a\hat{i} + 4\sqrt{3}a\hat{j}$ ,  $\mathbf{b}_2 = 8\sqrt{3}a\hat{j}$ ,  $\mathbf{b}_3 = 25.6\hat{k}$ . Additionally, both packing used  $17.6$  vacuum. Concerning the Brillouin Zone,  $\Gamma$ -point-defined calculations were utilized for both packings. Using a supercell, these calculations were sufficient to describe their wavefunctions. Additionally, each supercell had 4 TPyPPB molecules.

We conducted additional DFT calculations to explore theoretical spectroscopy in greater depth. For Resonant-Raman analysis of isolated TPyPPB shown in 2.6, we utilized the methodology outlined by Walter et al.<sup>119</sup> within the Atomic Simulation Environment (ASE) framework<sup>42</sup>. In this analysis, we opted for the Real-Space (RS) representation of the Kohn-Sham (KS) wavefunction<sup>41</sup>, employing a defined grid spacing of  $0.2 \text{ \AA}$  for the electron density. To emulate realistic conditions, we set an electronic temperature corresponding to  $k_B T = 0.025 \text{ eV}$  (equivalent to room temperature) and further extrapolated energies to  $T = 0 \text{ K}$ . The PBE exchange-correlation (xc) functional<sup>38</sup> was chosen for this analysis.

Lastly, we explored the applicability of the functional GLLB-sc exchange-correlation (xc), incorporating it along with the previously mentioned basis set for Linear Combination of Atomic Orbitals (LCAO). This allowed us to refine the representation of the electronic gap, mainly focusing on correcting for the derivative discontinuity present in the isolated gas phase TPyPPB. Through this approach, we obtained optical absorption spectra using the LCAO-TDDFT- $k$ - $\omega$  method<sup>35</sup>.



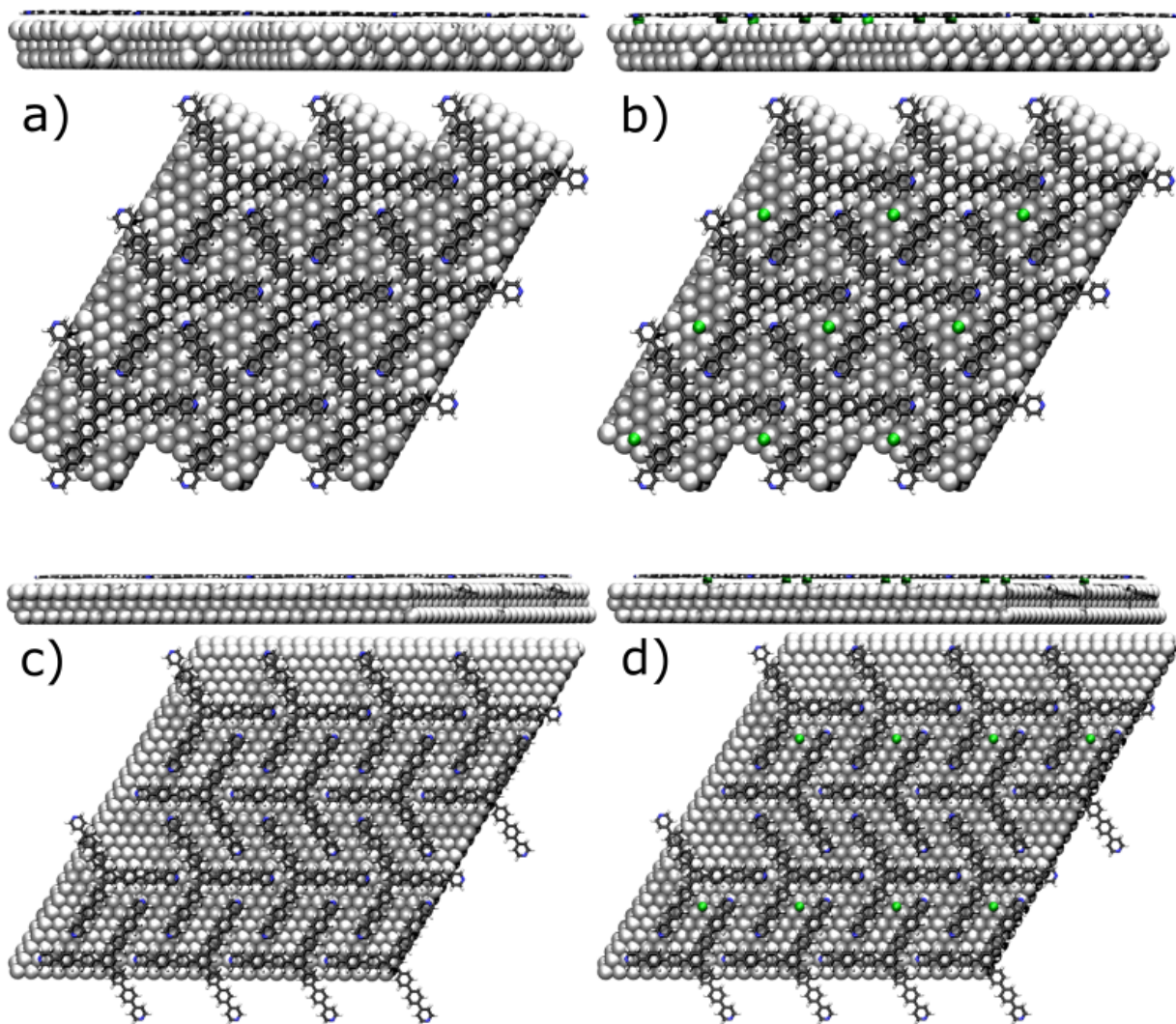


Figure 3.2: Structural configurations studied: (a) Triangular packing of TPyPPB on Ag(111), (b) Triangular packing with Cl adatom, (c) Inverted packing of TPyPPB on Ag(111), (d) Inverted packing of TPyPPB on Ag(111) with Cl adatom.

Fig. 3.2 depicts various structural arrangements (also called packing) of TPyPPB molecules on the Ag(111) surface, representing in white the Ag & H, in black C, and blue N. In (a) and (b), the molecules are arranged in triangular patterns, while in (b) and (d), Cl adatoms are incorporated into the structures. Notably, in (b) and (d), the Cl adatoms are located in the bridge and hollow sites of the Ag(111) surface, respectively, influencing the

molecular packing and interactions. These configurations were investigated to understand the stability and bonding characteristics of TPyPPB molecules on the Ag(111) surface, with and without Cl adatoms.



## Chapter 4

# Results & Discussion

In this project, we've amalgamated theoretical findings with experimental data from Scanning Tunneling Microscopy (STM) to comprehensively analyze mainly the topography. Our theoretical exploration began with Density Functional Theory (DFT) calculations, mainly focusing on formation energies to gain insights into the stability and intrinsic properties of the materials. This was complemented by theoretical spectroscopy split on vibrational, optical, and electronic. Additionally, charge analysis, excitonic activity at the highest optical activity energies by the LCAO-TDDFT- $k$ - $\omega$  code.

### 4.1 Formation Energies

All DFT calculations performed in this section used the Perdew-Burke-Ernzerhof exchange-correlation functional<sup>38</sup> complemented with the van der Waals corrections within the dispersion correction of the Grimme's D3<sup>39</sup>; these two combined are also known as PBE-D3 where the representation of the Kohn-Sham wave functions was represented as a Linear Combination of Atomic Orbitals<sup>94</sup> using two different basis sets: Single- $\zeta$ -polarized for Ag(111) atoms & Double- $\zeta$ -polarized for TPyPPB and Cl atoms. The calculators implemented the projected-augmented wave method<sup>40</sup> on GPAW<sup>41 116</sup> for the supercell described. The two packings with and without Cl adatom in 3.2. In this section, we examine how the formation energies of TPyPPB change with the addition of Cl atoms. Specifically, we studied the packing of the system with 0, 0.5, and 1 Cl adatoms per TPyPPB molecule shown in appendix A.

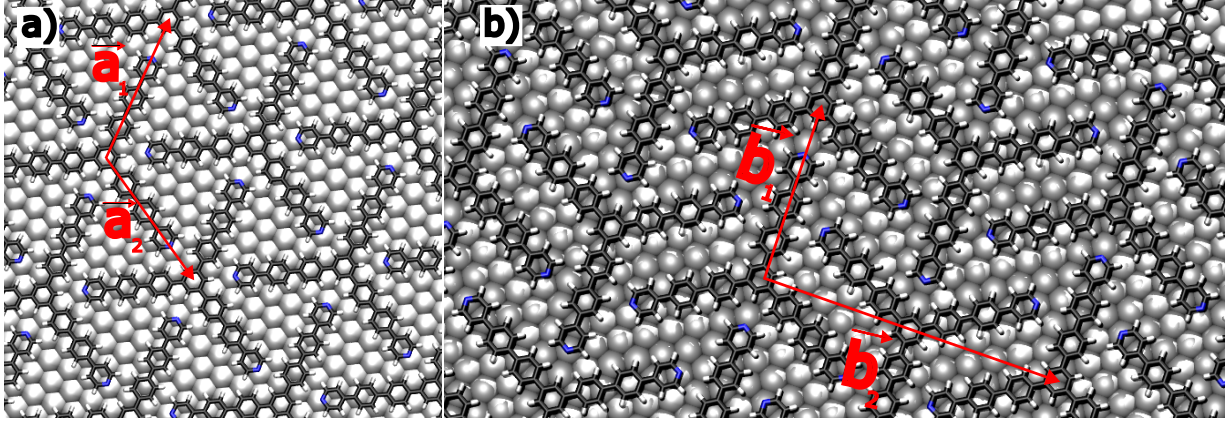


Figure 4.1: a) Hexagonal Triangular lattice vectors, b) Inverted Packing lattice vectors

The Triangular shown in a) 4.1 packing has a hexagonal unit cell with the following lattice vectors given in (nm):

$$\hat{\mathbf{a}}_1 = \begin{pmatrix} 1.9 \pm 0.1 \\ 0 \end{pmatrix}, \quad \hat{\mathbf{a}}_2 = \begin{pmatrix} 0 \\ 1.9 \pm 0.1 \end{pmatrix}$$

Consider that the last mentioned lattice vectors are rotated from the main crystallographic directions of the substrate in  $30^\circ$ , taking one molecule per unit cell. The Inverted packing shown in b) 4.1 has the following lattice vectors given in (nm):

$$\hat{\mathbf{b}}_1 = \begin{pmatrix} 1.9 \pm 0.1 \\ 0 \end{pmatrix}, \quad \hat{\mathbf{b}}_2 = \begin{pmatrix} 0 \\ 3.4 \pm 0.1 \end{pmatrix}$$

Those vectors are aligned in the main crystallographic direction, taking two molecules per unit cell. The **formation energies**  $E_{form}$  per TPyPPB molecule were calculated based on Cettato's<sup>29</sup> previous work as:

$$E_{form} = N_{ads}(E[Ads@Ag(111)] - E[Ag(111)] + N_{Cl}(E[Cl@Ag(111)] - E[Ag(111)] - (E_{Total} - E[Ag(111)])) \quad (4.1)$$

where  $N_{ads}$  is the number of adsorbate molecules, in this case, the number of TPyPPB, and  $N_{Cl}$  is the number of Chlorine adatoms,  $E[Ads@Ag(111)]$  is the total energy of a single TPyPPB being adsorbate on the Ag(111) surface,  $E[Ag(111)]$  is the total energy of the Ag(111) surface without any adsorbate,  $E[Cl@Ag(111)]$  is the total energy of an isolated Ag adatom adsorbed on the most stable site i.e. the hollow site of the Ag(111) surface, finally  $E_{Total}$  corresponds to the total energy of the specific system we calculating the formation energy which is made by  $N_{ads}$  molecules and  $N_{Cl}$  adatoms.

Table 4.1: Difference in formation energies

Packing	Cl atoms per TPyPPB molecule	$\Delta E_{form}$ (eV)
Triangular	0	0.29
	$\frac{1}{2}$	0.50
	1	0.66
Inverted	0	0.22
	$\frac{1}{2}$	0.34
	1	0.50

Table 4.1 takes the differences in the formation energies of the systems with Cl adatoms concerning both systems without. In addition, the Chlorine atoms isolated on Ag(111) tend to be in the most stable hollow site<sup>120</sup>; from our results for inverted packing shown in Fig 1 of A, the Cl adatoms are in the hollow site. However, in the case of triangular packing shown in Fig 2 of A, the Cl adatoms are at the bridge site.

## 4.2 Vibrational Spectroscopy

### 4.2.1 Isolated TPyPPB on gas phase

For vibrational spectroscopy conducted on the TPyPPB isolated on gas phase, it was conducted DFT calculations with the RS<sup>41</sup> for the representation of the KS wavefunctions with the following cell vectors:  $\mathbf{c}_1 = 50.21\hat{i}$ ,  $\mathbf{c}_2 = 25.19\hat{i} + 43.64\hat{j}$ ,  $20.98\hat{k}$ .

Table 4.2: FTIR active vibrational modes of TPyPPB

Symmetry	Mode	Type	Wavenumber ( $cm^{-1}$ )
$A_1$	$\beta[N-C=C]$	bending	590
$A_1$	$\omega[N-C=C-H]$	wagging	790
$A_1$	$\nu[C=C]$	stretching	1591
$A_1$	$\nu[C-H]$	stretching	3114

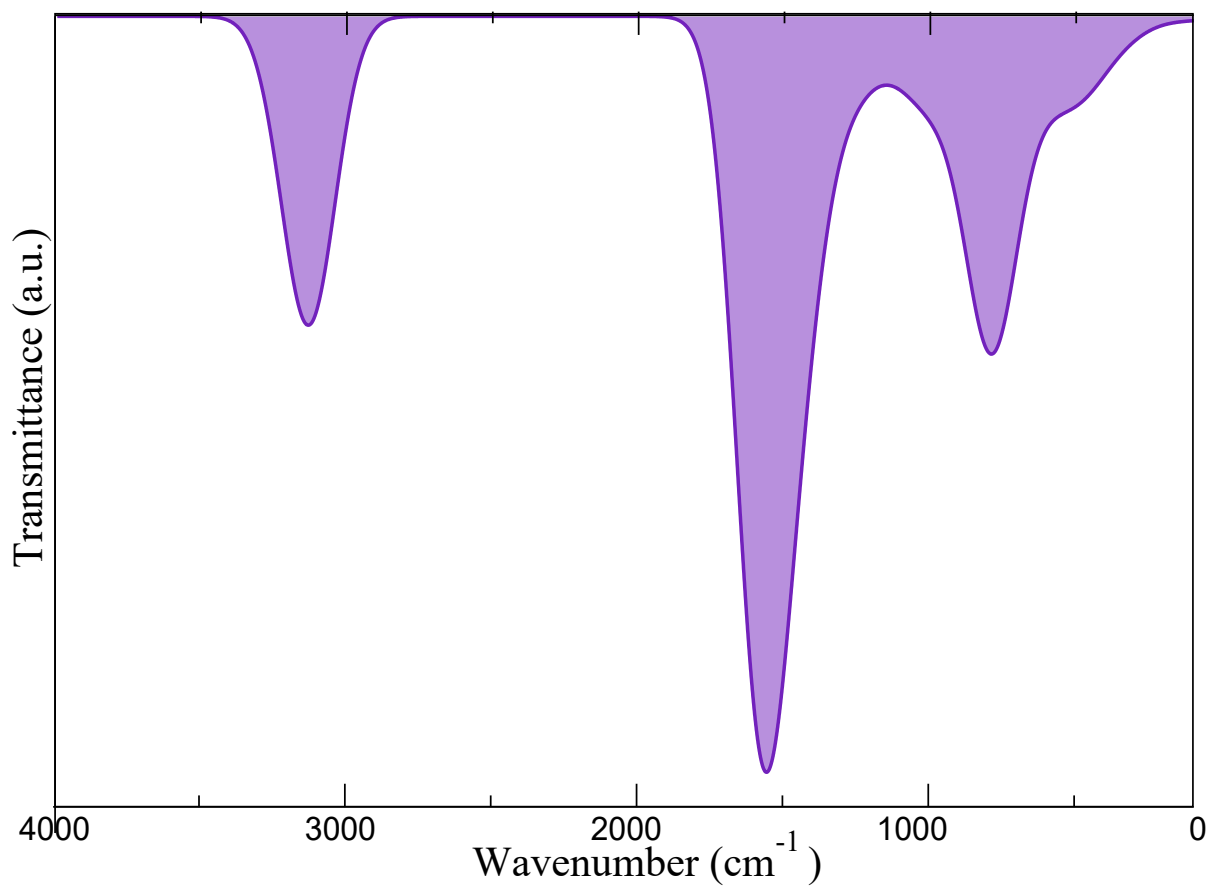


Figure 4.2: Simulated Fourier transform infrared (FTIR) transmittance in arbitrary units versus wavenumber in  $\text{cm}^{-1}$  for isolated TPyPPB in color indigo.

The wavenumbers of the peaks shown in Fig. 4.2 are depicted in table 4.2 with the respective description of the vibrational mode and symmetry of the modes. Although, TPyPPB is planar the only symmetry we got so far presented is  $A_1$ .

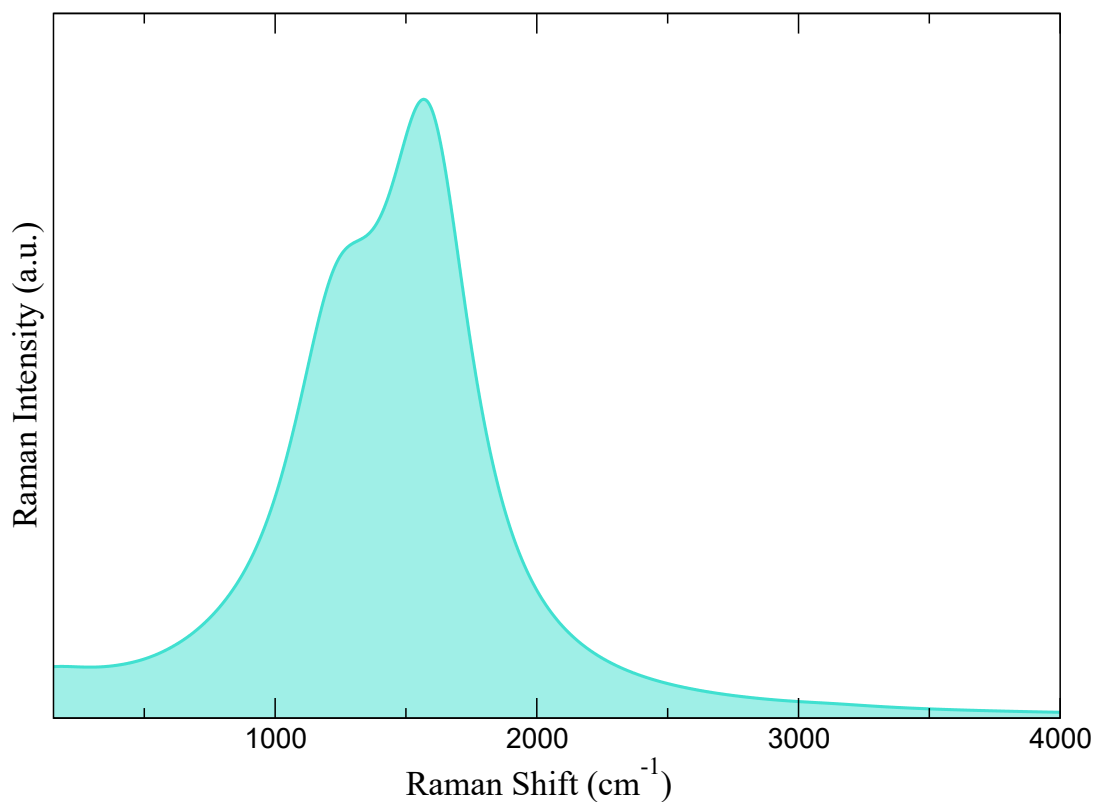


Figure 4.3: Simulated Raman of isolated TPyPPB in turquoise Raman intensity versus Raman shift in  $cm^{-1}$ .

Additionally, Raman calculations used an  $\omega$  equal to 2.45 eV that in nm is equivalent to 506.05 nm. The active vibrational modes of Fig. 4.3 are depicted with the symmetries in table 4.3 demonstrating that C=C functional group of isolated TPyPPB is neither Raman and FTIR active at approximately 1590.

Table 4.3: Raman active vibrational modes of TPyPPB

Symmetry	Mode	Type	Wavenumber ( $cm^{-1}$ )
$A_1$	$\omega[N-C=C-H]$	wagging	1216
$A_1$	$\beta[C=C-H]$	bending	1583

#### 4.2.2 Highly ordered self-assembled monolayers on Ag(111)

Fourier transform infrared simulations were applied to four highly ordered monolayers with and without Cl atoms for the two different emerged packings.



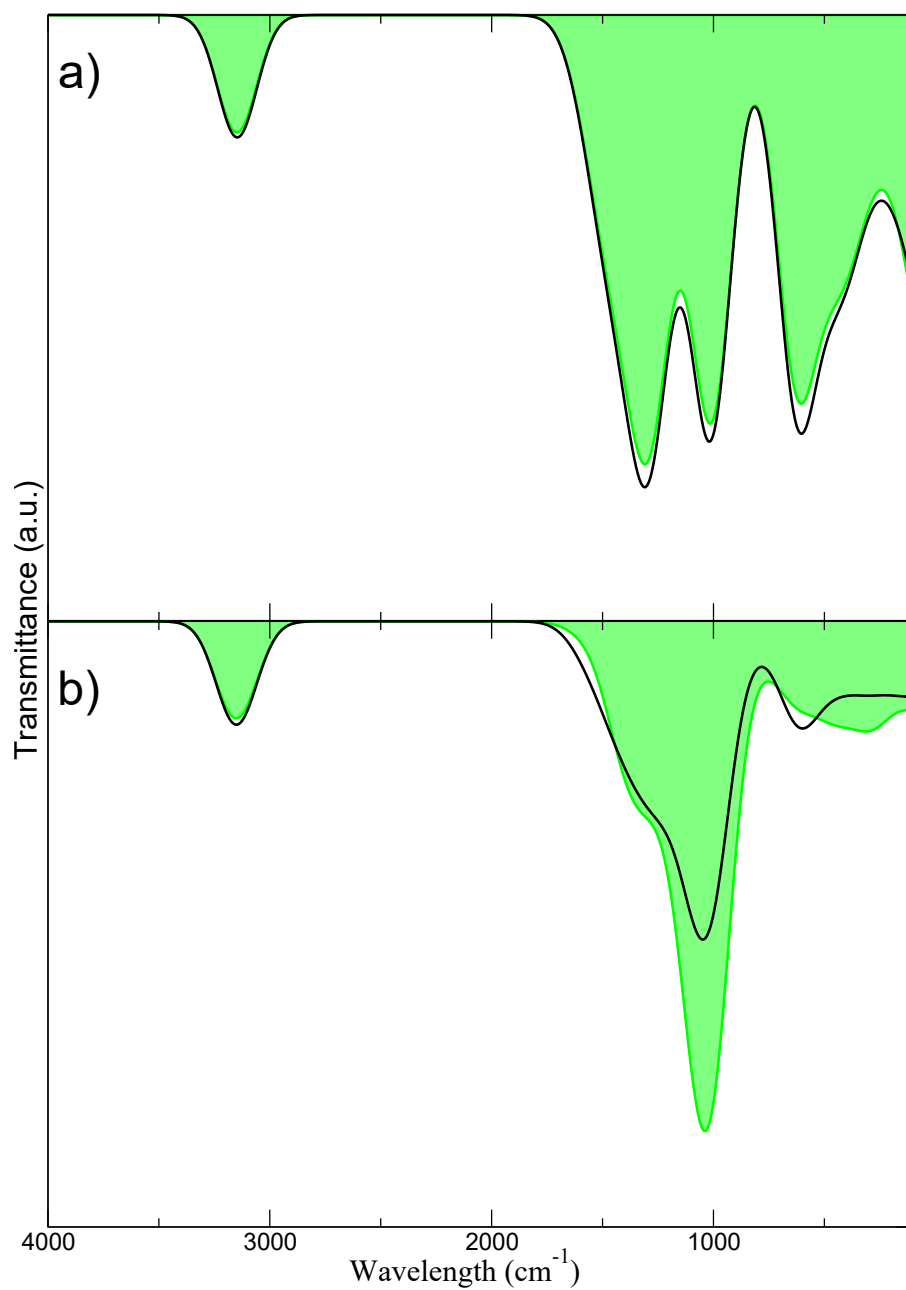


Figure 4.4: Simulations of FTIR in wavelength  $\text{cm}^{-1}$  vs transmittance (a.u.). a) FTIR for triangular packing: in black without Cl adatoms and in green with one Cl adatom per TPYPB molecule, b) FTIR for inverted packing: in black for without Cl adatoms and in green with half Cl adatom per TPYPB molecule.

Fig. 4.4 shows in a) & b) the same wavelength for all peaks depicted in table 4.4. However, the ratios' intensity varies, and the peak ratios vary due to the difference in the spatial arrangement of the highly ordered triangular nanoporous.

Table 4.4: FTIR active vibrational modes of TPyPPB on Ag(111) packings

Symmetry	Mode	Type	Wavenumber ( $cm^{-1}$ )
$A_1$	$\beta[N-C=C]$	bending	608
$A_1$	$\omega[N-C=C-H]$	wagging	1020
$A_1$	$\nu[C=C]$	stretching	1310
$A_1$	$\nu[C-H]$	stretching	3150

From FTIR table 4.4 comparing it with 4.2, it can be stated that vibrational mode presented a clear shift because of the physisorption of TPyPPB on Ag(111).

Table 4.5: Ratios between intensities

Structure	$\frac{I_{N-C=C-H}}{I_{C-H}}$	$\frac{I_{C=C}}{I_{C-H}}$
TPyPPB	1.09	2.45
Triangular packing	3.48	3.84
Triangular packing with Cl	3.47	3.87
Inverted packing	3.07	1.76
Inverted packing with Cl	5.49	2

Table 4.5 shows the ratios of the intensities concerning the intensity of the C-H vibrational mode similarly as depicted in Ref. 36.

### 4.3 UPS

In this section, we provide a UPS for the Isolated TPyPPB (from PBE<sup>76</sup> functional with the Grimme's<sup>67</sup> correction with LCAO)& both packing arrangements (from DFT calculations described for supercell in 3.2) based on the density of states without guessing the secondary electrons. Both packings described below have 0.5 Cl adatoms per TPyPPB molecule. Additionally, the isolated Ag(111) for each supercell.

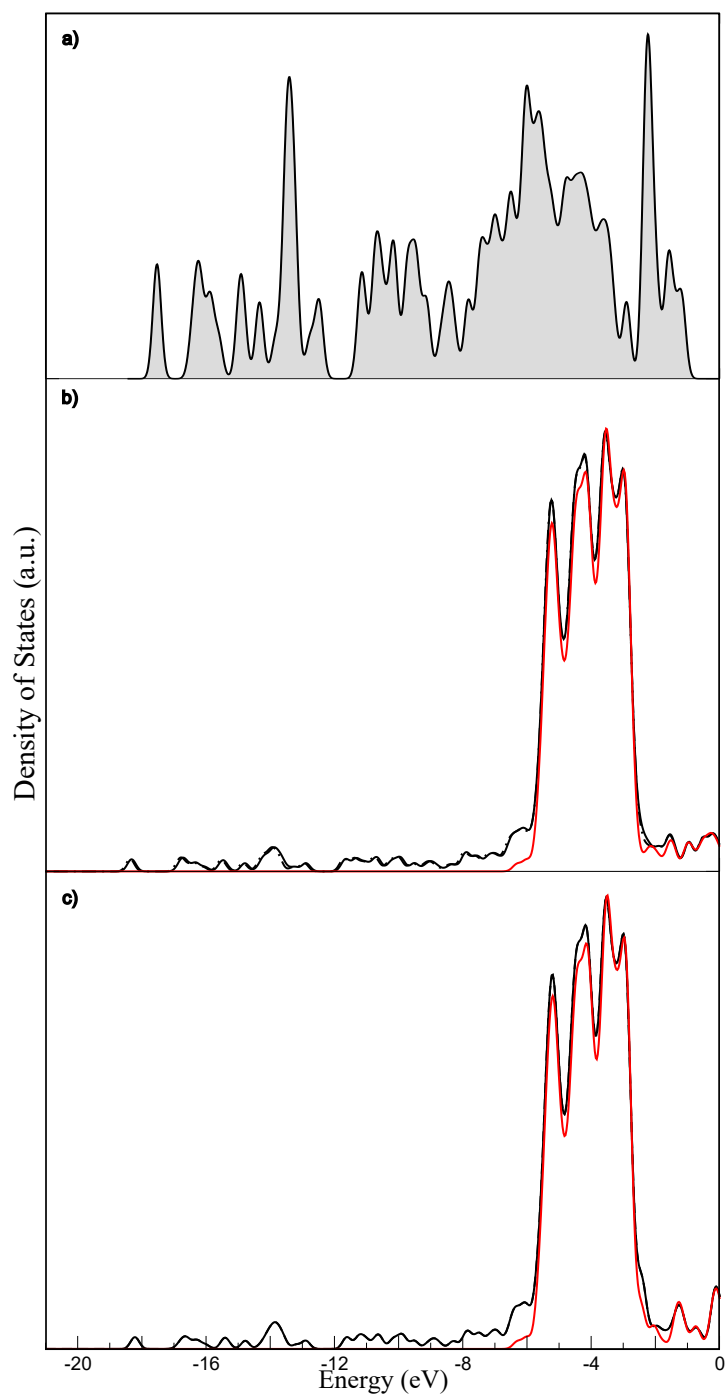


Figure 4.5: Occupied states, Energy (eV) from -23 to 0 (Fermi Level set at 0 eV) versus Density of states in arbitrary units. a) TPyPPB isolated. b) Triangular Packing UPS: in red, the Ag(111) Slab is isolated; in black, the triangular packing is with Cl adatom, in ... the triangular packing is without Cl atoms. c) Inverted Packing UPS with the same color format as literal b).

Fig. 4.5 shows our representation of UPS where are shown the occupied states. In addition, as a) is an insulator it is possible to discern a band gap.

## 4.4 IPES

This section presents an Inverse Photoemission Spectroscopy (IPES or IPS) for isolated TPyPPB, packing arrangements, and Ag(111) isolated surface (same as section 4.3). Both packings detailed below have 0.5 Cl adatoms per TPyPPB molecule. IPES provides a powerful technique for investigating unoccupied electron energy levels<sup>121</sup> on clean and adsorbate-covered surfaces<sup>122</sup>.

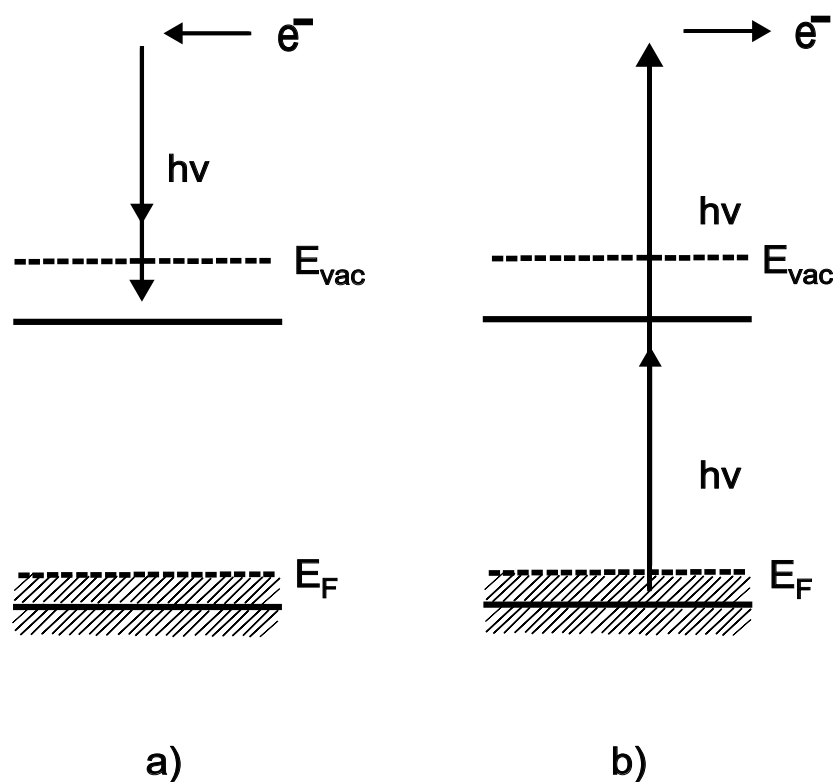


Figure 4.6: Schematic of IPES process. Unoccupied-state photoemission involves two processes: (a) Inverse photoemission, where an electron fills an empty state, resulting in the emission of a photon; (b) Two-photon photoemission, where the first photon excites an electron to fill the previously unoccupied state, and a second photon then causes the emission of this electron<sup>123</sup> adapted from Ref. 123.

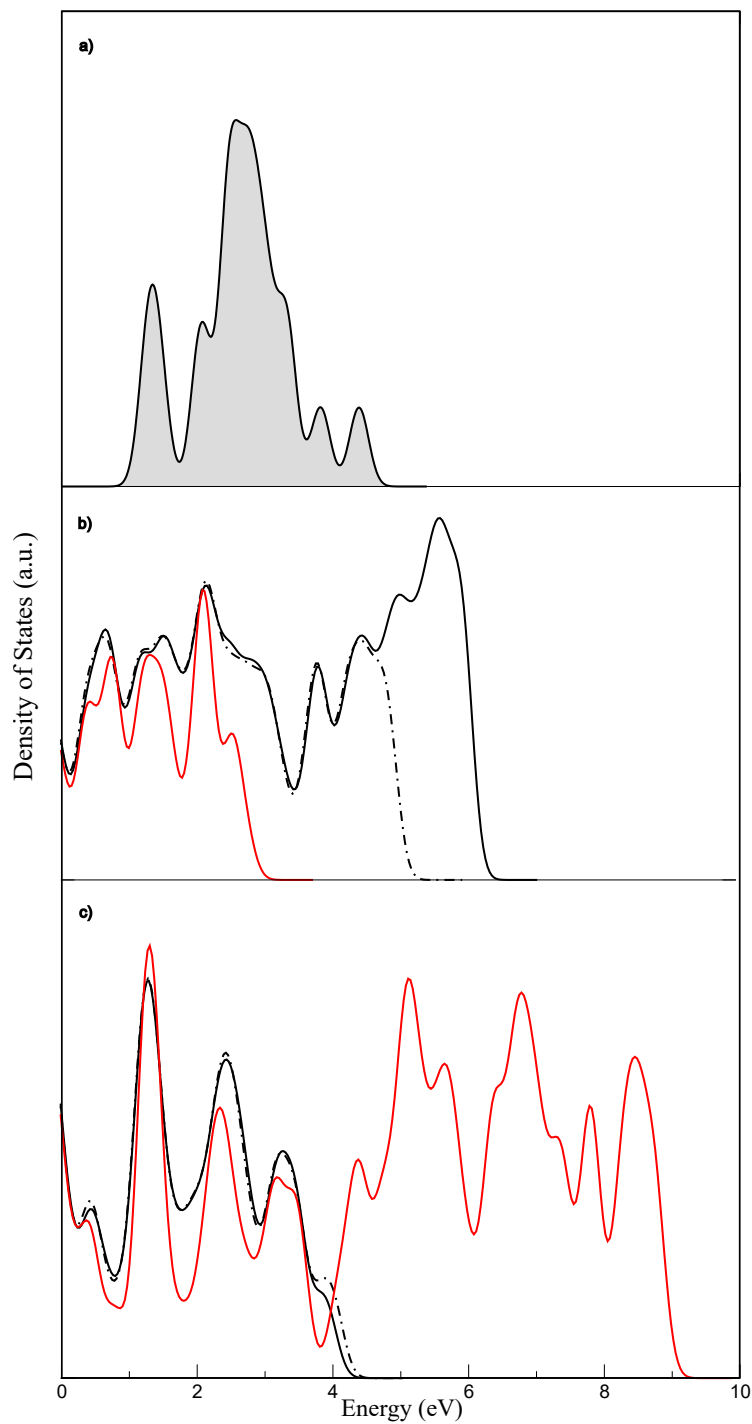


Figure 4.7: Unoccupied states, Energy (eV) from 0 to 10 (Fermi Level set at 0 eV) versus Density of states in arbitrary units. a) TPyPPB isolated. b) Triangular Packing IPES: in red, the Ag(111) Slab is isolated; in black, the triangular packing with Cl adatom, in  $\dots$  the triangular packing without Cl atoms. c) Inverted Packing IPES: in red, the Ag(111) Slab isolated; in black, the inverted packing with Cl adatom, in  $\dots$  the inverted packing without Cl atoms.

IPES was first applied to organic materials in the 1980s<sup>122,124–126</sup>. By IPES, we can explore how the adsorbate plays a crucial role within the  $\pi$  electrons interacting with the surface and affecting the unoccupied states. In other terms, the density of unoccupied states can be measured by inverse photoemission experiments<sup>121</sup>. In principle, the last statement makes IPES a great complement to UPS. Fig. 4.6 gives an insight into the experimental theory of how photons cause the emission of some electrons by exciting them to jump into unoccupied states to later be able to map out that empty states or conduction band for an insulator as TPyPPB. Fig. 4.6 is only a scheme. However, we map the unoccupied states based on DOS, and as depicted in Fig. 4.7 the presence of Ag(111) fills empty states of TPyPPB making it behave as a metal. In addition, Fig. 4.7 for a) it can easily denote its insulator behavior by a band gap, b) depicts unoccupied states of triangular packing with a wide range of energy contrasted to the slab of triangular packing cell isolated, c) the unoccupied states of the inverted packing isolated slab are close to 10 eV, however, as the packing is created the unoccupied states shift closely to 5 eV.

## 4.5 Projected density of states

To further study the electronic structure and complement the previous results from sections 4.3 and 4.4, this section presents the density of states for the isolated TPyPPB in the gas phase. Additionally, it focuses on the projected density of states for both packing structures, with and without a 1/2 Cl adatom per TPyPPB. This analysis aims to examine the electronic structure of the adsorbate and the superficial atoms of Ag.

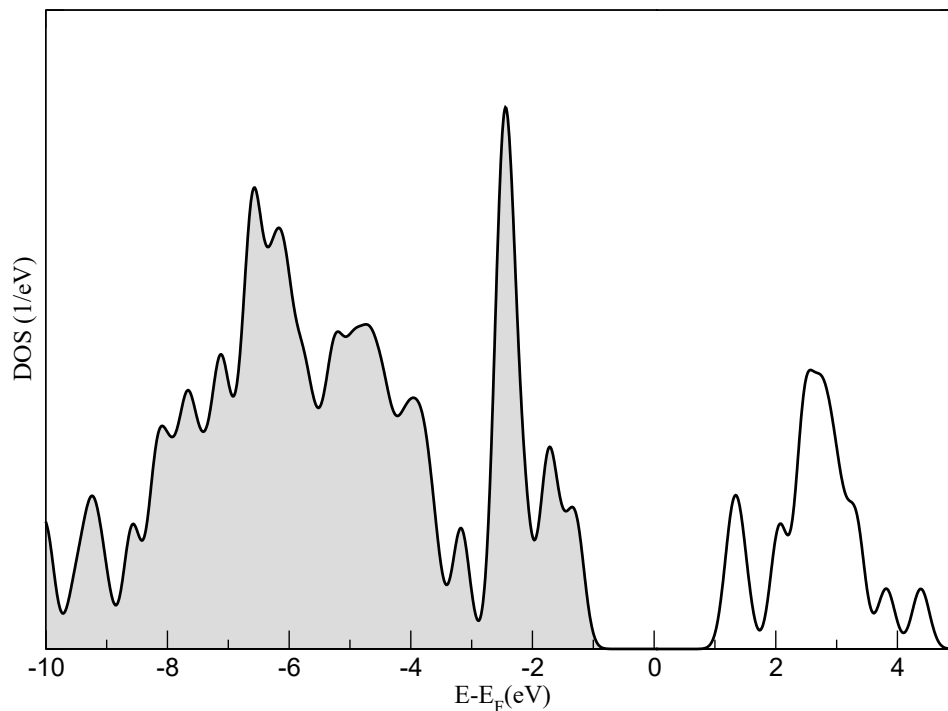


Figure 4.8: DOS versus Energy with the fermi level set at zero analysis of isolated TPyPPB on gas phase.

Figure 4.8 shows the density of states (DOS) of TPyPPB with a clear bandgap greater than 1 eV, so demonstrating that TPyPPB is an insulator. When comparing this with Figures 4.10 and 4.9, it becomes evident that the Ag(111) surface significantly influences the electronic structure in a detailed way. The interaction with the Ag(111) surface reduces the bandgap of all species on top of it to 0 eV, as the surface shares its electronic states. Fig. 4.10 and 4.9 show the occupied states filled with the Fermi level set at zero also compared with Fig. 4.8 it shows how occupied and unoccupied levels are filled due to Ag(111) presence. Additionally, the main contribution to the electronic structure of the overlayer is the Carbon atoms through  $\pi$  electrons as expected.

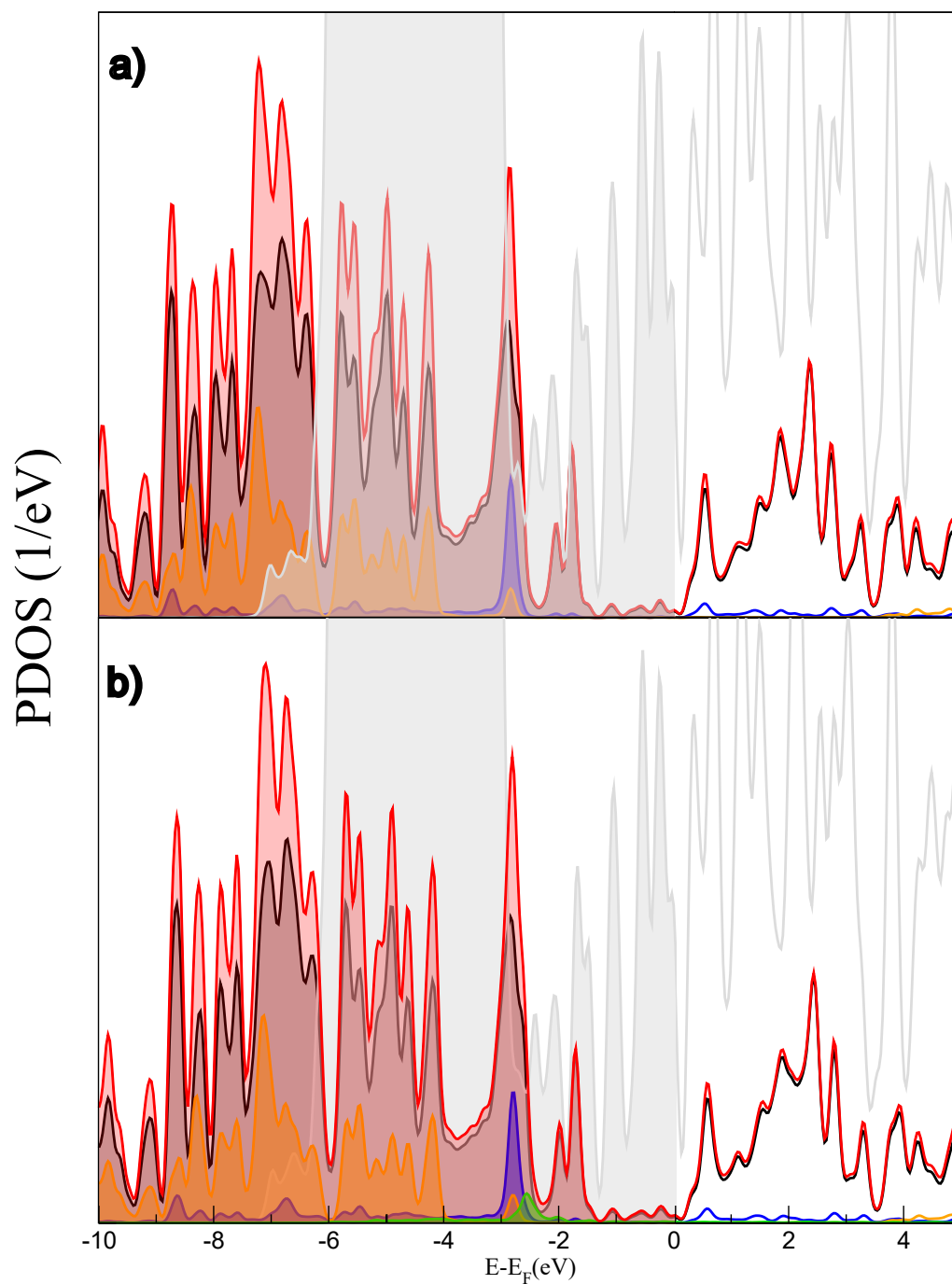


Figure 4.9: PDOS (1/eV) versus Energy with the fermi level set at zero analysis of the high ordered structure for triangular Packing; a) PDOS on surface Ag(111) atoms (grey), on surface TPyPPB (red), Carbon sp (black), Nitrogen sp (blue), Hydrogen (orange). b) PDOS on surface Ag(111) atoms (grey) and adsorbate TPyPPB-Cl (red), Carbon sp (black), Nitrogen sp (blue), Hydrogen s (orange), and Chlorine sp (green).



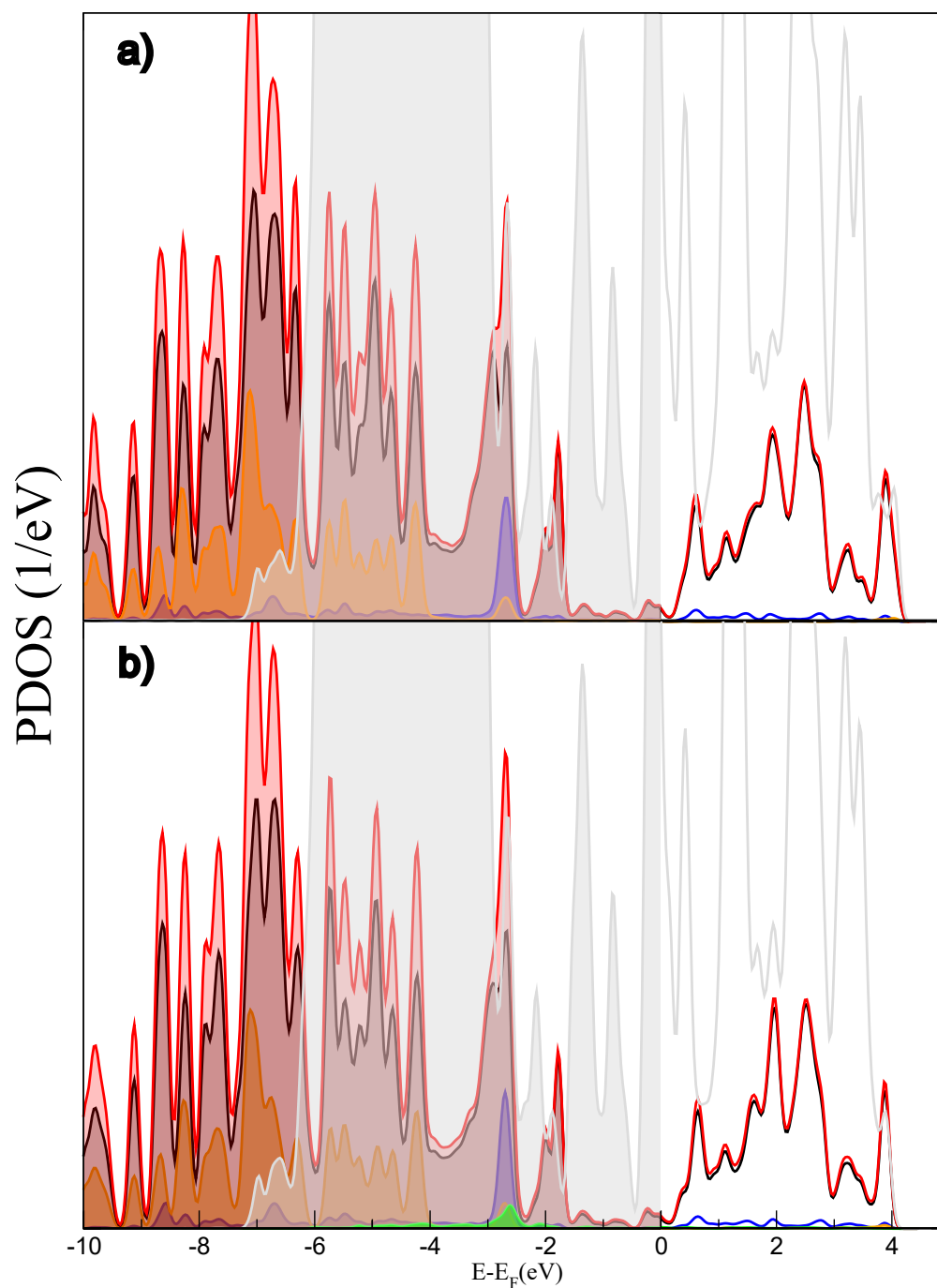


Figure 4.10: PDOS (1/eV) versus Energy with the fermi level set at zero analysis of the high ordered structure for inverted Packing; a) PDOS on surface Ag(111) atoms (grey), on surface TPyPPB (red), Carbon sp (black), Nitrogen sp (blue), Hydrogen (orange). b) PDOS on surface Ag(111) atoms (grey) and adsorbate TPyPPB-Cl (red), Carbon sp (black), Nitrogen sp (blue), Hydrogen s (orange), and Chlorine sp (green).

## 4.6 Charge Transfer

In this section, it is shown the charge transferred between TPyPPB-Ag(111) and Cl (if the case) by using the grid-based Bader analysis method<sup>44,105</sup>. In this way, we further understand the Cl atoms' interaction within TPyPPB-Ag(111) and how the charge is distributed from the metallic silver to the adsorbate. However, our main statement is that Cl adatoms may gain an interesting charge due to their high electronegativity. Indeed below are detailed in a table the results of the Bader analysis for both packing without Cl atoms:

Table 4.6: Charge transfer of both packings with no adatoms

Packing	Charge gained per TPyPPB molecule (e)
Triangular Packing	0.22
Inverted Packing	0.19

Based on the table 4.6, Ag(111) transfers some charge to the molecules on top. Triangular packing is gaining a difference of  $\approx 0.03$  (e) concerning the inverted packing.

Table 4.7: Charge transfer of both packings with 1/2 Cl atoms per TPyPPB molecule

Packing	Charge gained per TPyPPB molecule (e)	Charge gained per Cl atom (e)
Triangular Packing	0.14	0.56
Inverted Packing	0.13	0.52

From table 4.7, the difference in charge transferred of Cl atoms from both packings  $\approx 0.04$  (e) which is more significant in comparison to the difference in charge transferred of TPyPPB of both packings  $\approx 0.01$  (e), suggesting that Cl atoms in triangular packing receive more charge from the Ag(111) compared to inverted packing.

## 4.7 LCAO-TDDFT- $\mathbf{k}$ - $\omega$

The computational methods employed during this project, such as density functional theory (DFT), accurately calculated the energies of the orbitals for the different eigenstates, which provides an incredible insight into the description of the electronic structure of our system<sup>127</sup>.

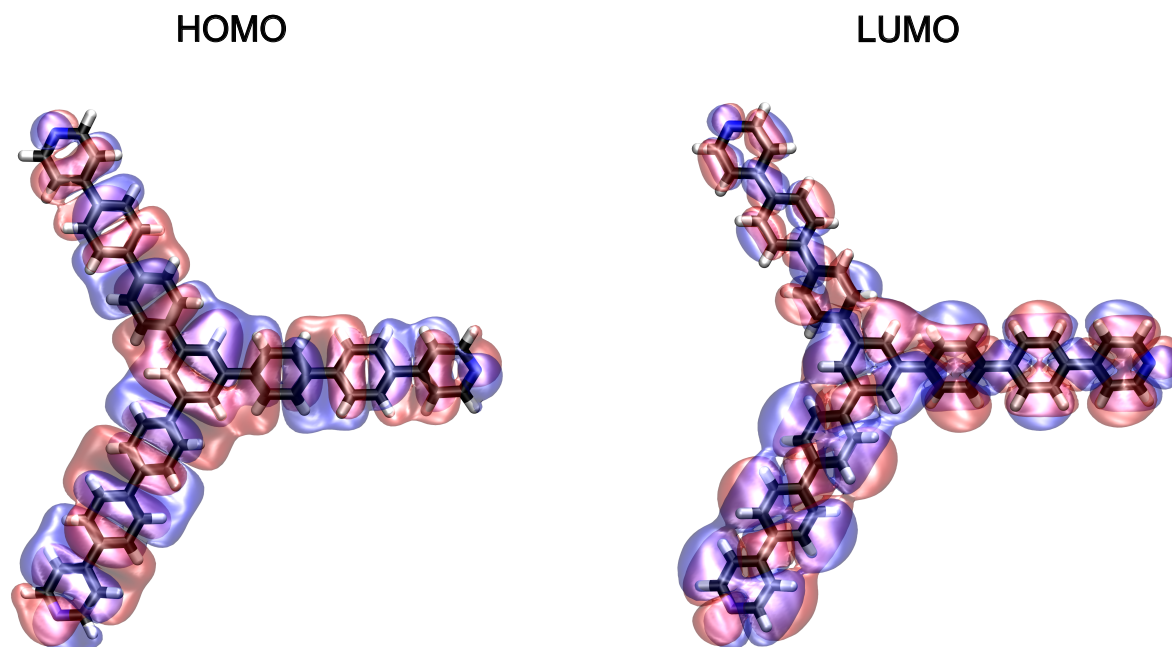


Figure 4.11: Top view of the HOMO and LUMO (in red holes and blue for electrons) for TPyPPB molecule.

The highest occupied molecular orbital (HOMO) and the lowest unoccupied molecular orbital (LUMO) are key concepts in understanding how orbital interactions stabilize combined systems. The energy gap between these orbitals, known as the HOMO-LUMO gap, is crucial for determining a molecule's chemical reactivity, stability, and electronic properties<sup>128</sup>. Fig. 4.11 used a isovalue of  $\pm 0.0006e/a_0^3$ , with Bohr radius approximately  $a_0 \approx 0.529177\text{\AA}$ . This value aids in visualizing the molecular orbitals.

Electron delocalization, particularly in organic molecules like TPyPPB with  $\pi$ -conjugated electrons, significantly influences charge transfer within metallic surfaces<sup>129</sup>. The optical properties of materials, such as their photovoltaic capabilities, can be studied through the behavior of  $\pi$  delocalized electrons from organic molecules.

To explore the optoelectronic properties of TPyPPB, we employed the GLLB-SC functional with the LCAO representation of the KS wavefunctions. For the isolated TPyPPB system, this approach yielded a bandgap of 4.23 eV and a derivative discontinuity correction  $\Delta_x$  of 1.26 eV. Subsequently, we used the LCAO-TDDFT- $k$ - $\omega$  code<sup>35</sup> to determine the Optical Absorption Spectrum (OAS) and the exciton density generated by photon-electron interactions.

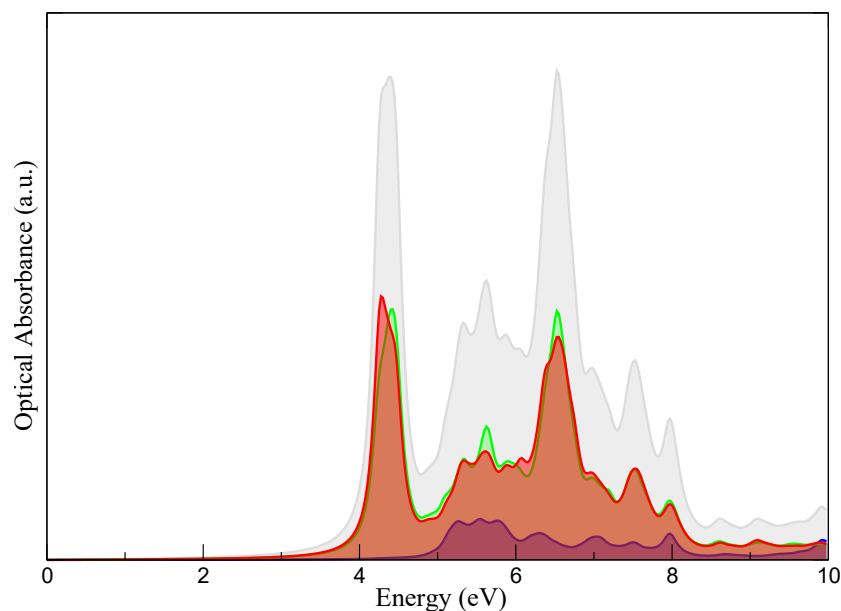


Figure 4.12: Optical absorption spectrum obtained from LCAO-TDDFT- $k\omega^{35}$  for TPyPPB isolated molecule with GLLB-sc exchange-correlation functional showing the Optical Absorbance in arbitrary units versus the energy. In grey the summed OAS of all three polarization axes which is decomposed in three colors y-green, red-x, and blue-z.

Fig. 4.13 used a value of the wavefunction isovalue of  $\pm 1 \times 10^{-6}$  ( $e/a_0^3$ ) for exciton density illustrations. Fig. 4.12 reveals an increase in the optical absorbance at 4 eV followed by the peak at 4.4 eV. In addition, a second significant peak at 6.52 eV. In addition, those peaks are approximately 281 nm and 190 nm, respectively, in the ultraviolet range. The exciton activity at 281 nm or 4.4 eV shows a significant exciton activity. Additionally, exciton density was only performed for the x and y direction of the polarizing light because those are the main contributors shown in Fig. 4.12. The two highest intensities at the OAS show two transitions. The first, HOMO-2 $\rightarrow$  LUMO at 4.4 eV, the second HOMO-13 $\rightarrow$  LUMO+10 at 6.52 eV.

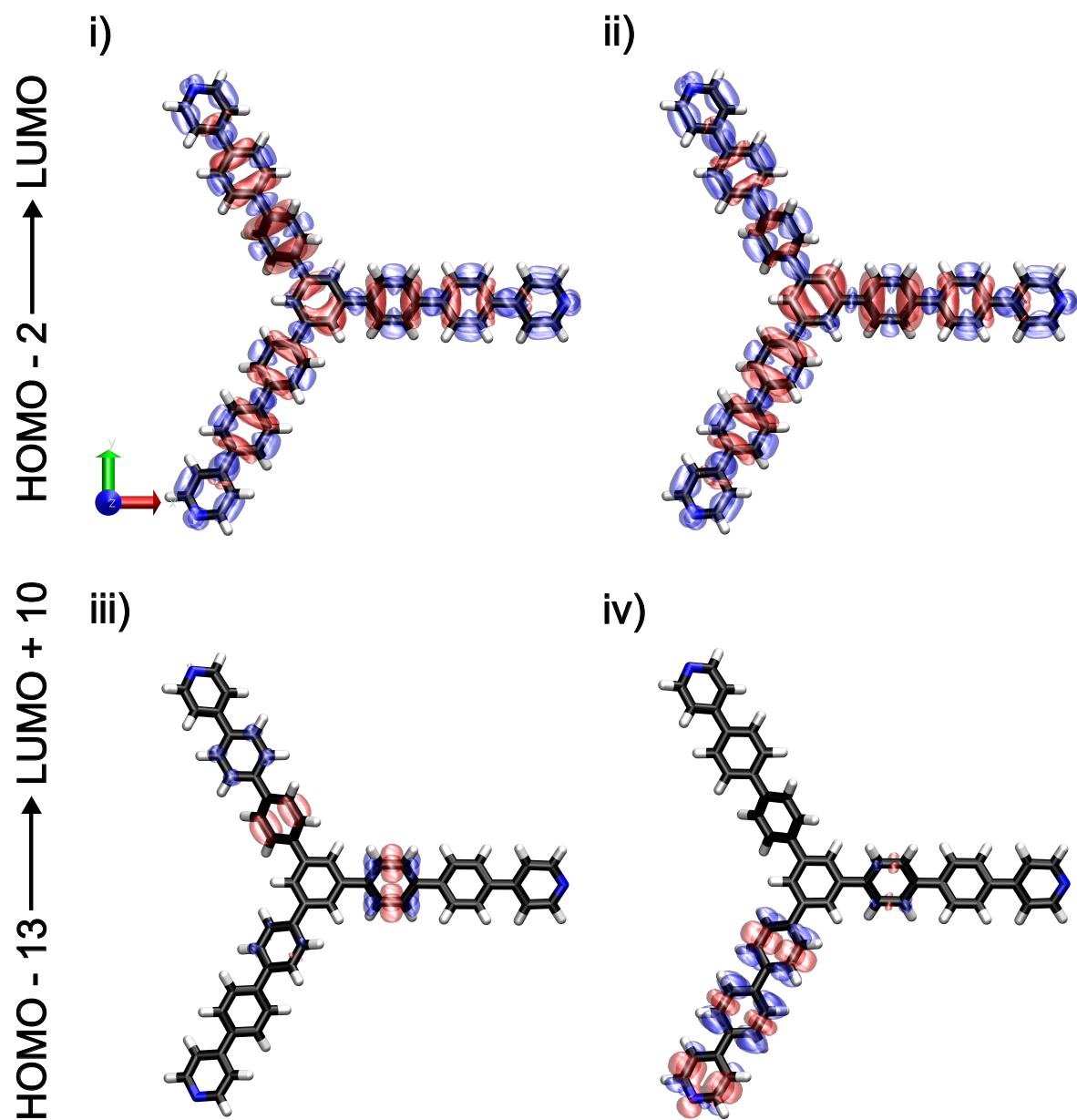


Figure 4.13: Exciton density with the transitions at the two peaks energies of Fig.4.12 from the top view with the polarization of the incident light for x and y respectively.

## 4.8 STM

Scanning Tunneling Microscopy (STM) is a great technique for measuring and analyzing the topography surface in materials. STM was performed for both packing with and without Cl atoms experimentally and theoretically. However, STM simulations used 1/2 Cl atom per TPyPPB on inverted packing, and 1 Cl atom per TPyPPB on triangular packing.

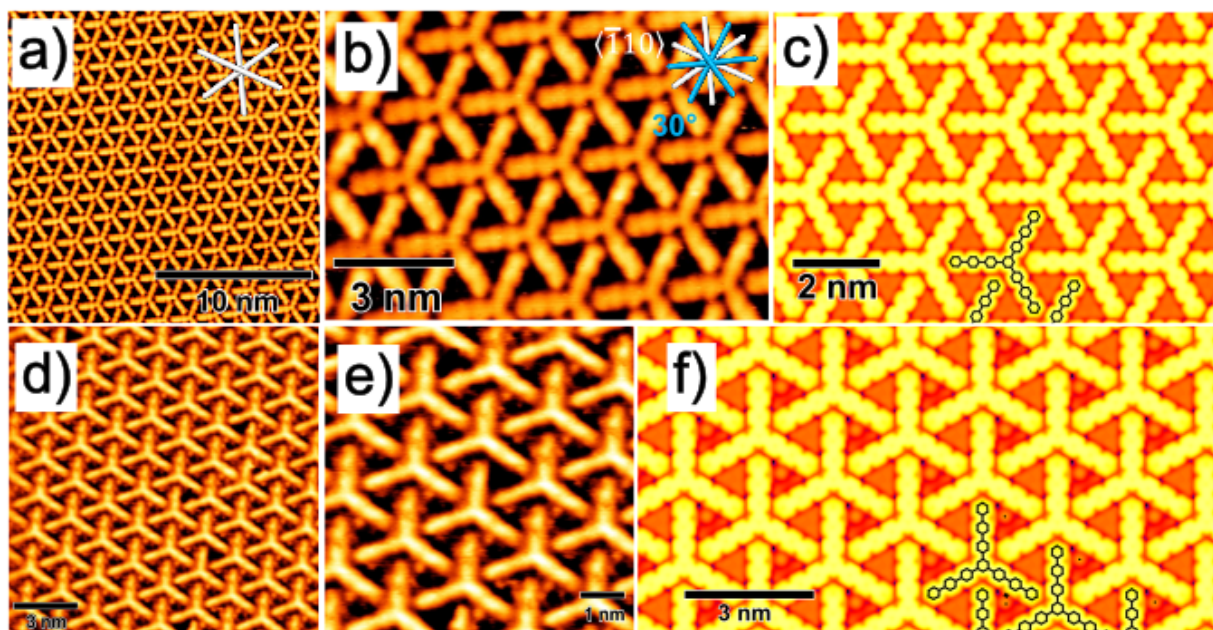


Figure 4.14: a),b),c) STM of the triangular nanoporous with  $V_{Bias}=-1.0$  V d),e),f) STM of the triangular packing with Cl atoms with  $V_{Bias}=-0.88$  V. c) and f) are simulated STM images and a),b),c),d),e) experimental STM images adapted from 117.

Fig. 4.14 compares theoretical and experimental STM set at the same voltage bias. The main crystallographic directions on the top-right denote the rotation of  $30^\circ$ . In addition, the 2D self-assembly had a triangular nanoporous area of  $\approx 1.7$  nm<sup>2</sup> with a molecular density of  $(0.32 \pm 0.02) \frac{mol}{nm^2}$ <sup>117</sup>. Furthermore, Fig. 4.14 f) denotes Cl atoms as black dots.

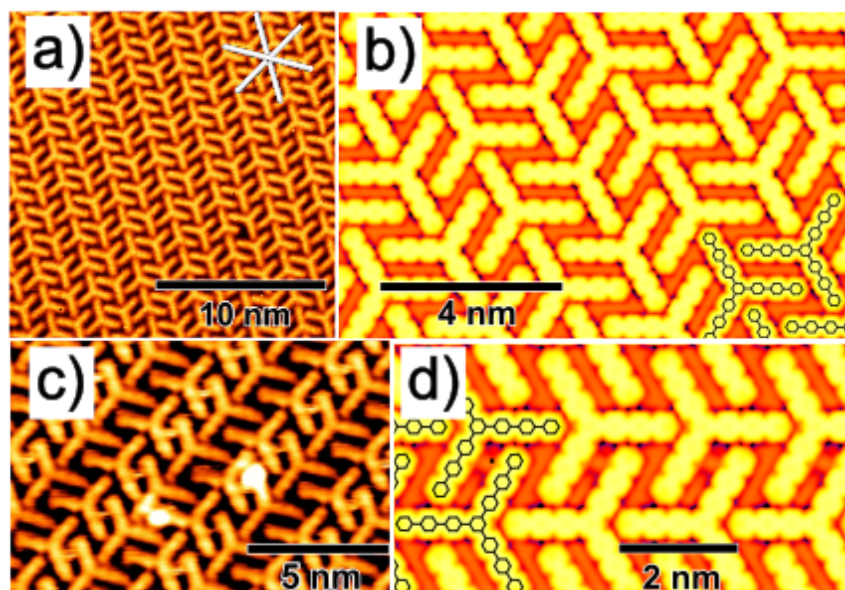


Figure 4.15: a), b) STM of the highly ordered inverted packing structure with  $V_{Bias}=-1.3$  V. c), d) Packings with the Cl atoms performed to a  $V_{Bias}=-0.90$  V. a),b) are experimental STM, and c),d) are theoretical STM simulations adapted from Ref. 117.

Fig. 4.15 mainly compares both experimentally and theoretical images, and denotes the main crystallographic direction being aligned to it, also, inverted packing exhibit a molecular density of  $(0.30 \pm 0.02) \frac{mol}{nm^2}$ <sup>117</sup>. Additionally, Fig. 4.15 d) denoted the Cl atoms as small black dots.

## Chapter 5

# Conclusions & Outlook

On-surface two-dimensional (2D) highly ordered nanomaterial synthesis can enhance properties and functionalities, including photoelectric, nanoelectronic, catalytic properties, and separation of small molecules or gases. This thesis investigates the behavior of an organic three-legged molecule, 1,3,4-tris[4-(pyridine-4-yl)-[1,1'-biphenyl]benzene, referred to as TPyPPB. The electronic orbitals of TPyPPB, particularly the  $\pi$  electrons in the phenyl and pyridine rings, exhibit significant delocalization, suggesting potential activity for various applications. Experimentally, we initially determined the structure by depositing TPyPPB on a Silver fcc (Ag(111)) surface, where chemisorption interactions induced the formation of a triangular packing pattern rotated by 30 degrees along the primary crystallographic direction, as detailed in sec 2.10.1. Density Functional Theory (DFT) calculations confirmed the stability of this structure, with a formation energy difference of approximately 0.29 eV per TPyPPB molecule.

Our subsequent challenge involved examining the interaction of TPyPPB along chlorine atoms, leading to the discovery of an alternative "inverted" packing configuration, characterized by a formation energy difference of approximately 0.22 eV per TPyPPB molecule. DFT analysis revealed that both packing arrangements are stable across varying numbers of chlorine atoms per TPyPPB molecule, with only minor differences in formation energies of both packings, approximately 0.1-0.2 eV. So just based on our DFT calculations both structures can exist, but in our search of what triggers why each packing appears along the Cl atoms experiments showed that the order of insertion in the precursor mentioned in sec. 3.1 was the key factor of each packing. In the creation of highly ordered triangular nanoporous packing, the process begins with the deposition of TPyPPB. This is followed by an annealing step to induce Cl dissociation on the surface, after which another round of annealing is performed. Conversely, for the formation of the highly ordered nanostructure with inverted packing, the sequence is altered. Initially, Cl is dissociated on the Ag(111) surface, followed by an annealing step. Then, TPyPPB is deposited, and a final annealing step completes the process. Of course, as shown theoretically the increase of Cl atoms can increase the stability of TPyPPB on both packings, experimentally the number of Cl atoms can vary changing the precursor  $\text{Cl}_2\text{PhPt}$  concentrations.

Theoretical spectroscopy techniques such as FTIR and Raman simulations provided extensive information on the vibrational modes of isolated TPyPPB. These techniques revealed how the vibrational peaks shift upon physisorption



on Ag(111) and in the presence of Cl comparing the ratios of the vibrational modes within the different spatial arrangements TPyPPB that can exist providing an insight to a different possible characterization method which could be used aside microscopy. Ultraviolet Photoelectron Spectroscopy (UPS) and Inverse Photoelectron Emission Spectroscopy (IPES) simulations, based on the density of states (DOS) of both packing structures and the isolated Ag(111) surface, were used to examine how the occupied and empty states vary and shift in the presence of TPyPPB and TPyPPB with Cl. Additionally, to gain more insights into the electronic structure of both packings, the Projected Density of States (PDOS) was calculated for the 2D overlayer on top of the silver surface along the first layer of silver atoms. This analysis showed how the electronic structure of each atomic species changes through its interaction with Ag(111).

To complement the aforementioned electronic analysis of our systems, we conducted a Bader analysis<sup>104</sup> to depict and take a look at how the charge is being shared between Ag(111), TPyPPB, and Cl atoms on the surface obtaining that TPyPPB indeed shares some of their gained charge by the metallic surface to Cl. Triangular packing had a charge gained per TPyPPB molecule of 0.22 (e) without Cl atoms, that charge reduces to 0.14 (e) as we add the Cl atoms, same happens to inverted packing with the charge gained per TPyPPB molecule moving from 0.19 (e) to 0.13 (e) as we add Cl atoms. However, the charge gained per Cl atoms compared for both packings is 0.04 (e) greater on triangular packing. Later we studied TPyPPB isolated that presented an insulator bandgap of 4.23 eV as described by GLLB-SC results with a derivative discontinuity correction  $\Delta_x$  of 1.26 eV. LCAO-TDDFT-k- $\omega$  revealed notable transitions between two different energies in the ultraviolet range. Specifically, the exciton density showed greater electron-hole activity at 290 nm for both directions of the polarization light x and y making a transition of HOMO-2 $\rightarrow$ LUMO, but the greater transition occurred at 6.52 eV going from HOMO-13 $\rightarrow$ LUMO+10.

Finally, the Scanning Tunneling Microscopy images showed consistency between theoretical and experimental data. The difference between molecular densities of both packings was  $(0.02 \pm 0.02) \frac{mol}{nm^2}$ . Additionally, the triangular highly ordered nanoporous structure, with an area of  $\approx 1.7 nm^2$ <sup>117</sup>, proved to be an excellent structure for separating gases and small molecules<sup>117</sup> due to their size, and periodicity.

In conclusion, self-assembled monolayers (SAMs) and porous self-assembled monolayers (p-SAMs) proved satisfactory on organic molecules<sup>110</sup>. In this work, we adequately demonstrated the formation of SAMs and p-SAMs both theoretically, using DFT, and experimentally, through on-surface synthesis similar to previous work of Ceccatto et al.<sup>29</sup>. Additionally, through a deep analysis using vibrational spectroscopy, we provided comprehensive characterization, including electronic behavior and charge transfer of the isolated molecule on gas phase and both packings, complemented optical absorption spectroscopy, and topography studies of the highly ordered nanostructures based on STM experiments and simulations. These findings enhance our understanding of SAMs and p-SAMs, contributing valuable insights into their electronic properties and potential future applications as the pivotal role of a possible OPV's device based on TPyPPB due to its  $\pi$  electrons along as the facility of being self-assembled into periodical high ordered nanostructures just by thermal treatment. Furthermore, it was shown the effectivity of the triangular nanoporous as a separator of gases, and small molecules i.e. catalyst.

Nevertheless, there is a very first step and there is still a significant amount of work needed to develop a functional organic photovoltaic device using TPyPPB in the exact system we have proposed. Some of the next steps include mixing TPyPPB with other molecules that increase their activity through  $\pi$  electron interactions so it will be possible

---

to effectively transfer charge in a certain desired direction, and shift the OAS peak energy to the visible spectrum. Additionally, we encourage performing all experimental parts of this work to contrast and complement our theoretical spectroscopy modeling so that on-surface self-assembled structures can be enhanced not only via microscopy and its possible applications such as combining them with a catalyst and other organic molecules that promise a great approach for creating a possible OPV's.





## Appendix A

# Structures studied at Formation Energies

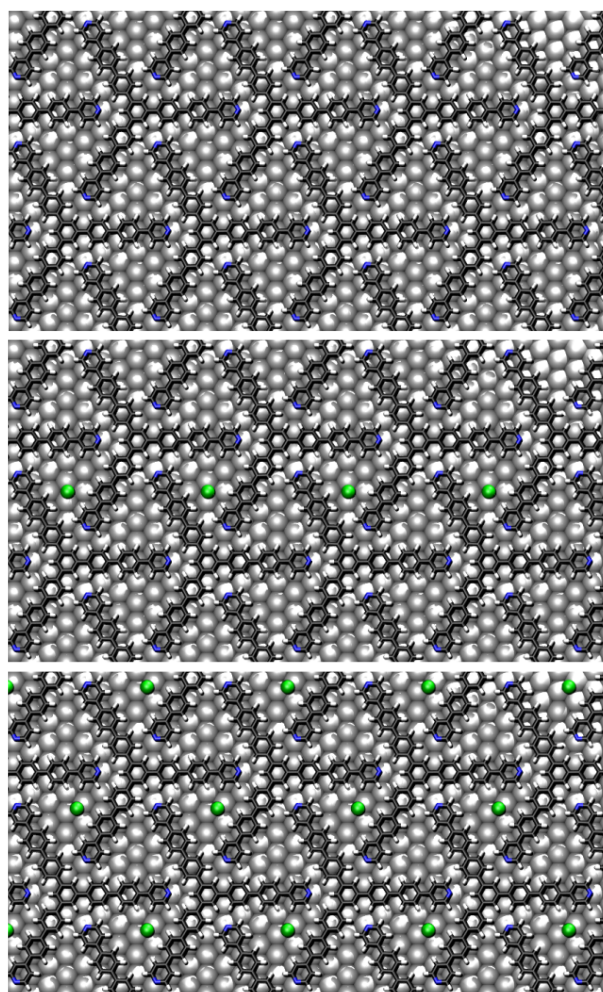


Figure A.1: Triangular packing structures studied for formation energies calculations

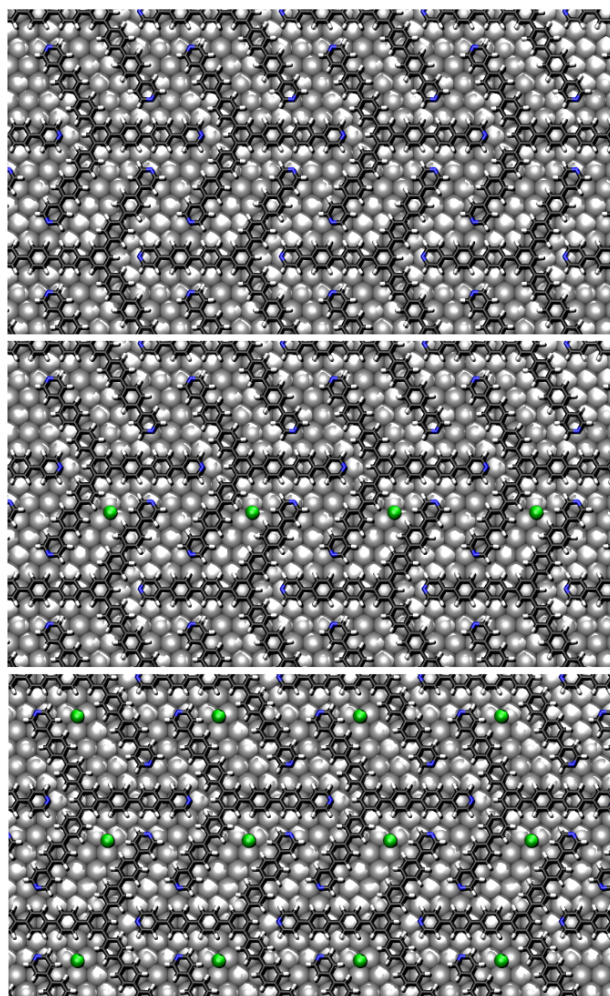


Figure A.2: Inverted packing structures studied for formation energies calculations



# Bibliography

- [1] Basov, D.; Averitt, R.; Hsieh, D. Towards properties on demand in quantum materials. *Nature Materials* **2017**, *16*, 1077–1088.
- [2] Li, R.; Xiao, F.; Amirkhanian, S.; You, Z.; Huang, J. Developments of nano materials and technologies on asphalt materials—A review. *Construction and Building Materials* **2017**, *143*, 633–648.
- [3] Smith, W. F. Self-assembly is ready to roll. *Nature Nanotechnology* **2007**, *2*, 77–78.
- [4] Sobota, J. A.; He, Y.; Shen, Z.-X. Angle-resolved photoemission studies of quantum materials. *Reviews of Modern Physics* **2021**, *93*, 025006.
- [5] Tokura, Y.; Kawasaki, M.; Nagaosa, N. Emergent functions of quantum materials. *Nature Physics* **2017**, *13*, 1056–1068.
- [6] Barth, J. V.; Costantini, G.; Kern, K. Engineering atomic and molecular nanostructures at surfaces. *Nature* **2005**, *437*, 671–679.
- [7] Lu, G. M.; Zhao, X. S. *Nanoporous materials: science and engineering*; World Scientific, 2004; Vol. 4.
- [8] Thommes, M.; Schlumberger, C. Characterization of nanoporous materials. *Annual Review of Chemical and Biomolecular Engineering* **2021**, *12*, 137–162.
- [9] Stupp, S. I. Self-assembly and biomaterials. *Nano Letters* **2010**, *10*, 4783–4786.
- [10] Binnig, G.; Rohrer, H. Scanning tunneling microscopy—from birth to adolescence. *Reviews of Modern Physics* **1987**, *59*, 615.
- [11] Braga, D.; Grepioni, F. *Crystal engineering: From Molecules and crystals to materials*; Springer, 1999; pp 421–441.
- [12] Kudernac, T.; Lei, S.; Elemans, J. A.; De Feyter, S. Two-dimensional supramolecular self-assembly: nanoporous networks on surfaces. *Chemical Society Reviews* **2009**, *38*, 402–421.



- [13] Lin, N.; Stepanow, S.; Ruben, M.; Barth, J. V. Surface-confined supramolecular coordination chemistry. *Templates in Chemistry III* **2009**, 1–44.
- [14] Ivasenko, O.; MacLeod, J. M.; Chernichenko, K. Y.; Balenkova, E. S.; Shpanchenko, R. V.; Nenajdenko, V. G.; Rosei, F.; Perepichka, D. F. Supramolecular assembly of heterocirculenes in 2D and 3D. *Chemical communications* **2009**, 1192–1194.
- [15] Griessl, S.; Lackinger, M.; Edelwirth, M.; Hietschold, M.; Heckl, W. M. Self-assembled two-dimensional molecular host-guest architectures from trimesic acid. *Single Molecules* **2002**, 3, 25–31.
- [16] Barth, J. V. Molecular architectonic on metal surfaces. *Annu. Rev. Phys. Chem.* **2007**, 58, 375–407.
- [17] Forrest, S. R. Ultrathin organic films grown by organic molecular beam deposition and related techniques. *Chemical reviews* **1997**, 97, 1793–1896.
- [18] Hoppe, H.; Sariciftci, N. S. Organic solar cells: An overview. *Journal of materials research* **2004**, 19, 1924–1945.
- [19] Dmitriev, A.; Lin, N.; Weckesser, J.; Barth, J.; Kern, K. Supramolecular assemblies of trimesic acid on a Cu (100) surface. *The Journal of Physical Chemistry B* **2002**, 106, 6907–6912.
- [20] Kawai, T.; Tanaka, H.; Nakagawa, T. Low dimensional self-organization of DNA-base molecules on Cu (111) surfaces. *Surface Science* **1997**, 386, 124–136.
- [21] Ortega Lorenzo, M.; Baddeley, C.; Muryn, C.; Raval, R. Extended surface chirality from supramolecular assemblies of adsorbed chiral molecules. *Nature* **2000**, 404, 376–379.
- [22] Barth, J. V.; Weckesser, J.; Cai, C.; Günter, P.; Bürgi, L.; Jeandupeux, O.; Kern, K. Building supramolecular nanostructures at surfaces by hydrogen bonding. *Angewandte Chemie International Edition* **2000**, 39, 1230–1234.
- [23] Barbosa, L. A. M.; Sautet, P. Stability of chiral domains produced by adsorption of tartaric acid isomers on the Cu (110) surface: a periodic density functional theory study. *Journal of the American Chemical Society* **2001**, 123, 6639–6648.
- [24] Weckesser, J.; De Vita, A.; Barth, J.; Cai, C.; Kern, K. Mesoscopic correlation of supramolecular chirality in one-dimensional hydrogen-bonded assemblies. *Physical Review Letters* **2001**, 87, 096101.
- [25] Böhringer, M.; Morgenstern, K.; Schneider, W.-D.; Berndt, R.; Mauri, F.; De Vita, A.; Car, R. Two-dimensional self-assembly of supramolecular clusters and chains. *Physical Review Letters* **1999**, 83, 324.
- [26] Furukawa, M.; Tanaka, H.; Sugiura, K.-i.; Sakata, Y.; Kawai, T. Fabrication of molecular alignment at the specific sites on Cu (111) surfaces using self-assembly phenomena. *Surface Science* **2000**, 445, L58–L63.

- [27] Lu, J.; Bao, D.-L.; Dong, H.; Qian, K.; Zhang, S.; Liu, J.; Zhang, Y.; Lin, X.; Du, S.-X.; Hu, W.; Gao, H.-J. Construction of two-dimensional chiral networks through atomic bromine on surfaces. *The Journal of Physical Chemistry Letters* **2017**, *8*, 326–331.
- [28] Chung, K.-H.; Kim, H.; Jang, W. J.; Yoon, J. K.; Kahng, S.-J.; Lee, J.; Han, S. Molecular multistate systems formed in two-dimensional porous networks on Ag (111). *The Journal of Physical Chemistry C* **2013**, *117*, 302–306.
- [29] Ceccatto, A.; Freiberger, E. M.; Waleska-Wellnhofer, N. J.; Jaekel, S.; Mowbray, D. J.; Papp, C.; Steinrück, H.-P.; de Siervo, A. Engineering large nanoporous networks with size and shape selected by appropriate precursors. *Carbon* **2024**, 118945.
- [30] Zangwill, A. A half century of density functional theory. *Physics Today* **2015**, *68*, 34–39.
- [31] Jain, A.; Ong, S. P.; Hautier, G.; Chen, W.; Richards, W. D.; Dacek, S.; Cholia, S.; Gunter, D.; Skinner, D.; Ceder, G.; Persson, K. A. Commentary: The Materials Project: A materials genome approach to accelerating materials innovation. *APL Materials* **2013**, *1*.
- [32] Nørskov, J. K.; Bligaard, T.; Rossmeisl, J.; Christensen, C. H. Towards the computational design of solid catalysts. *Nature chemistry* **2009**, *1*, 37–46.
- [33] Bahn, S. R.; Jacobsen, K. W. An object-oriented scripting interface to a legacy electronic structure code. *Computing in Science & Engineering* **2002**, *4*, 56–66.
- [34] Casida, M. E.; Huix-Rotllant, M. Progress in time-dependent density-functional theory. *Annual review of physical chemistry* **2012**, *63*, 287–323.
- [35] Lyon, K.; Preciado-Rivas, M. R.; Zamora-Ledezma, C.; Despoja, V.; Mowbray, D. J. LCAO-TDDFT- $k$ - $\omega$ : Spectroscopy in the optical limit. *Journal of Physics: Condensed Matter* **2020**, *32*, 415901.
- [36] Campi, G.; Duncan, J.; Ceccatto, A.; de Siervo, A. Using FTIR Simulation to Characterize Metal–Organic Frameworks: TPyPB on Cu(111). *Submitted* **2024**,
- [37] Kohn, W.; Sham, L. J. Self-consistent equations including exchange and correlation effects. *Physical Review* **1965**, *140*, A1133.
- [38] Perdew, J. P.; Burke, K.; Ernzerhof, M. Generalized gradient approximation made simple. *Physical Review Letters* **1996**, *77*, 3865.
- [39] Grimme, S.; Antony, J.; Ehrlich, S.; Krieg, H. A consistent and accurate ab initio parametrization of density functional dispersion correction (DFT-D) for the 94 elements H-Pu. *The Journal of Chemical Physics* **2010**, *132*.
- [40] Kresse, G.; Joubert, D. From ultrasoft pseudopotentials to the projector augmented-wave method. *Physical Review B* **1999**, *59*, 1758.

- [41] Mortensen, J. J.; Hansen, L. B.; Jacobsen, K. W. Real-space grid implementation of the projector augmented wave method. *Physical Review B* **2005**, *71*, 035109.
- [42] Larsen, A. H. *et al.* The atomic simulation environment—a Python library for working with atoms. *Journal of Physics: Condensed Matter* **2017**, *29*, 273002.
- [43] Porezag, D.; Pederson, M. R. Infrared intensities and Raman-scattering activities within density-functional theory. *Physical Review B* **1996**, *54*, 7830.
- [44] Tang, W.; Sanville, E.; Henkelman, G. A grid-based Bader analysis algorithm without lattice bias. *Journal of Physics: Condensed Matter* **2009**, *21*, 084204.
- [45] Born, M.; Heisenberg, W. Zur quantentheorie der molekeln. *Original Scientific Papers Wissenschaftliche Originalarbeiten* **1985**, 216–246.
- [46] Giustino, F. *Materials modelling using density functional theory: properties and predictions*; Oxford University Press, 2014.
- [47] Folkers, E. Floquet’s Theorem. Bachelor’s Thesis, University of Groningen, Netherlands, 2018.
- [48] Simon, S. H. *The Oxford solid state basics*; OUP Oxford, 2013.
- [49] Kittel, C. *Solid state physics*; Shell Development Company, 1955.
- [50] Monkhorst, H. J.; Pack, J. D. Special points for Brillouin-zone integrations. *Physical Review B* **1976**, *13*, 5188.
- [51] Chadi, D. J.; Cohen, M. L. Special points in the Brillouin zone. *Physical Review B* **1973**, *8*, 5747.
- [52] Einstein, A.; Podolsky, B.; Rosen, N. Can quantum-mechanical description of physical reality be considered complete? *Physical Review* **1935**, *47*, 777.
- [53] Pauli, W. Über den Zusammenhang des Abschlusses der Elektronengruppen im Atom mit der Komplexstruktur der Spektren. *Einführ. Orig* **1925**, *229*, 765–783.
- [54] Haynes, P. Linear-scaling methods in ab initio quantum-mechanical calculations. Ph.D. thesis, University of Cambridge, 1998.
- [55] Hedin, L.; Lundqvist, B. I. Explicit local exchange-correlation potentials. *Journal of Physics C: Solid state physics* **1971**, *4*, 2064.
- [56] Engel, E.; Dreizler, R. M. *Density Functional Theory: An Advanced Course*, 1st ed.; Springer: Heidelberg, 2011.
- [57] Hartree, D. R. *Mathematical Proceedings of the Cambridge Philosophical Society*; 1928; Vol. 24; pp 89–110.

- [58] Kohn, W.; Sham, L. *CONFERENCE PROCEEDINGS-ITALIAN PHYSICAL SOCIETY*; 1996; Vol. 49; pp 561–572.
- [59] Glanzmann, L. N. Modelling of Polymer-Carbon Nanotube Heterojunctions for Photovoltaic Applications. Ph.D. thesis, University of the Basque Country, Spain, 2017.
- [60] Slater, J. C. A simplification of the Hartree-Fock method. *Physical Review* **1951**, *81*, 385.
- [61] Perdew, J. P.; Zunger, A. Self-interaction correction to density-functional approximations for many-electron systems. *Physical Review B* **1981**, *23*, 5048–5079.
- [62] Gritsenko, O.; Mentel, .; Baerends, E. On the errors of local density (LDA) and generalized gradient (GGA) approximations to the Kohn-Sham potential and orbital energies. *The Journal of Chemical Physics* **2016**, *144*.
- [63] Perdew, J. P.; Burke, K.; Wang, Y. Generalized gradient approximation for the exchange-correlation hole of a many-electron system. *Physical Review B* **1996**, *54*, 16533.
- [64] Perdew, J. P.; Ernzerhof, M.; Zupan, A.; Burke, K. Nonlocality of the density functional for exchange and correlation: Physical origins and chemical consequences. *The Journal of Chemical Physics* **1998**, *108*, 1522–1531.
- [65] Zupan, A.; Burke, K.; Ernzerhof, M.; Perdew, J. P. Distributions and averages of electron density parameters: Explaining the effects of gradient corrections. *The Journal of Chemical Physics* **1997**, *106*, 10184–10193.
- [66] Perdew, J. P.; Ruzsinszky, A.; Csonka, G. I.; Vydrov, O. A.; Scuseria, G. E.; Constantin, L. A.; Zhou, X.; Burke, K. Restoring the density-gradient expansion for exchange in solids and surfaces. *Physical Review Letters* **2008**, *100*, 136406.
- [67] Grimme, S. Semiempirical GGA-type density functional constructed with a long-range dispersion correction. *Journal of computational chemistry* **2006**, *27*, 1787–1799.
- [68] Goerigk, L. A comprehensive overview of the DFT-D3 London-dispersion correction. *Non-covalent interactions in quantum chemistry and physics* **2017**, 195–219.
- [69] Preciado Rivas, M. R. Theoretical optical absorption and electron energy loss spectroscopy using LCAO-TDDFT-K- $\Omega$  of chlorophyll and carbon nanotubes. B.S. thesis, Universidad de Investigación de Tecnología Experimental Yachay, 2019.
- [70] Sham, L.; Schlüter, M. Density-functional theory of the band gap. *Physical Review B* **1985**, *32*, 3883.
- [71] Krieger, J.; Li, Y.; Iafate, G. Construction and application of an accurate local spin-polarized Kohn-Sham potential with integer discontinuity: Exchange-only theory. *Physical Review A* **1992**, *45*, 101.
- [72] Gritsenko, O.; van Leeuwen, R.; van Lenthe, E.; Baerends, E. J. Self-consistent approximation to the Kohn-Sham exchange potential. *Physical Review A* **1995**, *51*, 1944–1954.

- [73] Gritsenko, O. V.; Leeuwen, R. V.; Baerends, E. J. Direct approximation of the long- and short-range components of the exchange-correlation Kohn-Sham potential. *International journal of quantum chemistry* **1997**, *61*, 231–243.
- [74] Kuisma, M.; Ojanen, J.; Enkovaara, J.; Rantala, T. T. Kohn-Sham potential with discontinuity for band gap materials. *Physical Review B* **2010**, *82*, 115106.
- [75] Castelli, I. E.; Olsen, T.; Datta, S.; Landis, D. D.; Dahl, S.; Thygesen, K. S.; Jacobsen, K. W. Computational screening of perovskite metal oxides for optimal solar light capture. *Energy & Environmental Science* **2012**, *5*, 5814–5819.
- [76] Perdew, J. P. Density Gradient Expansion of the Electronic Exchange-Correlation Energy, and its Generalization. *Density Functional Theory* **1995**, 51–64.
- [77] Kohanoff, J. *Electronic structure calculations for solids and molecules: theory and computational methods*; Cambridge university press, 2006.
- [78] Gygi, F. Adaptive Riemannian metric for plane-wave electronic-structure calculations. *Europhysics Letters* **1992**, *19*, 617.
- [79] Gygi, F.; Galli, G. Real-space adaptive-coordinate electronic-structure calculations. *Physical Review B* **1995**, *52*, R2229.
- [80] Messiah, A. *Quantum mechanics*; Courier Corporation, 2014.
- [81] Griffiths, D. J.; Schroeter, D. F. *Introduction to quantum mechanics*; Cambridge university press, 2018.
- [82] Soler, J. M.; Artacho, E.; Gale, J. D.; García, A.; Junquera, J.; Ordejón, P.; Sánchez-Portal, D. The SIESTA method for ab initio order-N materials simulation. *Journal of Physics: Condensed Matter* **2002**, *14*, 2745.
- [83] Thygesen, K. S.; Mortensen, J. J. Localized atomic orbital basis sets in the projector augmented wave method. Ph.D. thesis, Ph. D Thesis, Technical University of Denmark, 2008.
- [84] Slater, J. C. An augmented plane wave method for the periodic potential problem. *Physical Review* **1953**, *92*, 603.
- [85] Blöchl, P. E. Projector augmented-wave method. *Physical Review B* **1994**, *50*, 17953.
- [86] Maitra, N. T.; Burke, K.; Woodward, C. Memory in time-dependent density functional theory. *Physical Review Letters* **2002**, *89*, 023002.
- [87] Marques, M. A.; Gross, E. K. Time-dependent density functional theory. *Annu. Rev. Phys. Chem.* **2004**, *55*, 427–455.
- [88] Runge, E.; Gross, E. K. Density-functional theory for time-dependent systems. *Physical Review Letters* **1984**, *52*, 997.

- [89] Ullrich, C. A. Time-dependent density-functional theory: concepts and applications. **2011**,
- [90] Bruner, A.; LaMaster, D.; Lopata, K. Accelerated broadband spectra using transition dipole decomposition and Padé approximants. *Journal of Chemical Theory and Computation* **2016**, *12*, 3741–3750.
- [91] Repisky, M.; Konecny, L.; Kadek, M.; Komorovsky, S.; Malkin, O. L.; Malkin, V. G.; Ruud, K. Excitation energies from real-time propagation of the four-component Dirac–Kohn–Sham equation. *Journal of Chemical Theory and Computation* **2015**, *11*, 980–991.
- [92] Yabana, K.; Nakatsukasa, T.; Iwata, J.-I.; Bertsch, G. Real-time, real-space implementation of the linear response time-dependent density-functional theory. *physica status solidi (b)* **2006**, *243*, 1121–1138.
- [93] Rossi, T. P.; Kuisma, M.; Puska, M. J.; Nieminen, R. M.; Erhart, P. Kohn–Sham decomposition in real-time time-dependent density-functional theory: An efficient tool for analyzing plasmonic excitations. *Journal of Chemical Theory and Computation* **2017**, *13*, 4779–4790.
- [94] Larsen, A. H.; Vanin, M.; Mortensen, J. J.; Thygesen, K. S.; Jacobsen, K. W. Localized atomic basis set in the projector augmented wave method. *Physical Review B* **2009**, *80*, 195112.
- [95] Larsen, A. H.; Kleis, J.; Thygesen, K. S.; Nørskov, J.; Jacobsen, K. W. Electronic shell structure and chemisorption on gold nanoparticles. *Physical Review B* **2011**, *84*, 245429.
- [96] Dongarra, J.; Petitet, A. *International Workshop on Applied Parallel Computing*; 1995; pp 166–176.
- [97] Crank, J.; Nicolson, P. *Mathematical proceedings of the Cambridge philosophical society*; 1947; Vol. 43; pp 50–67.
- [98] Adler, S. L. Quantum theory of the dielectric constant in real solids. *Physical Review* **1962**, *126*, 413.
- [99] Liebsch, A. Violation of sum rules by random-phase-approximation surface response calculations based on a density-functional ground-state description. *Physical Review B* **1985**, *32*, 6255.
- [100] Steele, D. *Theory of Vibrational Spectroscopy*; W.B. Saunders Company, 1971.
- [101] Wilson, E. B.; Decius, J. C.; Cross, P. C. *Molecular vibrations: the theory of infrared and Raman vibrational spectra*; Courier Corporation, 1980.
- [102] Cardona, M.; Ehrenfreund, E.; Güntherodt, G.; Kash, J.; von der Osten, W.; Page, J.; Ramdas, A.; Rodriguez, S.; Thomsen, C.; Tsang, J. In *Light Scattering in Solids VI: Recent Results, Including High-Tc Superconductivity*, 1st ed.; Cardona, M., Güntherodt, G., Eds.; Springer Science & Business Media, 2005; Vol. 68.
- [103] Matta, C. F.; Boyd, R. J. An introduction to the quantum theory of atoms in molecules. *The quantum theory of atoms in molecules: from solid state to DNA and drug design* **2007**,

- [104] Bader, R. F. W. *Atoms in Molecules: A Quantum Theory*; Oxford University Press: Oxford, U.K., 1990.
- [105] Henkelman, G.; Arnaldsson, A.; Jónsson, H. A fast and robust algorithm for Bader decomposition of charge density. *Computational Materials Science* **2006**, *36*, 354–360.
- [106] Sanville, E.; Kenny, S. D.; Smith, R.; Henkelman, G. Improved grid-based algorithm for Bader charge allocation. *Journal of computational chemistry* **2007**, *28*, 899–908.
- [107] Dyke, J.; Jonathan, N.; Morris, A. *Electron spectroscopy: theory, techniques and applications*. 1979.
- [108] Hino, S. Introduction to Ultraviolet Photoelectron Spectroscopy. *TANSO* **2000**, *2000*, 80–82.
- [109] Whitten, J. E. Ultraviolet photoelectron spectroscopy: Practical aspects and best practices. *Applied Surface Science Advances* **2023**, *13*, 100384.
- [110] Casalini, S.; Bortolotti, C. A.; Leonardi, F.; Biscarini, F. Self-assembled monolayers in organic electronics. *Chemical Society Reviews* **2017**, *46*, 40–71.
- [111] Cheshnovsky, O.; Yang, S.; Pettiette, C.; Craycraft, M.; Liu, Y.; Smalley, R. Ultraviolet photoelectron spectroscopy of semiconductor clusters: silicon and germanium. *Chemical Physics Letters* **1987**, *138*, 119–124.
- [112] Faes, B. B. M. Structural and chemical properties of boron and nitrogen dopants in graphene by means of STM/AFM in UHV at 5 K Master Thesis.
- [113] Chen, C. J. *Introduction to Scanning Tunneling Microscopy Third Edition*; Oxford University Press, USA, 2021; Vol. 69.
- [114] Eigler, D. M.; Schweizer, E. K. Positioning single atoms with a scanning tunnelling microscope. *Nature* **1990**, *344*, 524–526.
- [115] Tersoff, J.; Hamann, D. R. Theory of the scanning tunneling microscope. *Physical Review B* **1985**, *31*, 805.
- [116] Enkovaara, J. *et al.* Electronic structure calculations with GPAW: a real-space implementation of the projector augmented-wave method. *Journal of Physics: Condensed Matter* **2010**, *22*, 253202.
- [117] Ceccatto, A.; Campi, G. C.; Carreño-Díaz, V.; da Costa-Ferreira, E. B.; Waleska-Wellenhofer, N. J.; Freiberger, E. M.; Jaekel, S.; Papp, C.; Hans-Peter, S.; Duncan, J. M.; de Siervo, A. Engineering: Two-Dimensional Supramolecular Self-Assembly: The Role of Cl Atoms. *Submitted* **2024**,
- [118] Bitzek, E.; Koskinen, P.; Gähler, F.; Moseler, M.; Gumbsch, P. Structural relaxation made simple. *Physical Review Letters* **2006**, *97*, 170201.
- [119] Walter, M.; Moseler, M. Ab initio wavelength-dependent Raman spectra: Placzek approximation and beyond. *Journal of Chemical Theory and Computation* **2019**, *16*, 576–586.

- [120] Doll, K.; Harrison, N. M. Theoretical study of chlorine adsorption on the Ag(111) surface. *Physical Review B* **2001**, *63*, 165410.
- [121] Fauster, T.; Dose, V. Inverse photoemission spectroscopy. *Chemistry and Physics of Solid Surfaces VI* **1986**, 483–507.
- [122] Frank, K.-H.; Dudde, R.; Koch, E. Electron affinity levels of benzene and azabenzenes on Cu (111) and Au (110) revealed by inverse photoemission. *Chemical Physics Letters* **1986**, *132*, 83–87.
- [123] OSGOOD JR, R. M.; Wang, X. *Solid State Physics*; Elsevier, 1998; Vol. 51; pp 1–80.
- [124] Yannoulis, P.; Frank, K.-H.; Koch, E.-E. Electronic structure and orientation of anthracene on Ag (111). *Surface Science* **1991**, *241*, 325–334.
- [125] Dudde, R.; Reihl, B. Complete electronic structure of oriented films of hexatriacontane. *Chemical Physics Letters* **1992**, *196*, 91–96.
- [126] Otto, A.; Frank, K.; Reihl, B. Inverse photoemission of pyridine on silver (111). *Surface Science* **1985**, *163*, 140–152.
- [127] Parr, R. G.; Yang, W. *Density-functional Theory of Atoms and Molecules*; Oxford University Press: New York, 1989.
- [128] Fukui, K. Role of frontier orbitals in chemical reactions. *Science* **1982**, *218*, 747–754.
- [129] Brédas, J.-L.; Calbert, J. P.; da Silva Filho, D.; Cornil, J. Organic semiconductors: A theoretical characterization of the basic parameters governing charge transport. *Proceedings of the National Academy of Sciences* **2002**, *99*, 5804–5809.